Dissertation

submitted to the
Combined Faculties for the Natural Sciences and
for Mathematics
of the Ruperto-Carola University of Heidelberg,
Germany
for the degree of
Doctor of Natural Sciences

presented by
Sergej Moroz
born in Konchezero, Russia
Oral examination: 25.01.2011

Few-body Physics with Functional Renormalization

Referees: **Prof. Dr. Christof Wetterich**
Prof. Dr. Jan Martin Pawlowski

Wenig-Teilchen Physik mit funktionaler Renormierung

Zusammenfassung

In dieser Dissertation wird mit Hilfe der Methode der funktionalen Renormierung die nicht-relativistische Quantenphysik weniger Teilchen untersucht. Im speziellen diskutieren wir verschiedene theoretische Aspekte der Physik weniger Teilchen, die mit dem Efimov-Effekt verbunden sind. Unser zentrales Ergebnis ist, dass sich dieser Effekt im Auftreten von Renormierungsgruppen-Limitzyklen offenbart. Zuerst wird das Problem eines singulären Potential $V(r) \sim \frac{1}{r^2}$ behandelt. Hierauf untersuchen wir das Efimov Problem dreier Teilchen, die durch ein kurzreichweitiges Zwei-Teilchen-Potential wechselwirken. Anschließend präsentieren wir die ersten Schritte in Richtung der Lösung des quantenmechanischen Vier-Teilchen Problems mit Hilfe der Renormierungsgruppe für Bosonen. Abschließend werden zusammengesetzte Operatoren mit komplexer Skalendimension diskutiert, welche ein allgemeiner Bestandteil der Efimov Physik sind.

Few-body physics with functional renormalization

Abstract

In this thesis nonrelativistic few-body quantum physics is investigated with the method of functional renormalization. In particular, we discuss different theoretical aspects of few-body physics related to the Efimov effect. Our central finding is that this effect manifests itself as a renormalization group limit cycle. First, we treat the problem of a singular, inverse square potential in quantum mechanics. Then we examine the original Efimov problem of three particles interacting via a short-range two-body potential. Subsequently, we present a first step towards the renormalization group solution of the four-body quantum problem for bosons. Finally, a general theoretical feature of the Efimov physics, composite operators with complex scaling dimensions, are discussed.

Contents

Chapter 1

Introduction

Problems related to the motion of few interacting bodies are ubiquitous in physics. After the advent of the Newton's classical mechanics astronomers were able to predict the motion of planets in the Solar System. To the first approximation the trajectory of the planet is determined only by the gravitational force between the Sun and the planet – a simple two-body problem. This trajectory is, however, slightly perturbed by the neighboring planets and for a more precise prediction one must solve three-, four- and higher-body problems. The triumph of few-body classical physics was the discovery of Neptune. The existence of this planet was theoretically predicted in 1845 from unexpected changes of the orbit of its neighbor Uranus. In the early days of quantum mechanics few-body physics was of a key interest. After solving problem of the hydrogen atom in $1925-1926$, people started to tackle more difficult quantum three-body problems such as the helium atom, where two electrons orbit around the nucleus. Although the helium atom can not be solved analytically, it served as an excellent stimulus for developing perturbation and variational methods in quantum mechanics. Also nowadays few-body problems are of central importance in different areas of science such as physical chemistry, atomic physics and nuclear physics.

The main topic of this thesis is nonrelativistic few-body quantum physics. More specifically, we will be mainly interested in quantum problems of few electrically neutral atoms. Two neutral atoms interact with each other via the van der Waals potential $V(r)$ which falls off at large distances r as

$$\lim_{r\to\infty} V(r) = -\frac{C}{r^6}. \tag{1.1}$$

One can now associate a length scale $l_{vdW} = \left(\frac{mC}{\hbar^2}\right)^{1/4}$ with the van der Waals potential. Here C is a constant, m denotes the mass of interacting atoms and $\hbar$ stands for the reduced Planck constant. Importantly, at collision energy

$E \ll \frac{\hbar^2}{m l_{vdW}^2}$ the interaction can be described accurately by a simple short-range potential. In other words, at low energies neutral atoms behave like pointlike particles. Their two-body scattering is determined by the s-wave scattering length which will be denoted by a.[1]

Generically, physical observables of a few-particle system will depend on the scattering length a, but also on other (microscopic) parameters of the interaction potential such as the effective range, the range of interaction, etc. However, in the regime of $a \gg$ all other length scales, physical properties of the system will depend only on the scattering length. This is what is known under the name of few-body universality (for a review see [1]). Few-body universality is a very useful concept, since in the universal regime physical observables are insensitive to microscopic details of the interaction potential which are often difficult to measure precisely. Hence, prediction of a few-body universal theory are very simple and can be straightforwardly tested experimentally. As an example of such prediction, we consider a two-body (dimer) bound state. For $a > 0$ the universal theory predicts the presence of a dimer with the binding energy $E_D = -\frac{\hbar^2}{m a^2}$, which is in a good agreement with numerous experiments with ultracold atomic gases.

In general, we can enter the universal regime by a fine-tuning of some interaction parameter. The fine-tuning can be either accidental or experimental. Accidentally fine-tuned systems are gifts of Nature, for which "by accident" the scattering length happened to be much larger than other length scales. In atomic physics, for example, a pair of ^{4}He atoms can be described fairly well with the universal theory due to the accidental fine-tuning. In nuclear physics, pn and $\alpha\alpha$ systems are good examples of the accidental fine-tuning. Nowadays it is possible to change the scattering length over a wide range in experiments with ultracold atomic gases. A so-called Feshbach resonance (for a review see [2]) gives experimentalists a unique opportunity to enter the universal regime by simply tuning an external magnetic field. The advent of Feshbach resonances revolutionized the field of few-body quantum physics and made it a very active area of theoretical and experimental research.

In this thesis we focus our attention mainly on the specific part of few-body quantum physics known as the Efimov effect. In 1970 Vitaly Efimov solved a quantum problem of three bosons interacting via a two-body short-range attractive potential [3]. In the universal regime[2] Efimov found an

[1] A notable exception is a collision of two identical fermions which can not scatter in the s-wave channel. We do not discuss this case in the thesis.

[2] Note that in order to make the Efimov problem well-defined, in addition to the scattering length a, one must necessarily introduce a dimensionless three-body parameter which encodes details of the microscopic interaction [1]. In the context of the Efimov effect we

intricate energy spectrum of three-body (trimer) bound states. Surprisingly, he predicted bound trimers even for $a < 0$, where there is no two-body bound state. At the unitarity point,[3] where $a^{-1} = 0$, the energy spectrum forms a geometric series

$$\frac{E_{n+1}}{E_n} = e^{-\frac{2\pi}{s_0}} \quad \text{as } n \to \infty \tag{1.2}$$

with E_{n+1} and E_n denoting neighboring bound state energies. The so-called Efimov parameter $s_0 \approx 1.00624$ can be obtained as a solution of a transcendental equation [1]. For a long time the Efimov finding was "just" a theoretical conjecture. Efimov formulated his prediction in the context of nuclear physics. However, in nuclear physics verification of the Efimov finding is hindered by the presence of the long-range Coulomb interaction between protons and neutrons and the impossibility of experimental fine-tuning. Consequently, early experimental attempts to find the Efimov trimer states in nuclear physics were fruitless. The situation changed dramatically during recent years with an advent of ultracold atomic gases and Feshbach resonances. The first clear experimental signature of the Efimov state in ultracold cesium was discovered in Innsbruck in the group of Rudolf Grimm in 2006 [4]. In this work the lowest Efimov state was observed indirectly by measuring the atom-atom-atom loss resonance (for $a < 0$) and the atom-dimer loss resonance (for $a > 0$). These resonances were identified with positions where the Efimov state merges with the scattering continuum. The findings of Kraemer et al. [4] stimulated extensive experimental activity in the field of Efimov physics (for a pedagogical review see [5]). As a result, by now the Efimov effect is believed to be a well-understood phenomenon, both theoretically and experimentally.

Efimov made his discovery by solving the Schrödinger equation for three interacting particles. Since 1970 powerful theoretical methods were developed for quantum-mechanical treatment of the three-body problem (for reviews see [6, 1, 7]). Effective field theory is an alternative valuable tool for studying Efimov physics [1]. In this thesis we employ yet another field-theoretical – the technique of functional renormalization for investigation of the Efimov effect. This allows us to view the problem from a different perspective and gain some additional insights.

The thesis is structured as follows: Chapter 2 is devoted to an introduction to the method of functional renormalization. In Chapter 3 we start with two-body quantum mechanics with an inverse square potential. Solution of

will use this modified definition of few-body universality.

[3] At the unitarity point ($a^{-1} = 0$) the two-body problem has a zero-energy bound state and a scattering cross section saturates the unitarity bound.

this simple problem allows us to understand the essence of the Efimov effect and gain a simple intuition for it. In Chapter 4 we present our results for the three-body problem of cold atoms near a Feshbach resonance. We consider systems of three bosons and fermions and discuss the difference between them. The following Chapter 5 is devoted to an extension of the Efimov problem – the four-body problem for bosons. In this Chapter we describe our first step towards the renormalization group treatment of this interesting system. In Chapter 6 we discuss a general manifestation of the Efimov phenomenon – the presence of composite operators with complex scaling dimensions. As a simple illustration we compute the scaling dimension and the propagator of the s-wave two-body composite operator $\mathcal{O} = \psi\psi$ in quantum mechanics with the inverse square potential. We draw our conclusions and present the outlook in Chapter 7. Finally, technical details are summarized in Appendices A-E.

Chapter 2

Functional Renormalization Group

This Chapter is devoted to a short introduction to the method of functional renormalization group (FRG) that we employed in our studies of various quantum-mechanical few-body problems. First, we provide an intuitive picture which is behind FRG and also list some of the problems in theoretical physics which the method has been applied to. Subsequently, the central equation of FRG, the Wetterich flow equation governing the renormalization group evolution, is presented. Next, we discuss different aspects of functional renormalization. Finally, we use a very simple toy model- a zero-dimensional field theory- to examplify how the Wetterich equation can be derived and used in practice.

2.1 Functional renormalization: what is it about and what is it for?

Functional renormalization group[1] is a realization of the renormalization group concept in the framework of quantum and/or statistical field theory. FRG combines mathematical functional methods of quantum field theory with the physically intuitive implementation of renormalization group due to Wilson [8]. Roughly speaking, the main idea of renormalization group, developed by Kadanoff, Callan, Symanczik, Wilson and others, consists in the ingenious observation that it is often more useful to perform integration of quantum fluctuations in (continuous) steps rather than to do it at once. The FRG technique allows to interpolate smoothly between the known

[1] sometimes also called exact renormalization group

microscopic laws and the complicated macroscopic phenomena in physical systems. In this sense, it bridges the transition from simplicity of microphysics to complexity of macrophysics. Figuratively speaking, FRG acts as a microscope with a variable resolution. One starts with a high-resolution picture of the known microphysical laws and subsequently decreases the resolution to obtain a coarse-grained picture of macroscopic phenomena. The method is nonperturbative, meaning that is does not rely on an expansion in any small (e.g. interaction strength or $1/N$) parameter.

The method of functional renormalization is very general and was applied to numerous problems in physics. Here we list just few of them and cite some review articles, where more information can be found:

- In statistical field theory, FRG provided a unified picture of phase transitions in classical linear $O(N)$-symmetric scalar theories in different dimensions d, including critical exponents for $d = 3$ and the Berezinskii-Kosterlitz-Thouless phase transition for $d = 2$, $N = 2$ [9].

- In quantum theory of gauge fields, FRG was used, for instance, to investigate the chiral phase transition and infrared properties of QCD and its large-flavor extensions [10].

- In condensed matter physics, the method proved to be successful to treat lattice models (e.g. the Hubbard model or frustrated magnetic systems), repulsive Bose gas, BEC/BCS crossover for two-component Fermi gas, Kondo effect, disordered systems and nonequlibrium phenomena [11, 12, 13].

- Application of FRG to gravity provided solid arguments in favor of nonperturbative renormalizability of quantum theory of gravity in four spacetime dimensions [15, 16], known as the asymptotic safety scenario.

- In mathematical physics FRG was used to prove renormalizability of different field theories.

2.2 The Wetterich flow equation

In the framework of quantum field theory, the effective action Γ is a direct analogue of the classical action functional S. It depends on the fields of a given theory and includes all quantum fluctuations.[2] Variation of Γ with

[2]Note that due to a formal equivalence between Euclidean quantum field theory in d spacetime dimensions and classical statistical field theory in d spatial dimensions, one can

respect to fields yields exact quantum field equations, for example for cosmology or the electrodynamics of superconductors. Mathematically, Γ is the generating functional of one-particle irreducible vertices. Interesting physics, like field propagators (two-point Green functions) and scattering amplitudes (higher-point amputated, connected Green function), can be extracted from Γ in a straightforward (although sometimes tedious) way. In a generic interacting field theory the effective action Γ, however, is difficult to obtain. FRG provides a practical tool to calculate Γ employing the concept of renormalization group.

The central object in FRG is a scale-dependent effective action functional Γ_k often called average action or flowing action. The dependence on the RG sliding scale k is introduced by adding a regulator (infrared cutoff) $R_k(q)$ to the full inverse propagator $\Gamma_k^{(2)}$. Roughly speaking, the regulator $R_k(q)$ decouples slow fluctuation modes with momenta $q \lesssim k$ by giving them a large mass, while the higher momentum modes are not affected. Thus, Γ_k includes all quantum fluctuations with momenta $q \gtrsim k$. The flowing action Γ_k obeys the exact functional flow equation

$$\partial_k \Gamma_k \;=\; \frac{1}{2}\mathrm{STr}\,\partial_k R_k\,(\Gamma_k^{(2)} + R_k)^{-1}, \tag{2.1}$$

derived by Christof Wetterich in 1993 [17]. Despite its compact and elegant form, the flow equation governs the full quantum dynamics. In Eq. (2.1) ∂_k denotes a derivative with respect to the sliding scale k at fixed values of the fields. The functional differential equation for Γ_k must be supplemented with the initial condition $\Gamma_{k\to\Lambda} = S$, where the "classical action" S describes the physics at the microscopic ultraviolet scale $k = \Lambda \to \infty$. Importantly, in the infrared limit $k \to 0$ the full effective action $\Gamma = \Gamma_{k\to 0}$ is obtained. In the Wetterich equation STr denotes a supertrace operation which sums over momenta, frequencies, internal indices, and different fields (taking bosons with a plus and fermions with a minus sign). It is important to note that the exact flow equation for Γ_k has a one-loop structure. This is an important simplification compared to perturbation theory, where all multi-loop Feynman diagrams must be included. The second functional derivative $\Gamma_k^{(2)}$ is the full inverse field propagator modified by the presence of the regulator $R_k(q)$.

The renormalization group evolution of Γ_k traces a trajectory in the theory space, which is a multi-dimensional space of all possible couplings $\{c_n\}$ allowed by symmetries of the problem. As schematically shown in Figure 2.1, at the microscopic ultraviolet scale $k = \Lambda \to \infty$ one starts with the initial condition $\Gamma_{k=\Lambda} = S$. As the sliding scale k is lowered, the flowing action Γ_k

define the effective action Γ in classical statistical field theory. In this case Γ includes all thermal fluctuations and represents the grandcanonical potential.

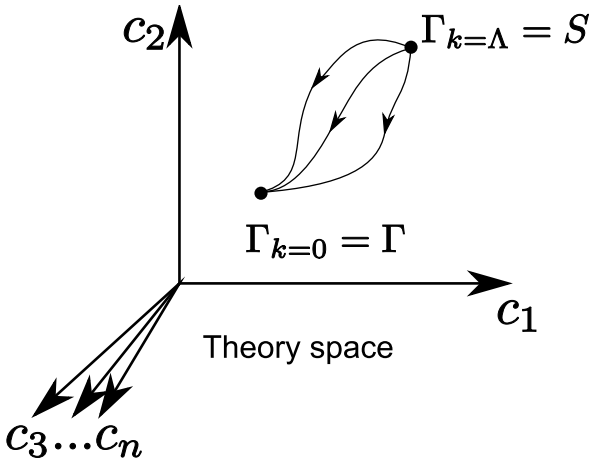

Figure 2.1: Renormalization group flow in the theory space of all possible couplings allowed by symmetries. Different trajectories correspond to different choices of the infrared regulator $R_k(q)$.

evolves in the theory space according to the functional flow equation. Thus, different couplings $\{c_n\}$ become running or flowing under the renormalization group evolution. The choice of the regulator $R_k(q)$ is not unique. This introduces some scheme dependence into the renormalization group flow. For this reason, different choices of the regulator $R_k(q)$ correspond to the different paths in Figure 2.1. At the infrared scale $k = 0$, however, the full effective action $\Gamma_{k=0} = \Gamma$ is recovered for every choice of the cutoff $R_k(q)$, and, thus, all trajectories meet at the same point in the theory space.

In most cases of interest the Wetterich equation can only be solved approximately. Usually some type of expansion of Γ_k is performed, which is then truncated at finite order leading to a finite system of ordinary differential equations. Different systematic expansion schemes were developed. The choice of the suitable scheme should be physically motivated and depends on a given problem. Importantly, the expansions do not necessarily involve any small parameter (like an interaction coupling constant) and thus they are, in general, of nonperturbative nature.

2.3 Aspects of functional renormalization

Here we list various aspects of functional renormalization which in our opinion merit special discussion

Truncations and error estimates The Wetterich flow equation is an exact equation. However, in practice, the functional differential equation must be truncated, i.e. it must be projected to functions of few variables or even onto some finite-dimensional sub-theory space. As in every nonperturbative method, the question of error estimate is very important and nontrivial in functional renormalization. One way to estimate the error in FRG is to improve the truncation in successive steps, i.e. to enlarge the sub-theory space by including more and more running couplings. The difference in the flows for different truncations gives a good estimate of the error. Alternatively, one can use different regulator functions R_k in a given (fixed) truncation and determine the difference of the RG flows in the infrared for the respective regulator choices. If bosonization is used, one can check the insensitivity of final results with respect to different bosonization procedures.

Regulator choice and optimization As mentioned above, in FRG one encounters a high degree of arbitrariness in the choice of the infrared regulator $R_k(q)$. In every relativistic field theory, the regulator function should satisfy three important conditions. First $R_k(q)$ should suppress infrared modes, i.e.

$$R_k(q) > 0 \qquad \text{for } q^2/k^2 \to 0. \tag{2.2}$$

Second, the regulator must vanish in the infrared

$$R_k(q) \to 0 \qquad \text{for } k \to 0. \tag{2.3}$$

Finally, we should recover the bare (classical) action in the ultraviolet and thus[3]

$$R_k(q) \to \infty \qquad \text{for } k = \Lambda \to \infty. \tag{2.4}$$

Apart from these requirements, the cutoff can be chosen arbitrarily. Nevertheless, it is recommended to pick the regulator carefully depending on a concrete physical problem. Moreover, one should better choose a regulator that respects all symmetries of the studied problem.[4] Under this choice the whole RG trajectory is invariant under the symmetry transformation. The apparent benefit here is that one can work in the space of symmetric average actions, i.e. use symmetric truncations with only terms invariant under symmetries.

Finally, as has been already mentioned, for a given truncation different choice of regulators leads to different effective action Γ. A question which naturally arises at this point is: what is the best choice of a regulator function

[3]We will make this point more clear in the next Section.

[4]Unfortunately, this is not always possible as, for example, in relativistic gauge theories.

within a given truncation? A procedure of finding rigorous answer to this question is known under the name of optimization [19, 20, 18]. Roughly speaking, the optimized cutoff is the one which realizes the RG flow with the shortest length in the theory space.

Fixed points In FRG, as in all renormalization group methods, a lot of insight about a physical system can be gained from the topology of RG flows. Specifically, identification of fixed points of the renormalization group evolution is of great importance. Near fixed points the flow of running couplings effectively stops and RG β-functions approach zero. Presence of (partially) stable infrared fixed points is closely connected to the concept of universality. Universality manifests itself in the observation that some very distinct physical systems have the same critical behavior. For instance, to good accuracy, critical exponents of the liquid-gas phase transition in water and the ferromagnetic phase transition in magnets are the same. Few-body universality, introduced in Chapter 1, is another good example. In the renormalization group language, different systems from the same universality class flow to the same (partially) stable infrared fixed point. In this way macrophysics becomes independent of the microscopic details of the particular physical model.

Nonrenormalizable couplings Compared to the perturbation theory, functional renormalization does not make a strict distinction between renormalizable and nonrenormalizable couplings. All running couplings that are allowed by symmetries of the problem are generated during the FRG flow. However, the nonrenormalizable couplings approach partial fixed points very quickly during the evolution towards the infrared, and thus the flow effectively collapses on a hypersurface of the dimension given by the number of renormalizable couplings [21]. Taking the nonrenormalizable couplings into account allows to study nonuniversal features that are sensitive to the concrete choice of the microscopic action S and the finite ultraviolet cutoff Λ.

Connection to Polchinski equation The Wetterich equation can be obtained from the Legendre transformation of the Polchinski functional equation, derived by Joseph Polchinski in 1984 [22]. The concept of the effective average action, used in FRG, is, however, more intuitive than the flowing bare action in the Polchinski equation. In addition, FRG method proved to be more suitable for numerical calculations.

Composite degrees of freedom Typically, low-energy physics of strongly interacting systems is described by macroscopic degrees of freedom (i.e. particle excitations) which are very different from microscopic high-energy degrees of freedom. For instance, QCD is a field theory of interacting quarks and gluons. At low energies, however, proper degrees of freedom are baryons and mesons. Another example is the BEC/BCS crossover problem in condensed matter physics. While the microscopic theory is defined in terms of two-component nonrelativistic fermions, at low energies a composite (particle-particle) dimer becomes an additional degree of freedom, and it is advisable to include it explicitly in the model. The low-energy composite degrees of freedom can be introduced in the description by the method of partial bosonization, known as the Hubbard-Stratonovich transformation. This transformation, however, is done once and for all at the UV scale Λ. In FRG a more efficient way of incorporating macroscopic degrees of freedom was introduced, which is known as flowing bosonization or rebosonization [23, 10, 24]. With the help of a scale-dependent field transformation, this method allows to perform the Hubbard-Stratonovich transformation continuously at all RG scales k. In this thesis we will use rebosonization extensively as an efficient and elegant tool in Chapters 3 and 4.

2.4 Zero-dimensional field theory

Despite its compact and elegant form, the Wetterich equation (2.1) is a very complicated functional differential equation. Not much is known so far about its mathematical properties. In order to simplify our discussion, in this Section we consider a very simple field theory defined at a single point, i.e. in the zero-dimensional spacetime.[5] The theory is formally defined by its generating function of correlation functions which is given by the one-dimensional integral over the "field" variable x

$$Z(j) = \int_{-\infty}^{\infty} dx \exp(-S(x) + jx) \tag{2.5}$$

with the action $S(x)$ and the source j. In the following we consider the "ϕ^4" theory with $S(x) = \frac{1}{2}x^2 + \frac{\lambda}{4!}x^4$. The integral can not be performed analytically for a general source j. Nevertheless, one can evaluate it numerically (for given λ and j) with an arbitrary precision. Thus, the model seems to be an ideal

[5] Part of the material described in this Section was presented by Professor Jan Pawlowski at his lecture "Functional Renormalization Group flows in gauge theories" in Heidelberg in 2008.

tool for benchmarking various approximation schemes. In addition, one can think about few potential applications

- We can think about this model as the lattice theory defined at a single lattice site. We note, however, that even in higher-dimensional lattice theories in the limit of strong coupling different lattice sites decouple, since in this limit the contribution from the kinetic term of the Hamiltonian can be neglected compared to the contribution of the interaction term. For this reason, at strong coupling the higher-dimensional generating function can be expressed as a product of factors $Z(j)$ located at different lattice sites. In this sense, the zero-dimensional field theory is a good starting point for developing a strong coupling expansion [25].

- One can view quantum mechanics as a quantum field theory defined in one temporal dimension. From this perspective, quantum mechanics at nonzero temperature is most conveniently formulated as a one-dimensional Euclidean field theory with a compact imaginary time direction. In the Matsubara formalism the compact nature of the imaginary time translates into a discrete set of Matsubara frequencies $\omega_n = 2\pi T n$ (for bosons). At high temperatures only the lowest frequency $\omega_{n=0}$ is important, while all higher Matsubara modes are gaped and effectively decouple. This is known as a dimensional reduction procedure and for quantum mechanics leads to an effective zero-dimensional theory.

Perturbation theory and its limitations

For $\lambda \ll 1$ it is natural to treat interactions perturbatively. In the following we illustrate this procedure by expanding the partition function

$$Z = \int_{-\infty}^{\infty} dx \exp\left(-\frac{1}{2}x^2 - \frac{\lambda}{4!}x^4\right) \tag{2.6}$$

in power series of the coupling constant λ. The series expansion reads

$$\begin{aligned} Z(n=\infty) &= \sum_{n=0}^{\infty} Z_n \lambda^n \\ Z_n &= \left(-\frac{1}{6}\right)^n \frac{\sqrt{2}}{n!}\Gamma\left(\frac{4n+1}{2}\right) \to_{n\gg 1} \left(-\frac{2n}{3e}\right)^n . \end{aligned} \tag{2.7}$$

We observe that no matter how small the coupling constant λ is, for sufficiently large order $n \gtrsim \frac{1}{\lambda}$ the summands $Z_n\lambda^n$ of the series become large.

Hence, we must conclude that the series (2.7) has zero radius of convergence around $\lambda = 0$. In fact, one can qualitatively understand it already from the form of Eq. (2.6): for $\lambda > 0$ ($\lambda < 0$) the integral is obviously convergent (divergent), leading to the breakdown of the series expansion around $\lambda = 0$.

Although the perturbation series does not converge, it is still very useful because it represents an asymptotic expansion. Roughly speaking, this means that for sufficiently small coupling constant λ the partial sum

$$Z(n_{opt}) = \sum_{n=0}^{n_{opt}} Z_n \lambda^n \tag{2.8}$$

approximates the exact partition function (2.6) very well. In order to find the optimal order n_{opt}, we note that the reminder (error) R_n of the partial sum can be estimated by

$$R_n = |Z - Z(n)| \leq |\lambda^{n+1} Z_{n+1}|. \tag{2.9}$$

The reminder is minimized as a function of n at

$$\left.\frac{dR}{dn}\right|_{n_{opt}} = 0 \tag{2.10}$$

yielding $n_{opt} = \frac{3}{2\lambda}$. The error of the perturbation theory of the order n_{opt} can be now estimated from Eq. (2.9) to be

$$R_{n_{opt}} \leq e^{-\frac{3}{2\lambda}}. \tag{2.11}$$

We conclude that for theories with $\lambda \ll 1$ the perturbative asymptotic expansion is very efficient and leads to tiny errors.

Derivation of the Wetterich flow equation

For $\lambda \gtrsim 1$ the perturbation theory is not very useful and a different (nonperturbative) method must be employed. This Section is devoted to the derivation of the Wetterich flow equation for the zero-dimensional model (2.5). Then we will discuss a concrete application of FRG to the zero-dimensional field theory in the next Sections.

For the purpose of derivation, first, we introduce a positive cutoff R into the generating function

$$Z(j, R) = \int_{-\infty}^{\infty} dx \exp\left(-\frac{1}{2}(1+R)x^2 - \frac{\lambda}{4!}x^4 + jx\right). \tag{2.12}$$

The full knowledge about the theory is more efficiently encoded in the Schwinger function $W(j,R) = \ln Z(j,R)$ which is a generating function of connected correlation functions. The main idea of the renormalization group method consists in studying how the theory is evolving under a continuous change of the cutoff R, i.e. we are interested in

$$\partial_R W(j,R) = -\int_{-\infty}^{\infty} dx \frac{x^2 \exp\left(-\frac{1}{2}(1+R)x^2 - \frac{\lambda}{4!}x^4 + jx\right)}{2Z(j,R)} = -\frac{1}{2}\langle x^2\rangle_{j,R}. \tag{2.13}$$

As was mentioned above, FRG deals with the effective flowing action which is defined via a modified Legendre transformation

$$\Gamma(x,R) = \underbrace{\sup_j \left(jx - W(j,R)\right)}_{\text{Legendre}} - \underbrace{\frac{1}{2}Rx^2}_{\text{modification}} . \tag{2.14}$$

The last term in Eq. (2.14) is introduced in order the effective action to have the correct ultraviolet limit

$$\Gamma(x, R=\Lambda\to\infty) - \Gamma(0, R=\Lambda\to\infty) \to S(x) = \frac{1}{2}x^2 + \frac{\lambda}{4!}x^4, \tag{2.15}$$

where $\Gamma(0,R)$ stands for the x-independent offset constant. Using Eqs. (2.13) (2.14) we obtain

$$\partial_R \Gamma(x,R) = \frac{1}{2}\left(\langle x^2\rangle_{j(x),R} - x^2\right) = \frac{1}{2}\langle x^2\rangle^{con}_{j(x),R}, \tag{2.16}$$

where the connected correlation function $\langle x^2\rangle^{con}_{j(x),R}$ was introduced. The field dependence of the source $j(x)$ can be inferred from the inversion of the relation $x = \partial_j W(j,R)$. To finish the derivation, we must express the RHS of Eq. (2.16) in terms of the effective average action, which can be done by noting

$$\langle x^2\rangle^{con}_{j(x),R} = \partial_j^2 W(j,R)\big|_{j=j(x)} = \left(\partial_x^2\Gamma(x,R) + R\right)^{-1}. \tag{2.17}$$

Putting Eqs. (2.16) and (2.17) together we arrive at the FRG flow equation for the toy model (2.5)

$$\partial_R \Gamma(x,R) = \frac{1}{2}\left(\partial_x^2\Gamma(x,R) + R\right)^{-1}. \tag{2.18}$$

This is a nonlinear partial differential equation defined in the domain $\{x,R\} = \{(-\infty,\infty),(0,\Lambda)\}$. To solve this equation one must provide the UV initial condition $\Gamma(x, R=\Lambda)$ and the boundary conditions $\Gamma(x=\pm\infty, R)$. The

analytical solution of the equation (2.18) is not known, but it can be readily solved numerically.

Now we would like to make a remark about the choice of initial conditions. As was stated above, for $\Lambda \to \infty$ the UV condition is simply given by the microscopic action (2.15) shifted by a x-independent offset. Note that for finite (but large) Λ, the initial condition must be modified. It reads

$$\Gamma(x, R = \Lambda) = \frac{1}{2}x^2 + \frac{\lambda}{4!}x^4 + \frac{1}{2}\ln\left(1 + \Lambda + \frac{\lambda}{2}x^2\right) \tag{2.19}$$

which has a form of a one-loop effective action in the presence of the cutoff $R = \Lambda$. To clarify the origin of the x-dependent modification term we note that for a large, but finite UV cutoff $R = \Lambda$, the integral (2.12) can be evaluated with the method of steepest descent. Subsequently, the resulting Schwinger function is substituted into Eq. (2.14) leading to the abovementioned result (2.19).

At this point one may rightfully ask whether we gained any advantage by transforming the integral representation (2.12) of the generating function $Z(j)$ into the partial differential equation (2.18) for the effective flowing action $\Gamma(x, R)$. Both are not tractable analytically and must be solved either approximately or numerically. We argue that the differential form is more flexible and useful for applications and also for comparison between different expansion schemes. This will be illustrated in the next Section, where different truncations of the effective flowing action of the zero-dimensional theory will be discussed.

Expansions and truncations

This Section is devoted to approximate solution of Eq. (2.18) by using different expansion schemes. In addition, we compare the approximate solutions with the "exact" numerical result.

Taylor expansion scheme

Our simplest approach consists in expanding the effective average action in the Taylor series around $x = 0$, i.e. we write

$$\Gamma(x, R) = \sum_{i=1}^{N_{max}=\infty} \frac{\lambda_{2i}(R)}{(2i)!}x^{2i} \tag{2.20}$$

with the cutoff-dependent Taylor coefficients $\lambda_{2i}(R)$. As the microscopic action $S(x)$ has Z_2 sign flip symmetry, the Taylor series (2.20) contains only

even powers of x. If $\Gamma(x,R)$ is analytic around $x=0$ as a function of x, then this representation is exact. Now, one can obtain a set of ordinary differential flow equations for the Taylor coefficients $\lambda_{2i}(R)$ from Eq. (2.18) by the following projection procedure

$$\lambda_{2i}(R) = \frac{d^{2i}}{dx^{2i}}\Gamma(x,R)\Big|_{x=0} \Rightarrow \partial_R \lambda_{2i}(R) = \frac{1}{2}\frac{d^{2i}}{dx^{2i}}\left(\partial_x^2\Gamma(x,R)+R\right)^{-1}\Big|_{x=0} \tag{2.21}$$

For example, for the lowest four Taylor coefficients we obtain

$$\begin{aligned}
\lambda_0'(R) &= \frac{1}{2\left(\lambda_2(R)+R\right)},\\
\lambda_2'(R) &= -\frac{\lambda_4(R)}{2\left(\lambda_2(R)+R\right)^2},\\
\lambda_4'(R) &= \frac{1}{2}\left(\frac{6\lambda_4(R)^2}{\left(\lambda_2(R)+R\right)^3} - \frac{\lambda_6(R)}{\left(\lambda_2(R)+R\right)^2}\right),\\
\lambda_6'(R) &= \frac{1}{2}\left(-\frac{90\lambda_4(R)^3}{\left(\lambda_2(R)+R\right)^4} + \frac{30\lambda_6(R)\lambda_4(R)}{\left(\lambda_2(R)+R\right)^3} - \frac{\lambda_8(R)}{\left(\lambda_2(R)+R\right)^2}\right).
\end{aligned} \tag{2.22}$$

We observe that a higher-order coupling $\lambda_{2(i+1)}$ always appears on the RHS of the flow equation for a coupling λ_{2i}. This pattern repeats itself also for $i>3$. We conclude that for an exact treatment one must solve an infinite tower of RG flow equations for all couplings λ_{2i}, $i=1,2,\ldots,\infty$. In practice one truncates the set of equations by taking a finite N_{max} in Eq. (2.20). This amounts to fixing $\lambda_{2i}(R)$ to zero for $i>N_{max}$, i.e. one ignores the influence of the higher-order couplings with $i>N_{max}$ on the RG flows of λ_{2i} with $i\leq N_{max}$.

The truncated set of flow equations is nonlinear and must be solved numerically. For illustrative purposes, we solved the truncated set of flow equations for $N_{max}=2,3,4,5$ and the UV initial conditions $\lambda_2(\Lambda)=1$, $\lambda_4(\Lambda)=10^2$, $\lambda_{2i>4}(\Lambda)=0$ for $\Lambda=10^{10}$.[6] Our result is plotted in Figure 2.2 in blue and is compared with the microscopic action (green) and the full numerical solution (red). The latter is obtained by the numerical evaluation of Eq. (2.12) and subsequent numerical Legendre transformation of the resulting $\ln Z(j,R=0)$.

We observe that the Taylor expansion approximates the "exact" solution well for $x\ll 1$. However, for the values of $x\gtrsim 1$ the expansion becomes inaccurate. Note that by increasing the order N_{max} one does not improve the result for $x\gtrsim 1$. Hence, while the Taylor expansion becomes more and

[6]Note that due to the extremely large value of Λ we can safely neglect the logarithmic term in Eq. (2.19).

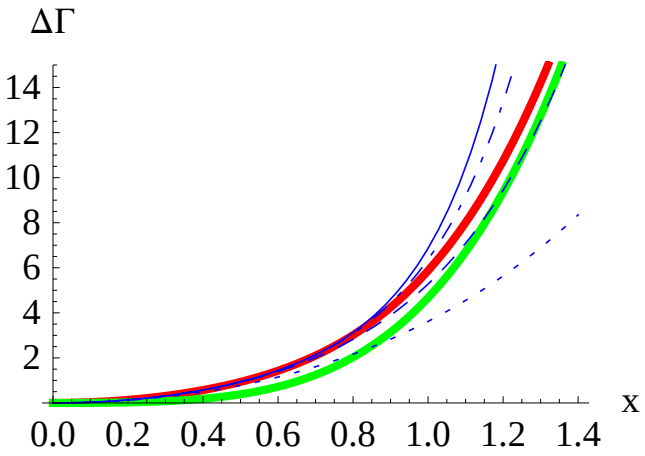

Figure 2.2: Shifted average action $\Delta\Gamma(x) = \Gamma(x) - \Gamma(0)$: exact numerical solution (red), Taylor $N_{max} = 2$ (blue, dotted), Taylor $N_{max} = 3$ (blue, dashed), Taylor $N_{max} = 4$ (blue, dot dashed), Taylor $N_{max} = 5$ (blue, solid). For comparison the microscopic action $S(x)$ is plotted in green.

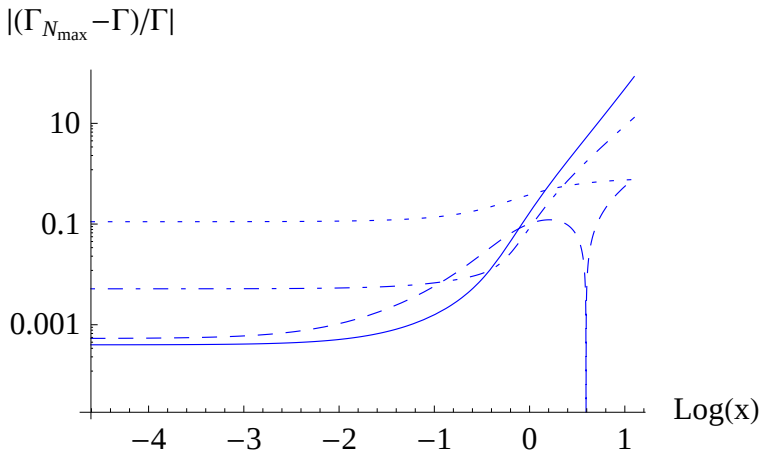

Figure 2.3: Relative error $|\frac{\Gamma_{N_{max}} - \Gamma}{\Gamma}|$: Taylor $N_{max} = 2$ (blue, dotted), Taylor $N_{max} = 3$ (blue, dashed), Taylor $N_{max} = 4$ (blue, dot dashed), Taylor $N_{max} = 5$ (blue, solid).

more accurate around $x = 0$ for higher N_{max}, it fails for large values of x. This becomes especially clear from Figure 2.3, where the relative error of the Taylor expansion is depicted in the plot with a double logarithmic scale. The reason why the truncated Taylor expansion fails for large x constitutes simply in its local nature. By increasing the order N_{max} one improves the local quality of the approximation. The global features of the exact solution, however, are not taken into account properly.

Iteration scheme

Alternatively, one can solve Eq. (2.18) by iteration. For this purpose, we start with the zeroth approximation given by

$$\Gamma_{(0)}(x, R) = S(x) = \frac{1}{2}x^2 + \frac{\lambda}{4!}x^4, \tag{2.23}$$

i.e. the effective flowing action is set to be equal to the microscopic action. This input is substituted now to the RHS of the flow equation (2.18) yielding the differential equation for the first approximation $\Gamma_{(1)}$

$$\partial_R \Gamma_{(1)}(x, R) = \frac{1}{2}\frac{1}{\partial_x^2 S(x) + R} = \frac{1}{2}\frac{1}{1 + \frac{\lambda}{2}x^2 + R} \tag{2.24}$$

which can be easily integrated analytically. Using the UV initial condition (2.19) we obtain

$$\begin{aligned} \Gamma_{(1)}(x, R) &= S(x) + \frac{1}{2}\ln(\partial_x^2 S + R) \\ &= \frac{1}{2}x^2 + \frac{\lambda}{4!}x^4 + \frac{1}{2}\ln\left(1 + \frac{\lambda}{2}x^2 + R\right) \end{aligned} \tag{2.25}$$

which for $R = 0$ (in the IR) is exactly the one-loop effective action. In other words, in the first iteration all one-loop Feynman diagrams that contribute to the full effective action are resumed.

In the following step we substitute $\Gamma_{(1)}$ to the RHS of the flow equation (2.18) and obtain

$$\begin{aligned} \partial_R \Gamma_{(2)} &= \frac{1}{2}\frac{1}{\partial_x^2 \Gamma_{(1)}(x, R) + R} \\ &= \frac{1}{2}\frac{1}{1 + \frac{\lambda}{2}x^2 + R}\frac{1}{1 + 2\lambda\frac{2 - \lambda x^2 + 2R}{(2 + \lambda x^2 + 2R)^3}} \end{aligned} \tag{2.26}$$

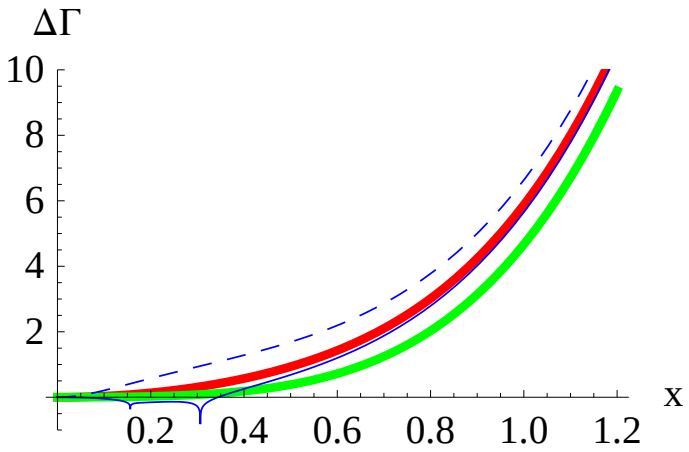

Figure 2.4: Shifted average action $\Delta\Gamma(x) = \Gamma(x) - \Gamma(0)$: exact numerical solution (red), first iteration (blue, dashed), second iteration (blue, solid). For comparison the microscopic action $S(x)$ is plotted in green.

that can be still evaluated analytically.[7]

In principle, it is (at least numerically) straightforward to repeat the iteration procedure described above and generate the higher iterations $\Gamma_{(n)}$. Here we show the result for the first two iterations and compare it with the full numerical solution. We impose the same UV initial conditions as were used in the previous subsection, namely $\lambda = 10^2$, $\Lambda = 10^{10}$.

In Figure 2.4 we depicted the shifted iterative effective actions $\Delta\Gamma_{(1)}$ (blue, dashed), $\Delta\Gamma_{(2)}$ (blue, solid) and the full numerical result (red). The relative error of the first two iterations $\Delta\Gamma_{(1)}$ and $\Delta\Gamma_{(2)}$ is plotted in Figure 2.5. It is remarkable that, while for $x \lesssim 1$ the iterative scheme turns out to be very inaccurate, it approximates the "exact" solution very well for $x \gtrsim 1$. This is in a start contrast to the Taylor expansion discussed in the previous subsection which was local and thus accurate only for $x \to 0$. In general, we expect that for $x \gg 1$ the higher iterations $\Gamma_{(n)}$ become better and better for the increasing order n.

[7]Let us note at this point that the second iteration $\Gamma_{(2)}(x, R)$ includes not only two-loop Feynman diagrams, but also some of the higher-loop contributions. We can see it by introducing the loop counting factor "$\hbar$" into the flow equation (2.18) and counting powers of "$\hbar$".

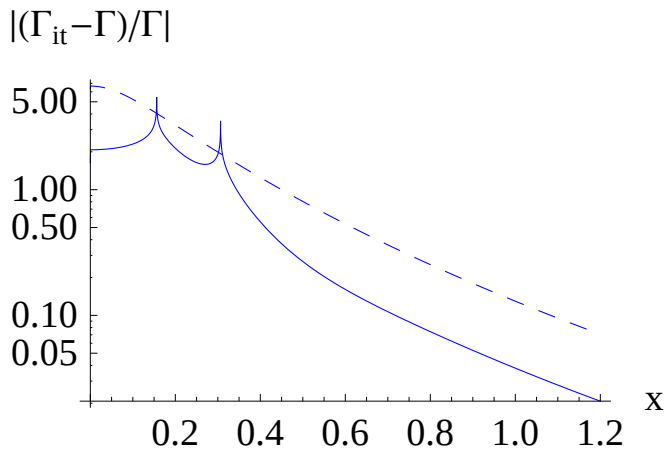

Figure 2.5: Relative error $|\frac{\Gamma_{it}-\Gamma}{\Gamma}|$: first iteration (blue, dashed), second iteration (blue, solid).

Mixed scheme

In previous subsections two distinct expansion schemes were analyzed. We found that the local Taylor expansion is a good approximation for $x \ll 1$, while the iterative solution turns out to be very accurate for $x \gg 1$. Here we introduce the mixed scheme which combines the advantages of the Taylor and iterative solutions, i.e. it becomes accurate for both $x \ll 1$ and $x \gg 1$. To this end we expand the effective flowing action as

$$\Gamma(x,R) = S(x) + \frac{1}{2}\ln\left(\partial_x^2 S + R\right) + \sum_{i=0}^{N_{max}=\infty} \frac{\lambda_{2i}(R)}{(2i)!}\frac{x^{2i}}{(\partial_x^2 S(x)+R)^{i+2}}. \quad (2.27)$$

The first two terms in this equation simply constitute the one-loop effective action. The third term is designed in a way that it resembles the Taylor expansion for $x \ll 1$, while for $x \gg 1$ it is suppressed as $\sim \frac{1}{x^4}$.

By differentiating the flow equation (2.18) at $x = 0$, it is now straightforward to get an (infinite) coupled set of ordinary differential equations for the couplings $\lambda_{2i}(R)$, $i = 0, 1, \ldots, \infty$. We truncated the tower of flow equations taking $N_{max} = 2, 3, 4, 5$ and solved the corresponding (finite) set of differential equations numerically. The UV initial conditions $\lambda(\Lambda) = 1$, $\lambda_{2i>0} = 0$ and $\Lambda = 10^3$ were used. The relative error[8] of the mixed truncation scheme compared to the full numerical result is depicted in Figure 2.6. As expected, the error becomes tiny for $x \ll 1$ and $x \gg 1$. The convergence properties

[8] plotted using the linear and logarithmic scales

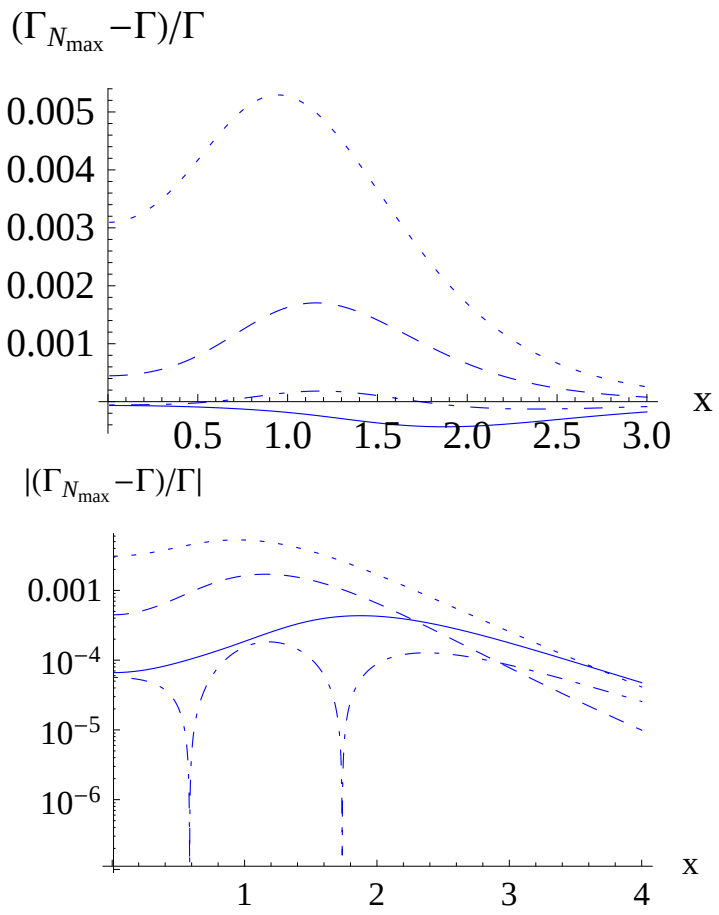

Figure 2.6: Relative error $|\frac{\Gamma_{N_{max}}-\Gamma}{\Gamma}|$:mixed $N_{max} = 2$ (blue, dotted), mixed $N_{max} = 3$ (blue, dashed), mixed $N_{max} = 4$ (blue, dot dashed), mixed $N_{max} = 5$ (blue, solid).

of the expansion, however, are not under control. For example, it is clear from Figure 2.6 that the $N_{max} = 5$ truncation is worse than the $N_{max} = 4$ truncation, since the corresponding relative error for $N_{max} = 5$ is bigger that the error for $N_{max} = 4$ for any $x \in (0, 4)$. It is desirable to design an expansion with good convergence properties. For such expansion the higher-order truncation should approximate the exact result better than any lower-order truncation.

No spontaneous symmetry breaking in zero dimensions

Spontaneous symmetry breaking (SSB) is a very important concept in modern theoretical physics. It is a key notion in the theory of phase transitions in statistical physics. Roughly speaking, a symmetry is broken spontaneously if the full effective action respects it, but the vacuum (ground) state is not invariant under the symmetry transformation. In this Section we demonstrate that no spontaneous symmetry breaking is possible in any reasonable zero-dimensional field theory. In order to prove this it is sufficient to notice that the generating function $Z(j)$ (2.5) and the Schwinger function $W(j)$ are smooth (differentiable) functions of the source j.[9] The proof of the smoothness of $Z(j)$ (under very mild assumptions about the microscopic action $S(x)$) can be found in Appendix A. It is important to stress that the proof does not hold in higher dimensions $d \geq 1$ due to infinite dimensionality of the functional Feynman integral which defines the generating functional $Z[j]$. In other words, phase transitions are possible in $d \geq 1$, but only in the thermodynamic (infinite volume) limit.

It is instructive to study in some detail how the absence of spontaneous symmetry breaking in a zero-dimensional field theory is encoded in the FRG equation for the effective flowing action. As a simple example, consider the microscopic action of the form

$$S(x) = \frac{\lambda}{4!}\left(x^2 - x_0^2\right)^2, \qquad \lambda > 0. \tag{2.28}$$

This action has two degenerate minima at $x = \pm x_0$ and a maximum at $x = 0$. The classical ground state is associated with a minimum of $S(x)$. Since the minima at $x = -x_0$ and $x = x_0$ are degenerate, the classical ground state

[9]Indeed, the nonanalyticities of $W(j)$ are directly related to phase transitions and thus to a spontaneous symmetry breaking. Specifically, if the first derivative of $W(j)$ undergoes a discontinuous jump, then we are dealing with the first order phase transition. If the second (or higher) derivative of $W(j)$ is not continuous, then the associated phase transition is called a continuous phase transition.

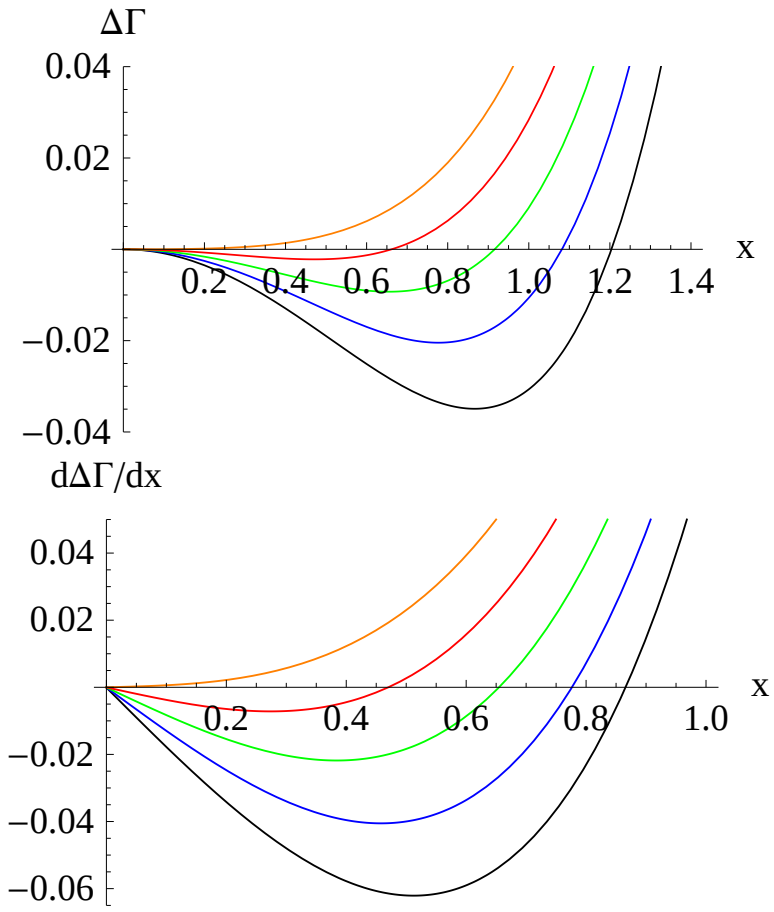

Figure 2.7: Snapshots of $\Delta\Gamma(x, \exp(T))$ and its derivative for $T = 0.5$ (black), $T = 0.4$ (blue), $T = 0.3$ (green), $T = 0.2$ (red), $T = 0.1$ (orange) for $x > 0$.

must "choose" one of them, and in this way it breaks spontaneously the discrete Z_2 sign flip symmetry.

Since there is no spontaneous symmetry breaking in any zero-dimensional field theory, the full solution must differ substantially from the classical picture described above. The transition from the microscopic classical action to the full effective action can be naturally studied with the Wetterich flow equation (2.18). The snapshots of the numerical solution $\Delta\Gamma(x, R)$ and its derivative $\frac{d\Delta\Gamma(x,R)}{dx}$ for different values of the cutoff R are plotted in Figure 2.7. As the UV initial conditions we used $\lambda(\Lambda) = 3$, $x_0(\Lambda) = \sqrt{2}$ and $\Lambda = 10^3$. The effective flowing action undergoes a transition from the regime with two degenerate minima (SSB) to the symmetric (SYM) regime with a

single global minimum located at the origin $x = 0$. This evolution of the effective flowing action $\Gamma(x, R)$ provides a simple explanation of how spontaneous symmetry breaking is avoided in a zero-dimensional field theory.

Another feature of the full effective action which becomes obvious from Figure 2.7 is convexity. Since the effective action is defined as a Legendre transformation of the (necessarily) convex Schwinger functional $W(j)$

$$\Gamma(x) = \sup_j \left(jx - W(j) \right), \tag{2.29}$$

it must be convex as well. For this reason it can not have a double well structure of the microscopic action $S(x)$ in Eq. (2.28). One can directly see how convexity is acquired during the renormalization group flow. Finally, we note that convexity is a general feature of the effective potential of a field theory in any number of dimensions. The general proof of this statement can be found in [26].

In the reminder of this Section we study a transition from the SSB regime in the ultraviolet to the SYM regime in the infrared employing a simple truncation

$$\Delta\Gamma(\rho, R) = m^2(R)[\rho - \rho_0(R)] + \frac{\lambda(R)}{2}[\rho - \rho_0(R)]^2 \tag{2.30}$$

with $\Delta\Gamma(\rho, R) = \Gamma(\rho, R) - \Gamma(\rho_0, R)$, $\rho \equiv \frac{1}{2}x^2$ and $\rho_0 \equiv \frac{1}{2}x_0^2$.[10] The truncation (2.30) is universal in the sense that it can be used in both SSB and SYM regimes. In particular, in the SSB regime by definition $\frac{d\Delta\Gamma}{d\rho}\Big|_{\rho=\rho_0} = 0$ which implies that necessarily $m(R) \equiv 0$. On the other hand, in the SYM regime the effective flowing action has just a single global minimum at $\rho = 0$ leading to $\rho_0(R) \equiv 0$. In other words, the truncation (2.30) can be expressed as

$$\begin{aligned} &m^2(R) = 0 \Rightarrow \Delta\Gamma(\rho, R) = \frac{\lambda(R)}{2}[\rho - \rho_0(R)]^2 \quad \text{SSB}, \\ &\rho_0(R) = 0 \Rightarrow \Delta\Gamma(\rho, R) = m^2(R)\rho + \frac{\lambda(R)}{2}\rho^2 \quad \text{SYM}. \end{aligned} \tag{2.31}$$

It is now straightforward to derive the flow equations for the running couplings of the truncation (2.30). In the SSB regime we obtain

$$\begin{aligned} \partial_T \rho_0 &= -\frac{\partial_\rho \partial_T \Delta\Gamma}{\partial_\rho^2 \Delta\Gamma}\Big|_{\rho=\rho_0} = \frac{3R}{2(R + 2\lambda\rho_0)^2}, \\ \partial_T \lambda &= \partial_\rho^2 \partial_T \Delta\Gamma\Big|_{\rho=\rho_0} = \frac{9R\lambda^2}{(R + 2\lambda\rho_0)^3}, \end{aligned} \tag{2.32}$$

[10] Notice that here we rescaled the coupling λ by a constant multiplicative factor $\lambda \to 3\lambda$ compared to Eqs. (2.23), (2.28). We hope that this will not lead to confusion.

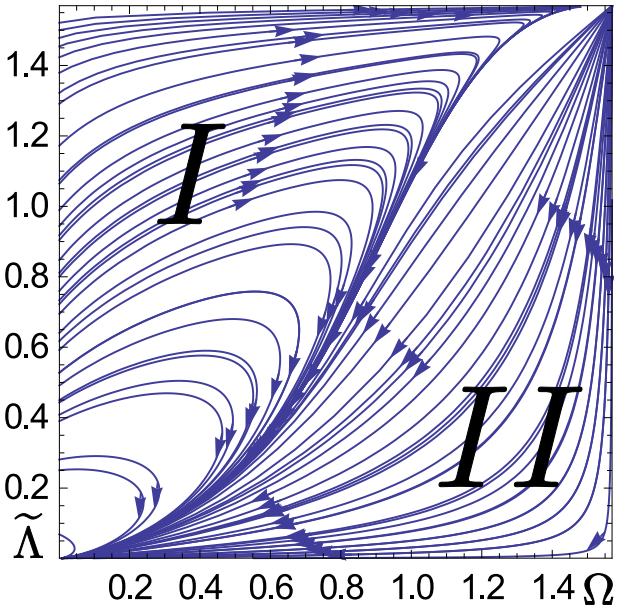

Figure 2.8: Phase portrait of the renormalization group flow in the SSB regime. Arrows denote the direction towards the UV.

where we introduced $T = \ln R$. We aim to investigate the fixed point structure of these flow equations. For this reason, it is now convenient to transform to the "dimensionless" couplings $\omega \equiv \frac{2\lambda\rho_0}{R}$ and $\widetilde{\lambda} \equiv \frac{\lambda}{R^2}$. The flow equations for ω and $\widetilde{\lambda}$ read

$$\begin{aligned} \partial_T \omega &= -2\omega + \frac{3\widetilde{\lambda}(4\omega+1)}{(1+\omega)^3}, \\ \partial_T \widetilde{\lambda} &= \widetilde{\lambda}\left(-2 + \frac{9\widetilde{\lambda}}{(1+\omega)^3}\right). \end{aligned} \tag{2.33}$$

In order to understand the topology of the RG flow in the SSB regime, we solve the nonlinear system (2.33) numerically. The phase portrait of the RG trajectories is depicted in Figure 2.8. In this Figure arrows point in the UV direction. To make the domain of the phase portrait finite we introduced rescaled variables

$$\begin{aligned} \Omega \in [0, \frac{\pi}{2}], \qquad & \omega = \tan\Omega, \\ \widetilde{\Lambda} \in [0, \frac{\pi}{2}], \qquad & \widetilde{\lambda} = \tan\widetilde{\Lambda}. \end{aligned} \tag{2.34}$$

The RG flow plotted in Figure 2.8 has an ultraviolet attractive Gaussian fixed point. In our truncation the whole domain of the RG evolution can

be naturally divided into two regions (denoted by I and II in the Figure). Remarkably, every trajectory in the region I leaves the SSB regime (while evolving towards infrared) and enters the SYM phase as it crosses the boundary at $\Omega = 0$. This is consistent with our general finding that there is no spontaneous symmetry breaking in zero-dimensional field theory. On the other hand, in the region II every trajectory is attracted by the infrared fixed point at $(\Omega = \frac{\pi}{2}, \widetilde{\Lambda} = \frac{\pi}{2})$. The "dimensionful" couplings ρ_0 and λ approach fixed finite values in the IR in this regime. We believe that this is an artifact of the simple truncation (2.30). We expect that for a proper treatment of RG flows with initial conditions located in the region II some more elaborate (for example higher polynomial) truncation must be used.

Similar steps can be repeated in the SYM regime. The flow equations for m^2 and λ are given now by

$$\begin{aligned} \partial_T m^2 &= \partial_\rho \partial_T \Delta\Gamma\Big|_{\rho=\rho_0} = -\frac{3R\lambda}{2(m^2+R)^2}, \\ \partial_T \lambda &= \partial_\rho^2 \partial_T \Delta\Gamma\Big|_{\rho=\rho_0} = \frac{9R\lambda^2}{(m^2+R)^3}. \end{aligned} \tag{2.35}$$

For the "dimensionless" version $\widetilde{m}^2 = \frac{m^2}{R}$ and $\widetilde{\lambda} = \frac{\lambda}{R^2}$ we get

$$\begin{aligned} \partial_T \widetilde{m}^2 &= -\widetilde{m}^2 - \frac{3\widetilde{\lambda}}{2(1+\widetilde{m}^2)^2}, \\ \partial_T \widetilde{\lambda} &= \widetilde{\lambda}\left(-2 + \frac{9\widetilde{\lambda}}{(1+\widetilde{m}^2)^3}\right). \end{aligned} \tag{2.36}$$

We solved the flow equations (2.36) numerically and the phase portrait of RG trajectories in the SYM regime is plotted in Figure 2.9. Here we rescaled the variables to make their domain of definition finite. Following our treatment of the SSB regime, the rescaling is done in the following way

$$\begin{aligned} M \in [0, \frac{\pi}{2}], \qquad & m^2 = \tan M, \\ \widetilde{\Lambda} \in [0, \frac{\pi}{2}], \qquad & \widetilde{\lambda} = \tan \widetilde{\Lambda}. \end{aligned} \tag{2.37}$$

We observe that in the IR all trajectories approach the IR attractive fixed point at $(M = \frac{\pi}{2}, \widetilde{\Lambda} = \frac{\pi}{2})$. The corresponding "dimensionful" variables m^2 and λ approach finite values in the IR.

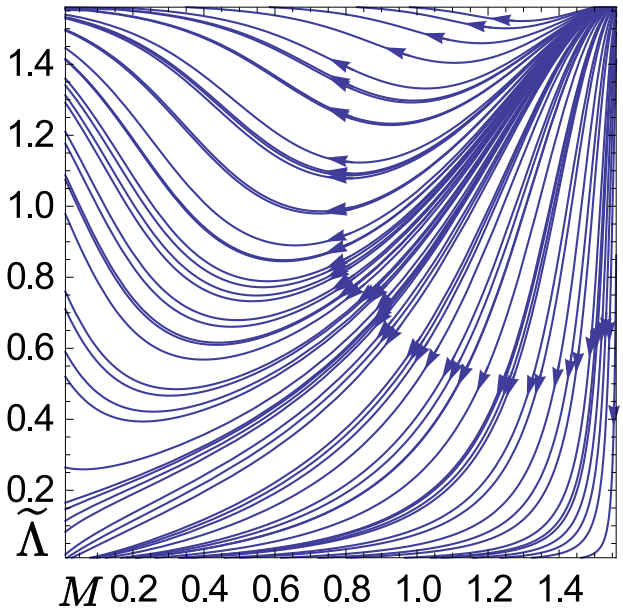

Figure 2.9: Phase portrait of the renormalization group flow in the SYM regime. Arrows denote the direction towards the UV.

Chapter 3

Quantum Mechanics with Inverse Square Potential

Exactly solvable problems play an important role in physics. They provide a backbone of our understanding and allow to develop perturbation theory on the basis of an exact solution. In nonrelativistic quantum mechanics the harmonic oscillator and the Coulomb central potential are certainly the two most important examples. Another prominent example of an exactly solvable problem in quantum mechanics is the central, inverse square potential

$$V(r) = -\frac{\kappa}{r^2}. \tag{3.1}$$

Most remarkably, in any spatial dimension the potential (3.1) is classically scale invariant because it is a homogeneous function of degree -2 and has the same scaling as the nonrelativistic kinetic energy. Hence, the classical action is invariant under the nonrelativistic scaling $\vec{r} \to \rho\vec{r}$, $t \to \rho^2 t$. The quantum problem with the potential (3.1) has a long history and is discussed both in textbooks [27, 28] and in the scientific literature [29, 30]. More recently there were a number of renormalization group (RG) studies of this problem [31, 32, 33, 34, 35, 36, 37, 38, 39, 40, 41].

The quantum physics of the inverse square potential is well understood. The interaction (3.1) is an example of a singular potential [42] and must be treated with care. It is known that for the repulsive and weakly attractive coupling ($\kappa < \kappa_{cr}$)[1], the scale symmetry is preserved at the quantum level and the theory provides an example of nonrelativistic conformal field theory [43]. On the other hand, for strong attractions ($\kappa > \kappa_{cr}$) a discrete, geometric bound state spectrum develops in the two-body problem, and the continuous

[1] κ_{cr} represents the critical attractive coupling. In d spatial dimensions it is given by $\kappa_{cr} = \frac{(d-2)^2}{4}$.

scale symmetry is broken to a discrete subgroup by a quantum anomaly [44]. The anomaly has its origin in the singular short-distance behavior of the inverse square potential. As will be discussed many times in this thesis, in the RG language the anomaly manifests itself as a limit cycle instead of a scale-invariant fixed point.

In this thesis we start our discussion with the inverse square potential problem, since it is a paradigmatic system for nonrelativistic conformal invariance and scale anomaly. Remarkably, there is a number of different physical systems, which are described (often only in some restricted domain) by the inverse square potential:

- The celebrated Efimov effect, first derived in [3], consists in the formation of a tower of three-body bound states of identical nonrelativistic bosons[2] interacting through a short range potential. Exactly at resonance (unitarity regime) all scales drop out of the problem and the three-body spectrum becomes infinite and geometric. The three-body problem in quantum mechanics is treated most easily in hyperspherical coordinates [6]. Employing the adiabatic hyperspherical approximation [45], Faddeev decomposition of the wave function [46] and restricting to the zero total angular momentum sector, one arrives at the remarkably simple one-dimensional effective equation [1]

$$\left[-\frac{d^2}{dr^2} - \frac{s_0^2 + 1/4}{r^2}\right]\psi(r) = E\psi(r) \tag{3.2}$$

  with the Efimov parameter $s_0 \approx 1.0062$. This is a one-dimensional radial Schrödinger equation with the inverse square potential in the overcritical regime ($\kappa > \frac{1}{4}$). Our FRG studies of the Efimov effect are described in detail in Chapters 4 and 5.

- The interaction of a polar molecule with an electron in three spatial dimensions can be approximated by a point dipole-charged particle anisotropic potential

$$V(\vec{r}) \sim \frac{\cos\theta}{r^2}, \tag{3.3}$$

  where the angle θ is measured with respect to the direction of the dipole moment. As was demonstrated in [47], this anisotropic conformal potential can be reduced to the effective isotropic inverse potential (3.1) in the zero angular-momentum channel. Remarkably, the dipole-electron

[2]More generally, for the occurrence of the Efimov effect it is sufficient that at least two two-body subsystems have s-wave bound states close to the zero-energy threshold unless two of the three particles are identical fermions.

system exhibits all interesting features characteristic for the potential (3.1).

- At the critical coupling κ_{cr} the theory undergoes a transition from the conformal ($\kappa < \kappa_{cr}$) to the nonconformal ($\kappa > \kappa_{cr}$) regime. It has been demonstrated recently in [41] that this transition is closely related to the classical Berezinskii-Kosterlitz-Thouless (BKT) phase transition in two dimensions. In particular, the energy B of the lowest bound state near the critical coupling κ_{cr} in the nonconformal regime vanishes like

$$B \sim \exp\left(-\frac{\pi}{\sqrt{\kappa - \kappa_{cr}}}\right) \tag{3.4}$$

  which is analogous to the behavior of the inverse correlation length as the BKT transition temperature is approached form above [48].

- Quite unexpectedly, the inverse square potential arises in the near-horizon physics of some black holes. More specifically, this is the case for a massive, scalar field minimally coupled to gravity on the nonextremal spherically-symmetric Reissner-Nordström (RN) black hole background. It was demonstrated in [44] that the Klein-Gordon field equation of the scalar field reduces to the effective Schrödinger equation with the overcritical ($\kappa > \kappa_{cr}$) inverse square potential in the near-horizon limit. The related problem of a scalar particle near an extremal RN black hole was treated in [49] leading to a similar finding.

- Finally, the conformal inverse square potential appears naturally in the context of vacuum AdS/CFT correspondence [50]. The field equation for a scalar field ϕ of mass m in the Euclidean AdS_{d+1} is

$$\partial_r^2\phi - \frac{d-1}{r}\partial_r\phi - \frac{m^2}{r^2}\phi - q^2\phi = 0, \qquad q^2 = (q^0)^2 + \vec{q}^2, \tag{3.5}$$

  where we transformed to the momentum space on the AdS_{d+1} boundary $(x^0, \vec{x}) \to (q^0, \vec{q})$, and r denotes the radial direction in the AdS_{d+1} space. We can change variable $\phi = r^{(d-1)/2}\psi$ and obtain

$$-\partial_r^2\psi + \frac{m^2 + (d^2-1)/4}{r^2}\psi = -q^2\psi, \tag{3.6}$$

  which is a one-dimensional Schrödinger equation with an inverse square potential of strength $\kappa = -m^2 - \frac{d^2-1}{4}$ and energy $E = -q^2$. As was emphasized in [41, 51], the overcritical coupling $\kappa > \kappa_{cr}$ corresponds to the violation of the Breitenlohner-Freedman bound in AdS_{d+1}.

In this Chapter we present our study of the quantum problem with the inverse square potential using functional renormalization. First, in Section 3.1 we introduce the physical system of interest and derive the flow equations using a sharp cutoff regulator. A general mathematical discussion of the flow equation is performed in Section 3.2. Our central result is derived in Section 3.3, where we extend the analysis to the complex plane, discuss the fixed point structure and find a numerical solution of the extended set of flow equations. Additionally, we provide a physical interpretation, geometric description and motivation for the complex extension. In Section 3.4 we bosonize the interaction. This allows us to view the problem from a different angle and, most remarkably, obtain an analytic solution of the generalized complex flow equations. Finally, in Section 3.5 we present the renormalization group flows on the Riemann sphere.

Let us note that the physically more interesting three-body quantum problem for fermions and bosons will be discussed in detail in Chapter 4. In the present Chapter we solve an arguably much simpler problem. The aim of this Chapter is twofold. First, the inverse square potential is a paradigm and it is important for understanding of other, more challenging problems. Second, by working with this simple system, it is easy to develop and illustrate a new renormalization group method of complexified flows.

3.1 The model and the flow equation

Here we study the nonrelativistic quantum mechanical problem of identical bosons interacting through a long-range potential (3.1) in d spatial dimensions. The many-body field theory is defined in the UV by the microscopic action S_E

$$\begin{aligned} S_E[\psi,\psi^*] = &\int_0^{1/T} d\tau \int d^dx \psi^*(\tau,\vec{x})[\partial_\tau - \Delta - \mu]\psi(\tau,\vec{x}) \\ &- \frac{\lambda_\psi}{2}\int_0^{1/T} d\tau d^dx \psi^*(\tau,\vec{x})\psi^*(\tau,\vec{x})\psi(\tau,\vec{x})\psi(\tau,\vec{x}) \\ &- \int_0^{1/T} d\tau \int d^dx d^dy \psi^*(\tau,\vec{x})\psi^*(\tau,\vec{y})\frac{\kappa}{|\vec{x}-\vec{y}|^2}\psi(\tau,\vec{y})\psi(\tau,\vec{x}). \end{aligned} \tag{3.7}$$

Our convention is $\hbar = 2M_\psi = 1$ with the boson mass M_ψ. We work in the imaginary-time formalism with Euclidean time $\tau \in (0, 1/T)$. In what follows we will be interested exclusively in the few-body (vacuum) physics. The vacuum state is characterized by zero density, which corresponds to zero chemical potential ($\mu = 0$), and zero temperature ($T = 0$). The bare action

(3.7) is invariant under a global $U(1)$ transformation and possesses Galilean spacetime symmetry.[3] The microscopic bare parameter κ characterizes the strength of the long-range potential and is positive in the attractive case. We augmented the theory by a four-boson contact interaction term with a coupling λ_ψ. This is a consequence of the fact that the inverse square potential is singular at the origin [29, 42]. On its own the singular potential is not sufficient to define a quantum mechanical problem and must be augmented by the boundary condition at the origin [41]. We will see that the introduction of λ_ψ in the UV determines the $r = 0$ boundary condition and makes the problem well-defined.

For our method it is convenient to switch to momentum space. The Fourier transform of the $1/r^2$ potential in d spatial dimensions reads

$$\begin{aligned} F_d(l) &= \int d^d r \frac{1}{r^2} \exp[i\vec{l}\cdot\vec{r}] = (2\pi)^{d/2}|\vec{l}|^{2-d}\int_0^\infty dz z^{d/2-1}J_{d/2-1}(z) = \\ &= \frac{(4\pi)^{d/2}\Gamma(d/2-1)|\vec{l}|^{2-d}}{4}, \qquad 2<d<5. \end{aligned} \tag{3.8}$$

The restriction to dimensions d in the range $2 < d < 5$ can be understood easily by the fact that on the one side, $d = 2$ is a natural lower dimension, in which the integral (3.8) is IR logarithmically divergent. On the other side, the upper bound $d = 5$ can be relaxed, if we modify the Fourier integral by the introduction of a UV suppression factor $\exp(-\epsilon|\vec{r}|)$ and perform the limit $\epsilon \to 0$ in the very end. Hence, we will use

$$F_d(l) = \frac{(4\pi)^{d/2}\Gamma(d/2-1)|\vec{l}|^{2-d}}{4}, \quad d>2. \tag{3.9}$$

In what follows we consider only $d > 2$.

First, we consider a momentum-independent (pointlike) truncation for the flowing action

$$\begin{aligned} \Gamma_k[\psi,\psi^*] &= \int_Q \psi^*(Q)[i\omega+\vec{q}^2]\psi(Q) \\ &- \kappa\int_{Q_1,Q_2,\ldots,Q_4} F_d(l)\psi^*(Q_1)\psi(Q_2)\psi^*(Q_3)\psi(Q_4)\delta(-Q_1+Q_2-Q_3+Q_4) \\ &- \frac{\lambda_\psi}{2}\int_{Q_1,Q_2,\ldots,Q_4} \psi^*(Q_1)\psi(Q_2)\psi^*(Q_3)\psi(Q_4)\delta(-Q_1+Q_2-Q_3+Q_4), \end{aligned} \tag{3.10}$$

[3]Some details about Galilean symmetry are summarized in Appendix B.

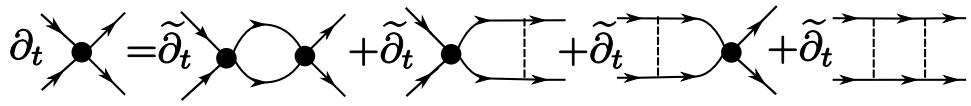

Figure 3.1: Flow equation of the four-particle contact coupling λ_ψ in form of Feynman diagrams. The solid lines with an arrow denote the boson ψ regularized propagator, the dashed lines correspond to the long-range interaction vertex, and the dark blobs represent the contact coupling λ_ψ.

where $Q = (\omega, \vec{q})$ and $\int_Q = \int \frac{d\omega}{2\pi} \int \frac{d^d q}{(2\pi)^d}$. The vector $\vec{l} = \vec{q}_2 - \vec{q}_1 = \vec{q}_3 - \vec{q}_4$ gives the spatial momentum transfer during a collision and $l = |\vec{l}|$. In the nonrelativistic vacuum the propagator of the elementary field ψ is not renormalized because the only diagram, which contributes to its flow, contains a hole (antiparticle) in the loop. Since there are only particles but no holes as excitations of the nonrelativistic vacuum, the propagator keeps its microscopic form. Remarkably, the coupling κ, characterizing the strength of the long-range $1/r^2$ potential, is also constant during the renormalization group flow (we discuss this issue in more detail in Section 3.4). The only coupling which flows during the RG evolution in our truncation is the contact coupling λ_ψ. Its flow equation is

$$\partial_t \lambda_\psi = \int_L \widetilde{\partial}_t \frac{[\lambda_\psi + 2F_d(l)\kappa]^2}{(i\omega + l^2 + R_k(L))(-i\omega + l^2 + R_k(-L))}, \tag{3.11}$$

where $\partial_t = k\partial_k$ and $\widetilde{\partial}_t$ is a scale derivative which acts only on the IR regulator R_k. The flow equation is depicted in terms of Feynman diagrams in Figure 3.1. In order to proceed further we must specify the cutoff function $R_k(L)$.

Nevertheless, we note that already at this point it is possible to identify the generic form of the flow equation which reads

$$\partial_t \lambda_\psi = \alpha \lambda_\psi^2 + \beta \lambda_\psi + \gamma \tag{3.12}$$

with $\alpha, \beta, \gamma \in \mathbb{R}$, which depend on the coupling κ, dimension d and a concrete choice of the cutoff function. We postpone the general analysis of equation (3.12) until Section 3.2.

It is convenient to rewrite Eq. (3.11) as

$$\partial_t \lambda_\psi = J_{0,d} \lambda_\psi^2 + 4J_{1,d}\kappa\lambda_\psi + 4J_{2,d}\kappa^2, \tag{3.13}$$

where we defined the cutoff dependent integrals

$$J_{n,d} \equiv \int \frac{d\omega}{2\pi} \frac{d^d l}{(2\pi)^d} \partial_t \frac{F_d^n(l)}{(i\omega + l^2 + R_k(L))(-i\omega + l^2 + R_k(-L))}, \tag{3.14}$$

where $F_d^n(l) \equiv F_d(l)^n$.

In the rest of this Section we finish the computation by specifying the sharp regulator $R_k(L) = (i\omega+l^2)\left(\frac{1}{\theta(l^2-k^2)}-1\right)$. The cutoff function $R_k(L) = (i\omega + l^2)\left(\frac{1}{\theta(l^2-k^2)}-1\right)$ cuts off quantum fluctuations sharply, i.e. it totally suppresses the modes with $l^2 < k^2$ during the renormalization group evolution. This type of cutoff was used in the closely related three-body problem in [52] as will be discussed in Chapter 4. The cutoff satisfies

$$\frac{1}{i\omega + l^2 + R_k(L)} = \theta(l^2-k^2)\frac{1}{i\omega+l^2}. \tag{3.15}$$

Employing this property we can calculate $J_{n,d}$ defined in Eq. (3.14) explicitly as

$$J_{n,d} = \int \frac{d\omega}{2\pi}\frac{d^dl}{(2\pi)^d}\partial_t\theta(l^2-k^2)\frac{F_d^n(l)}{(i\omega+l^2)(-i\omega+l^2)} = -\frac{\pi S_d}{(2\pi)^{d+1}}k^{d-2}F_d^n(k) \tag{3.16}$$

with $S_d = \frac{2\pi^{d/2}}{\Gamma(d/2)}$ being the area of a unit sphere in d-dimensional space. The resulting $J_{n,d}$ can be readily substituted in Eq. (3.13)

$$\partial_t\lambda_\psi = -\frac{k^{d-2}}{(4\pi)^{d/2}\Gamma(d/2)}\lambda_\psi^2 - \frac{2\kappa}{d-2}\lambda_\psi - \frac{(4\pi)^{d/2}\Gamma(d/2)}{(d-2)^2}\kappa^2. \tag{3.17}$$

The contact coupling λ_ψ has a naive (Gaussian) scaling dimension $[\lambda_\psi] = 2-d$ and is IR irrelevant in $d > 2$. Our aim is to investigate the fixed point structure of Eq. (3.17). For this reason we introduce a dimensionless, rescaled coupling $\lambda_{\psi R} \equiv \frac{k^{d-2}\lambda_\psi}{(4\pi)^{d/2}\Gamma(d/2)}$ and its flow equation reads

$$\partial_t\lambda_{\psi R} = -\lambda_{\psi R}^2 + \left(-\frac{2\kappa}{d-2} + d - 2\right)\lambda_{\psi R} - \frac{\kappa^2}{(d-2)^2}. \tag{3.18}$$

As will be shown in Section 3.2, the discriminant D of the quadratic β-function determines the overall behavior of the solution. In our case $D = -4\kappa + (d-2)^2$. The critical κ_{cr} is defined by the condition $D = 0$ yielding

$$\kappa_{cr} = \frac{(d-2)^2}{4}. \tag{3.19}$$

For $\kappa < \kappa_{cr}$ (weak attraction and repulsion) the dimensionless coupling $\lambda_{\psi R}$ has two real fixed points

$$\lambda_{\psi R}^{\pm} = -\frac{\kappa}{d-2} + \frac{d-2}{2} \pm \sqrt{\frac{(d-2)^2}{4} - \kappa} \tag{3.20}$$

and the theory is scale invariant in the IR respectively UV. For $\kappa > \kappa_{cr}$ (strong attraction) the coupling $\lambda_{\psi R}$ ceases to have real fixed points and scale invariance is lost.

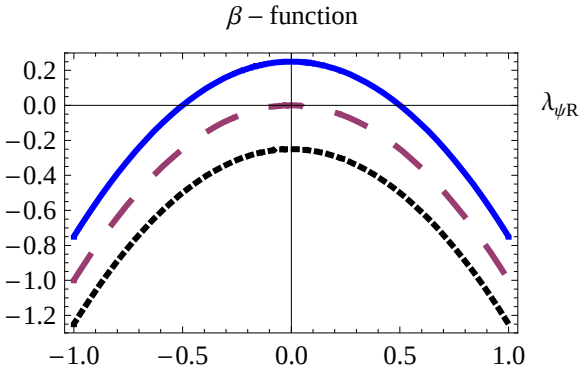

Figure 3.2: The β-function of the coupling $\lambda_{\psi R}$ for $\alpha = -1$ and $\beta = 0$. The three lines correspond to different values of γ with $D = 1$ (solid blue), $D = 0$ (dashed red) and $D = -1$ (dashed black).

3.2 General analysis of the flow equation

The flow equation for $\lambda_{\psi R}$ found in Section 3.1 has the general form

$$\frac{d}{dt}\lambda_{\psi R}(t) = \alpha\lambda_{\psi R}(t)^2 + \beta\lambda_{\psi R}(t) + \gamma, \tag{3.21}$$

where $\alpha, \beta, \gamma \in \mathbb{R}$ are numerical coefficients. Without loss of generality we consider $\alpha \leq 0$. This choice corresponds to the result obtained in Section 3.1. The form of the solution of Eq. (3.21) is determined by the sign of the discriminant $D = \beta^2 - 4\alpha\gamma$ of the quadratic β-function. We consider the three different cases depicted in Figure 3.2

- $D > 0$

  In this case the β-function has two real fixed points $\lambda_{\psi R}^{IR}$ and $\lambda_{\psi R}^{UV}$ with $\lambda_{\psi R}^{IR} < \lambda_{\psi R}^{UV}$. The solution of Eq. (3.21) depends on the interval, where the UV initial condition $\lambda_{\psi R}$ belongs. For the initial condition $\lambda_{\psi R}^{IR} < \lambda_{\psi R} < \lambda_{\psi R}^{UV}$ the solution is attracted towards the IR by the fixed point $\lambda_{\psi R}^{IR}$ and has the form

  $$\lambda_{\psi R}(t) = \frac{-\beta - \sqrt{D}\tanh\left[\frac{\sqrt{D}}{2}(t+\eta)\right]}{2\alpha}, \tag{3.22}$$

  with η fixed by the UV initial condition $\lambda_{\psi R}(t = 0)$. For the initial condition $\lambda_{\psi R} > \lambda_{UV}$ the flow runs into a positive divergence (Landau pole), but reemerges at negative infinity and subsequently approaches

$\lambda_{\psi R}^{IR}$ in the IR. The explicit solution in this case reads

$$\lambda_{\psi R}(t) = \frac{-\beta + \sqrt{D}\coth\left[\frac{\sqrt{D}}{2}(-t+\eta)\right]}{2\alpha}, \tag{3.23}$$

with η fixed by the UV initial condition.[4] Finally, for the initial condition $\lambda_{\psi R} < \lambda_{\psi R}^{IR}$ the RG flow is a smooth, monotonic function $\lambda_{\psi R}(t)$, which approaches $\lambda_{\psi R}^{IR}$ with the explicit solution given again by Eq. (3.23). Notably, for $D > 0$ the IR value $\lambda_{\psi R}(k=0) = \lambda_{\psi R}^{IR}$ is not sensitive to the concrete choice of the initial condition. We offer an elegant geometric description of the flow in Section 3.3 and Section 3.5.

- $D = 0$

  This is a limit of the previous case ($D > 0$) when the two fixed points merge. Excluding the trivial choices $\alpha = \beta = \gamma = 0$ and $\alpha = \beta = 0$; $\gamma \neq 0$, the β-function has a single fixed point $\lambda_{\psi R}^{*} = -\frac{\beta}{2\alpha}$ (see Figure 3.2). The RG equation takes the form

  $$\frac{d\lambda_{\psi R}(t)}{dt} = \alpha[\lambda_{\psi R}(t) - \lambda_{\psi R}^{*}]^2 \tag{3.24}$$

  with the solution

  $$\lambda_{\psi R}(t) = \lambda_{\psi R}^{*} - \frac{1}{\alpha t + \eta}, \tag{3.25}$$

  where η is fixed by the initial condition. The running of the coupling $\lambda_{\psi R}(k)$ is logarithmic (which corresponds to the marginal deformation) and for $\eta < 0$ it hits an IR Landau pole. The coupling runs into the pole at the scale $t = -\frac{\eta}{\alpha}$, nevertheless the RG evolution can be extended beyond this scale and approaches $\lambda_{\psi R}^{*}$ at $k = 0$.

- $D < 0$

  In this case there are no real fixed points. The formal solution can be written as

  $$\lambda_{\psi R}(t) = \frac{-\beta + \sqrt{-D}\tan\left[\frac{\sqrt{-D}}{2}(t+\eta)\right]}{2\alpha}, \tag{3.26}$$

  where η is fixed by the initial condition. This solution is periodic with a period $T = \frac{2\pi}{\sqrt{-D}}$. Remarkably, in this case the UV initial condition $\lambda_{\psi R}(k=\Lambda)$ plays an important role as it determines the infrared value $\lambda_{\psi R}(k=0)$.[5]

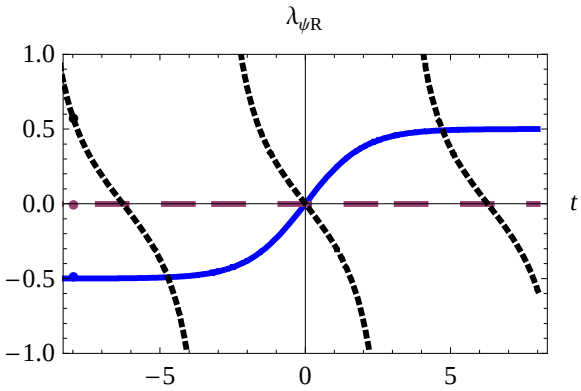

Figure 3.3: The renormalization group flows of the coupling $\lambda_{\psi R}$ for $\alpha = -1$ and $\beta = 0$ and initial condition $\lambda_{\psi R}(t = 0) = 0$. The different lines correspond to three different choices of γ with $D = 1, \eta = 0$ (solid blue), $D = 0, \eta \to \infty$ (dashed red), and $D = -1, \eta = 0$ (dashed black).

We plot the RG flows of $\lambda_{\psi R}$ in the three cases in Figure 3.3. While for $D \geq 0$ the flows approach a fixed point in IR, the renormalization group evolution develops a "limit" cycle[6] for $D < 0$. Quotation marks are used here because in mathematical theory of differential equations a limit cycle is a periodic *stable* solution. The periodic solution (3.26) is not stable, but is only marginal. Thus, the solution should be properly called a cycle. Nevertheless in the physical literature the term limit cycle is often used, so we use this (though probably a little confusing) nomenclature in the thesis. As the RG scale k can be related to the energy of the particles, the physical interpretation of the limit cycle solution is clear: During the RG flow one hits bound states, manifesting themselves as divergences of the coupling $\lambda_{\psi R}$. And since there are infinitely many divergences one has an infinite tower of bound states with a geometric spectrum for the case $D < 0$.

[4]In fact, the case $\kappa = 0$, which leads to $D > 0$, corresponds to the well-studied case of a contact interaction in atomic physics. In this context the appearance of the Landau pole signals the presence of a weakly bound molecular (dimer) state.

[5]This is analogous to the necessity to introduce the well-know three-body parameter in the context of the Efimov effect [1].

[6]Strictly speaking, to find a cycle one needs at least two couplings connected by the RG flow equations (see, for example, Eqs. (3.62, 3.64)). In the case of a single coupling constant an infinite (unbounded) cycle appears only if there are periodic real discontinuities in the RG flow. We provide an elegant description of the infinite cycle on the Riemann sphere in Section 3.3.

3.3 Complex extension

In this Section we discuss the different subcases, considered in Section 3.2, in more detail and extend the analysis to complex values of the interaction coupling. We also present a physical interpretation of this extension.

Negative discriminant: complex fixed points

The renormalization group flow equation in our point-like approximation is[7]

$$\partial_t \lambda = \alpha \lambda^2 + \beta \lambda + \gamma \tag{3.27}$$

with $\alpha, \beta, \gamma \in \mathbb{R}$, and one can vary the parameters β and γ by considering different κ and d in Eq. (3.18). It is sometimes useful to express Eq. (3.27) in the alternative form

$$\partial_t \lambda = \alpha(\lambda - \lambda_*)^2 + \Delta\gamma, \qquad \lambda_* = -\frac{\beta}{2\alpha}, \qquad \Delta\gamma = \gamma - \frac{\beta^2}{4\alpha}. \tag{3.28}$$

If the discriminant $D = \beta^2 - 4\alpha\gamma = -4\alpha\Delta\gamma < 0$, the β-function has a pair of complex roots

$$\lambda^{\pm} = \frac{-\beta \pm i\sqrt{|D|}}{2\alpha} = \lambda_* \pm i\frac{\sqrt{|\alpha\Delta\gamma|}}{\alpha}. \tag{3.29}$$

For this reason it is natural to consider the RG evolution of a generally complex variable $\lambda = \lambda_1 + i\lambda_2$ in Eq. (3.27). The resulting flow equations in the complex plane now read

$$\begin{aligned} \partial_t \lambda_1 &= \alpha\lambda_1^2 - \alpha\lambda_2^2 + \beta\lambda_1 + \gamma \\ \partial_t \lambda_2 &= 2\alpha\lambda_1\lambda_2 + \beta\lambda_2. \end{aligned} \tag{3.30}$$

Notably, if we start on the real axis (i.e. $\lambda_2(t=0) = 0$), the flow remains real

$$\begin{aligned} \partial_t \lambda_1 &= \alpha\lambda_1^2 + \beta\lambda_1 + \gamma \\ \partial_t \lambda_2 &= 0 \end{aligned} \tag{3.31}$$

with the periodic solution

$$\lambda_1(t) = \frac{-\beta + \sqrt{-D}\tan[\frac{\sqrt{-D}}{2}(t+\eta)]}{2\alpha}, \tag{3.32}$$

[7] This equation coincides with Eq. (3.21). To simplify notation, we denote the coupling $\lambda_{\psi R}$ as λ in this Section.

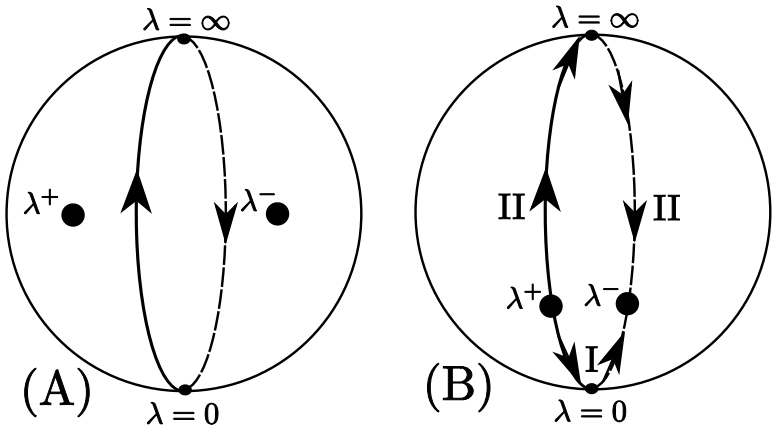

Figure 3.4: The real flows of λ projected onto the Riemann sphere: Great circle with arrows pointing towards the UV represents the real line. (A) For negative discriminant the fixed points λ^+ and λ^- are complex, and the flow traverses the real great circle periodically generating a limit cycle. (B) For positive discriminant the IR fixed point λ^+ and the UV fixed point λ^- lie on the real great circle. The UV fixed point can be reached from the IR fixed point via two different paths– the "short" path I and the "long" path II.

where η is fixed by the initial condition $\lambda_1(t=0)$. The solution can be nicely identified with a limit cycle if we map the complex plane of the Riemann sphere. On the Riemann sphere the real line corresponds to a great circle and the solution (3.32) traverses this circle periodically (see Figure 3.4 (A) and Section 3.5). Remarkably, on the complex plane the real axis is the separatrix of the two complex fixed points.

Let us investigate the properties of the fixed points $\lambda^\pm$ by considering the stability matrices

$$M_{ij}^{\pm} = \frac{\partial \beta_i}{\partial \lambda_j}|_{\lambda^\pm}. \tag{3.33}$$

A straightforward computation shows

$$M^{\pm} = \begin{pmatrix} 0 & -b^{\pm} \\ b^{\pm} & 0 \end{pmatrix}, \qquad b^{\pm} = \pm\sqrt{|D|}. \tag{3.34}$$

The stability matrices $M^\pm$ have a pair of complex conjugate pure imaginary eigenvalues

$$\kappa_1^{\pm} = \pm i\sqrt{|D|} \qquad \kappa_2^{\pm} = (\kappa_1^{\pm})^*. \tag{3.35}$$

Therefore, the local flow near the fixed points has a form of a circle. The sign of $b^\pm$ in the matrix (3.34) determines the orientation of the circle. For

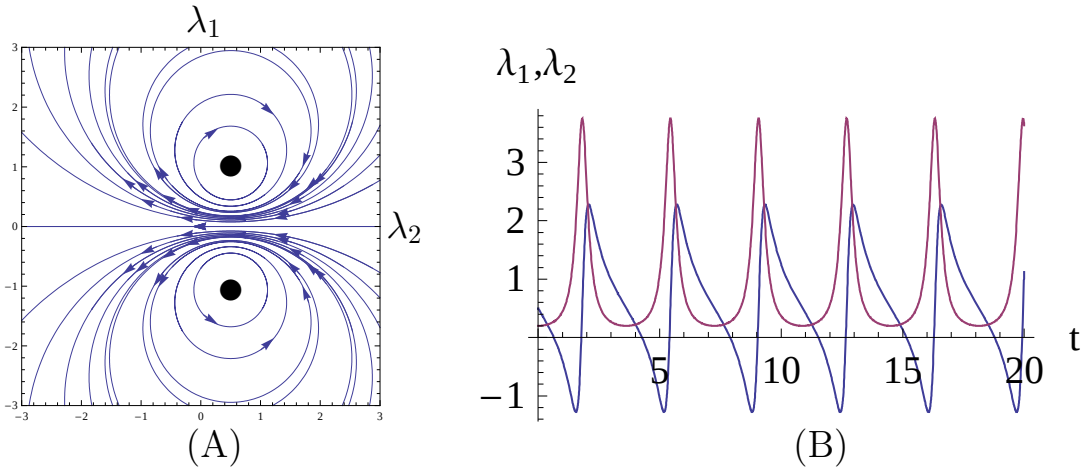

Figure 3.5: (A) The phase portrait of the flow equations (3.30) for the specific choice of parameters $\alpha = \gamma = -1$ and $\beta = 1$. Arrows denote the direction towards the UV. (B) Corresponding periodic flows of the real part λ_1 (blue) and the imaginary part λ_2 (red) of the complex coupling λ.

$b^{\pm} > 0$ the circulation is anticlockwise, while for $b^{\pm} < 0$ it is clockwise. Hence the fixed points $\lambda^{\pm}$ have the opposite circulation.

The phase portrait of the RG flow in the complex plane, computed numerically for specific values of parameters, and the example of the RG flow are depicted in Figure 3.5. We observe that the periodic divergences of the pure real solution (3.32) are regularized and the flow of the imaginary part λ_2 develops a tower of resonances. The analytic solution of Eq. (3.30) for $D < 0$ is given in Section 3.4.

Positive discriminant: real fixed points

If the discriminant D is positive, the β-function has a pair of real roots

$$\lambda^{\pm} = \frac{-\beta \pm \sqrt{D}}{2\alpha}. \tag{3.36}$$

As before, we generalize the coupling to complex values $\lambda = \lambda_1 + i\lambda_2$ and obtain the pair of coupled differential equations (3.30). The phase portrait and a specific solution of the flow equations (3.30) for $D > 0$ are depicted in Figure 3.6. We find the analytic solution of Eq. (3.30) for $D > 0$ in Section 3.4.

The character of the fixed points $\lambda_{\pm}$ can be determined from the stability

matrices $M_{ij}^{\pm}$, defined by Eq. (3.33). For $D > 0$, we obtain

$$M^{\pm} = \begin{pmatrix} \pm\sqrt{D} & 0 \\ 0 & \pm\sqrt{D} \end{pmatrix} = \pm\sqrt{D}I \tag{3.37}$$

with the degenerate eigenvalues $\kappa^{\pm}$

$$\kappa^{\pm} \equiv \kappa_1^{\pm} = \kappa_2^{\pm} = \pm\sqrt{D}. \tag{3.38}$$

The sign of the real eigenvalue determines whether the fixed point is UV attractive or repulsive. The eigenvalue κ^+ is positive and hence the fixed point λ^+ (left fixed point in Figure 3.6(A)) is UV repulsive, meaning that as the sliding scale k is increased the flow is driven away from λ^+. On the other hand κ^- is negative and therefore the fixed point λ^- (right fixed point in Figure 3.6(A)) is UV attractive. Notice that any two-component vector is an eigenvector of the fixed points $\lambda^{\pm}$.

We propose a geometric interpretation for the different behavior of the real solution in dependence on the initial conditions, which we observed in Section 3.2. For a positive discriminant D both the UV fixed point λ^- and the IR fixed point λ^+ are situated on the large real circle on the Riemann sphere (see Figure 3.4 (B) and Section 3.5). We note that the UV fixed point can be reached from the IR fixed point following two different paths. Depending on the initial conditions $\lambda_{\text{in}} = \lambda^+ \pm \epsilon$, the flow can follow either a "short" path I or a "long" path II (see Figure 3.4 (B)). Path I corresponds to the solution (3.22), which is a standard way how to regularize the inverse square potential at $\kappa < \kappa_{cr}$. On the other hand, the path II traverses $\lambda = \infty$ on the Riemann sphere and corresponds to the solution (3.23) with the Landau pole. The divergence during the RG evolution is identified with a single bound state, which, in the case of $\kappa = 0$, becomes the the well-known universal shallow dimer studied extensively in atomic physics [1]. We notice that on the full Riemann sphere the path II can be continuously deformed into the path I. Thus, the introduction of a small imaginary initial condition $\lambda_2(t = 0)$ for the complex extended flow, which leads to a small deformation of the path II, regularizes the divergence in the real part of the coupling (see Figure 3.6 and Section 3.5).

Zero discriminant: degenerate fixed points

Finally, for $D = 0$, the pair of roots of the β-function becomes degenerate

$$\lambda_* \equiv \lambda^+ = \lambda^- = -\frac{\beta}{2\alpha} \tag{3.39}$$

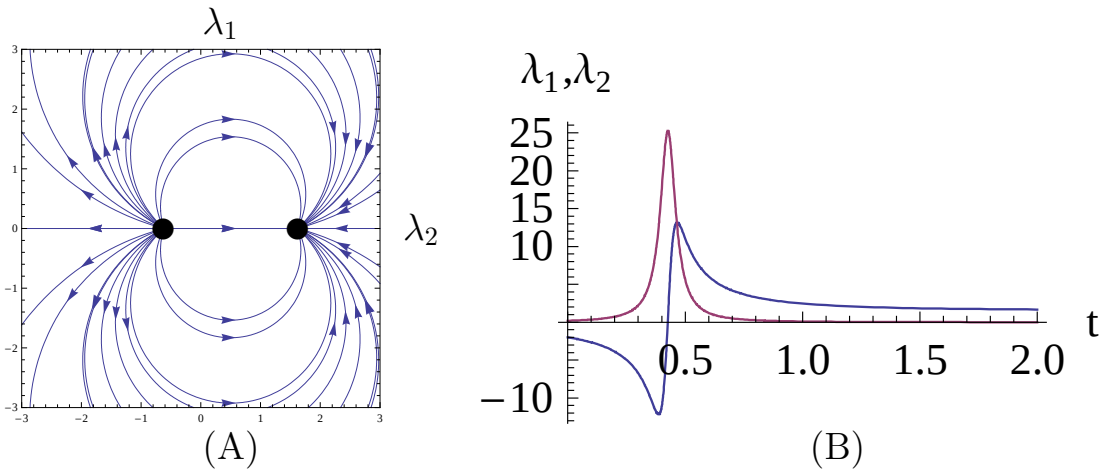

Figure 3.6: (A) The phase portrait of the flow equations (3.30) for the specific choice of parameters $\alpha = -1$ and $\beta = \gamma = 1$. Arrows denote the direction towards the UV. (B) Corresponding renormalization group flows of the real part λ_1 (blue) and the imaginary part λ_2 (red) of the complex coupling λ.

which corresponds to a single, real-valued fixed point λ_*.

As it turns out, the stability matrix $M_{ij} = \frac{\partial \beta_i}{\partial \lambda_j}|_{\lambda_*}$ vanishes in the case of $D = 0$. This corresponds to a logarithmic (marginal) renormalization group flow in the vicinity of the fixed point and local properties of the degenerate fixed point λ_* are accounted for by the second derivative of the β-function K_{ijl} at λ_*

$$K_{ijl} = \frac{\partial^2 \beta_i}{\partial \lambda_j \partial \lambda_l}|_{\lambda^*} \qquad i, j, l = 1, 2. \tag{3.40}$$

The only nontrivial components are

$$K_{111} = -K_{122} = K_{212} = K_{221} = 2\alpha. \tag{3.41}$$

Again, we computed the phase portrait and a specific solution of the flow equations (3.30) and show the results in Figure 3.7. We observe that the Landau pole of the real part of λ is regularized and the imaginary part of λ develops a single resonance.

Physical interpretation of the complex extension

One may wonder about the physical meaning of the complex contact coupling λ introduced in this Section. To answer this question, we consider inelastic

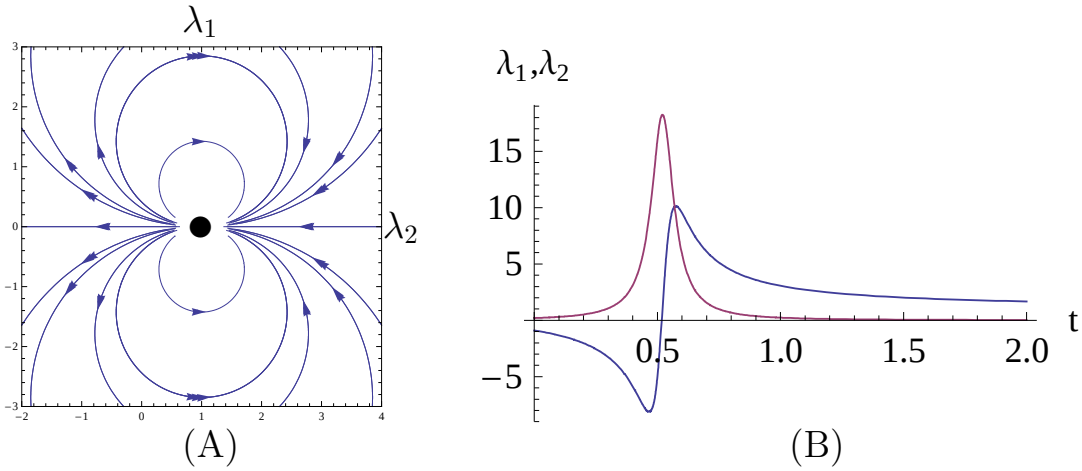

Figure 3.7: (A) The phase portrait of the flow equations (3.30) for the specific choice of parameters $\alpha = -1$, $\beta = 2$ and $\gamma = -1$. Arrows denote the direction towards the UV. (B) Corresponding renormalization group flows of the real part λ_1 (blue) and the imaginary part λ_2 (red) of the complex coupling λ.

scattering[8] of particles in a central potential in quantum mechanics. Following [28] in three spatial dimensions the scattering amplitude in the center of mass frame can be expanded in partial waves

$$f_k(\theta) = \sum_{l=0}^{l=\infty} (2l+1) f_l(k) P_l(\cos(\theta)), \tag{3.42}$$

where $P_l(\cos\theta)$ are the Legendre polynomials. From the unitarity constraints the partial waves scattering amplitudes $f_l(k)$ as functions of scattering momentum k are given by

$$f_l(k) = \frac{1}{g_l(k^2) - ik}. \tag{3.43}$$

Here, $g_l(k^2)$ is an even function of k which is generally complex in the case of presence of inelastic channels.

For low-energy scattering of particles, interacting through a short-range potential, only the s-wave contribution $f = f_0$ is substantial and $g(k^2) =$

[8]By definition inelastic collisions change the internal state of the colliding particles and, hence, at least one of the colliding particles must be composite and have some internal structure. For example, in experiments two atoms might collide and fall into energetically deeper lying internal states. The excess in energy will be converted into kinetic energy and the atoms will be lost if the released energy suffices to overcome the trapping potential.

$g_0(k^2)$ can be expanded as

$$g(k^2) = -a^{-1} + \frac{1}{2} r_{\text{eff}} k^2 + \dots, \tag{3.44}$$

where in the case of elastic scattering a and r_{eff} are real and denote the scattering length and effective range. However, in the inelastic case a may also be regarded as a complex scattering length $a = \alpha + i\beta$ and the effective range r_{eff} might also be complex [53]. In the forthcoming argument it is sufficient to consider low energy scattering and therefore we keep only the scattering length a and neglect the second term in Eq. (3.44).

The generalized optical theorem for the scattering of indistinguishable particles

$$\text{Im} f(k) = \frac{k}{8\pi} \sigma_{tot} = \frac{k}{8\pi} (\sigma_{el} + \sigma_{in}) \tag{3.45}$$

holds also in the case of general inelastic scattering [28]. In this case the total scattering cross section σ_{tot} is the sum of the positive elastic σ_{el} and inelastic σ_{in} contributions. The positivity of σ_{in} and the optical theorem (3.45) imply that the imaginary part of the scattering length β must be negative. At low energies and for sufficiently short-range interactions the complex scattering length fully determines the elastic and inelastic cross sections, and for indistinguishable particles the result reads [28]

$$\begin{aligned} \sigma_{el} &= 8\pi |a|^2 (1 - 2k|\beta|) \\ \sigma_{in} &= 8\pi \frac{|\beta|}{k} (1 - 2k|\beta|). \end{aligned} \tag{3.46}$$

We observe that a nonvanishing imaginary part of the scattering length β is required to obtain an inelastic contribution to the total cross section,[9] which results in loss of particles.

The presented arguments can be connected to a complex generalization of λ by the simple observation that in a system of identical bosons with short-range interactions the physical scattering length a is related to the IR value of the dimensionful, contact coupling λ_ψ in $d = 3$ via the simple formula (in the case of $\kappa = 0$)

$$\lambda_\psi(k = 0) = -8\pi a. \tag{3.47}$$

Thus, allowing for complex values of λ_ψ during the RG flow corresponds to the presence of inelastic two-body collisions leading to particle loss. This provides a physical interpretation of the complex coupling λ_ψ. We must stress,

[9] We note that according to [28] Eq. (3.46) is valid for sufficiently fast decrease of the interaction potential at large distances (at least $1/r^3$). Thus, it is not strictly applicable in our case of the long-range $1/r^2$ potential, and the presented argument has to be taken as heuristic.

however, that the local $(\psi^\dagger\psi)^2$ operator with a negative imaginary coefficient can describe inelastic scattering only to deep energetic states, i.e. the gap energy E_{gap} of the state must be large compared to other energy scales in the problem [54]. On the other hand, decay into shallow bound states can be described by introduction of a nonlocal operator with a complex coefficient. In fact, a large imaginary part of the two-body interaction might also be useful in the context of atomic physics. This case has recently been studied for cold atoms confined to motion in 1D. In particular it has been shown that a Tonks-Girardeau gas, where 1D strongly repulsive bosons exhibit fermionic like behavior, can also be induced by the effect of strong dissipation [55, 56], meaning large imaginary two-body interaction $\lambda_{\psi 2}$.

Finally, we note that our extension of the RG equation to the complex plane can be used as an efficient numerical tool. As was demonstrated in Section 3.2, the flow equation (3.21) has the periodic solution (3.26) in the nonconformal phase. The running coupling $\lambda_{\psi R}$ diverges periodically during the RG evolution, making the numerical solution impossible beyond the first divergence. We showed in this Section that adding a small imaginary part to the initial condition $\lambda_{\psi R}(t = 0)$ makes the solution of Eq. (3.21) numerically feasible. Physically, this corresponds to converting stable bound states to long-lived resonances. As shown in the next Section, the problem considered in here can be treated analytically and hence the numerical treatment is not necessary. Nevertheless, the extension turns out to be useful in some other few-body problems, which can not be solved analytically.

3.4 Bosonization

In this Section we approximate the four-particle vertex by an exchange of a composite particle. Introduced already in Chapter 2, the bosonization procedure is a powerful, physically transparent concept. Here we will bosonize in two distinct ways. The first bosonization corresponds to the exchange of a massless nondynamical particle in the t-channel. In this realization the composite particle mediates the long-range $1/r^2$ interaction combined with the contact four-particle interaction. Alternatively, one can approximate the contact vertex by the exchange of a massive particle in the s-channel. While at low energies and momenta bosonization simply reproduces the pointlike (momentum-independent) approximation of Section 3.1, it resolves some of momentum structure of the interaction at higher energies.

t-channel bosonization

In this subsection we approximate the total four-particle interaction vertex by the exchange of a composite massless particle χ in the t-channel.

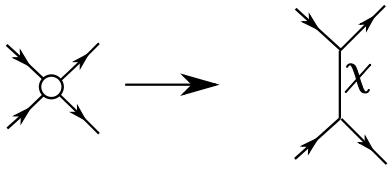

Galilean symmetry of the nonrelativistic vacuum implies that the inverse propagator $P_\chi(\omega, \vec{q})$ of the massless particle depends only on the absolute value of the spatial momentum $\vec{q}$, but not on the frequency ω. Thus, the composite χ is not a dynamical particle and serves only to mediate the two-body long-range interaction.

Mathematically, bosonization is implemented by means of the Hubbard-Stratonovich transformation. At $T = \mu = 0$ one adds an auxiliary part to the microscopic action (3.7)

$$\begin{aligned} S_{E,aux}[\psi, \psi^*, \chi] = \frac{1}{2} \int_{Q_1,Q_2,\ldots,Q_4} & P_\chi(l)\{\chi(-L) + \frac{g}{2P_\chi(\vec{l})}\psi^*(Q_1)\psi(Q_2)\}\times \\ & \{\chi(L) + \frac{g}{2P_\chi(\vec{l})}\psi^*(Q_3)\psi(Q_4)\}\times \\ & \delta(-Q_1 + Q_2 - Q_3 + Q_4), \end{aligned} \tag{3.48}$$

where $L = (\omega_l, \vec{l}) = Q_2 - Q_1 = Q_3 - Q_4$ is the momentum transfer $d+1$-vector and χ is a real-valued field. The modified action $S_E^{'} = S_E + S_{E,aux}$ defines an equivalent quantum mechanical problem as the action S_E because the functional integral in the field χ is Gaussian.

Notably, at the UV scale we can achieve the cancellation of the four-particle interaction term by choosing the nonlocal inverse propagator

$$P_\chi(l) = \frac{g^2}{4}\left[\lambda_\psi^{UV} + 2\kappa F_d(l)\right]^{-1}, \tag{3.49}$$

where λ_ψ^{UV} is the microscopic (bare) contact coupling in Eq. (3.7). The modified bare action $S_E^{'}$ now reads

$$\begin{aligned} S_E^{'}[\psi, \psi^*, \chi] = & \int_Q \psi^*(Q)[i\omega + \vec{q}^2]\psi(Q) + \frac{1}{2}\int_Q \chi(-Q)P_\chi(q)\chi(Q) \\ & + g\int_{Q_1,Q_2,Q_3} \psi^*(Q_1)\psi(Q_2)\chi(Q_3)\delta(-Q_1 + Q_2 + Q_3) \end{aligned} \tag{3.50}$$

with the four-boson interaction replaced by the Yukawa-like term $\chi\psi\psi^*$. Our truncation for the flowing action is chosen to be

$$\begin{aligned}\Gamma_k[\psi,\psi^*,\chi] &= \int_Q \psi^*(Q)P_\psi(Q)\psi(Q) + \frac{1}{2}\int_Q \chi(-Q)P_\chi(Q)\chi(Q) \\ &+ g\int_{Q_1,Q_2,Q_3} \psi^*(Q_1)\psi(Q_2)\chi(Q_3)\delta(-Q_1+Q_2+Q_3) \\ &- \frac{\lambda}{2}\int_{Q_1,Q_2,\ldots,Q_4} \psi^*(Q_1)\psi(Q_2)\psi^*(Q_3)\psi(Q_4)\delta(-Q_1+Q_2-Q_3+Q_4),\end{aligned} \tag{3.51}$$

where λ is a contact coupling, which is zero in the ultraviolet by construction and is regenerated during the RG flow through a box diagram.

Due to the numerous simplifications of the nonrelativistic vacuum, which are described in detail in Chapter 4 and [52], we note:

- the inverse propagators P_ψ and P_χ are not renormalized during the RG flow

$$P_\psi(Q) = i\omega + \vec{q}, \qquad P_\chi(Q) = \frac{g^2}{4}\left[\lambda_\psi^{UV} + 2\kappa F_d(l)\right]^{-1}. \tag{3.52}$$

  Technically this arises from the fact that the one-loop Feynman diagrams, which would renormalize P_ψ and P_ϕ, have poles in the same half plane of the complex loop frequency. One can close the integration contour such that it does not enclose any frequency poles. As the result of the residue theorem, the frequency integrals vanish, leading to the nonrenormalization of the propagators. We observe the clear manifestation of the nonrenormalization of the long-range potential, mentioned already in Section 3.1. Another example for this behavior is the boundary sine-Gordon theory, which was studied in [57, 58].

- The coupling g can be chosen arbitrarily, e.g. $g = 1$, at the UV scale. This is a well-know ambiguity of the Hubbard-Stratonovich decoupling. Furthermore, the coupling g is also not renormalized during the renormalization group evolution for the reason mentioned in the previous point.

- Interaction terms of the form χ^n with $n \geq 1$ and $\psi^*\psi\chi^k$ with $k > 1$ are absent in the ultraviolet and are not generated during the flow due to the argument provided above. On the other hand interaction terms of the form $(\psi^*\psi)^2\chi^k$ with $k \geq 0$ are generated through box diagrams during the renormalization group evolution.

- Our truncation is complete up to the two-body sector. This is a result of the special hierarchy of the flow equations in the nonrelativistic vacuum which will be discussed in more detail in Chapter 4.

It is straightforward to derive the flow equation of the momentum-independent coupling λ. The result turns out to be given by Eqs. (3.13, 3.14) with the substitution $F_d^n(l) \to F_d^n(l) + \frac{\lambda_\psi^{UV}}{2\kappa}$ in Eq. (3.14). The initial condition $\lambda_\psi(k = \Lambda) = \lambda_\psi^{UV}$ of the one-channel model of Section 3.1 is implemented directly as the initial condition of the inverse propagator P_χ in the bosonization approach. Otherwise, the flows are completely equivalent at the level of our approximation.

s-channel bosonization

We will follow an alternative bosonization procedure in this subsection. In this approach the four-particle contact vertex is approximated by the exchange of a massive ($M_\phi = 2M_\psi$) particle ϕ in the s-channel.

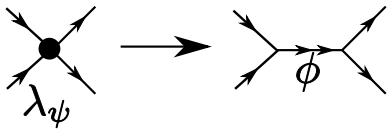

At the level of the microscopic (bare) action this is achieved via the Hubbard-Stratonovich transformation. The auxiliary part, added to the microscopic action (3.7) at $T = \mu = 0$, reads

$$\begin{aligned} S_{E,aux}[\psi,\psi^*,\phi,\phi^*] = \int_{Q_1,Q_2,\ldots,Q_4} & m^2\{\phi^*(Q_1+Q_3) + \frac{h}{2m^2}\psi^*(Q_1)\psi^*(Q_3)\}\times \\ & \{\phi(Q_2+Q_4) + \frac{h}{2m^2}\psi(Q_2)\psi(Q_4)\}\times \\ & \delta(-Q_1+Q_2-Q_3+Q_4). \end{aligned} \tag{3.53}$$

For the specific choice $\frac{\lambda_\psi}{2} = \frac{h^2}{4m^2}$, we can cancel the contact term in the modified microscopic action $S_E^{'} = S_E + S_{E,aux}$

$$\begin{aligned} S_E^{'}[\psi,\psi^*,\phi,\phi^*] &= \int_Q \psi^*(Q)[i\omega + \vec{q}^2]\psi(Q) + \int_Q \phi^*(Q)m^2\phi(Q) \\ &+ \frac{h}{2}\int_{Q_1,Q_2,Q_3} [\phi^*(Q_1)\psi(Q_2)\psi(Q_3) + \phi(Q_1)\psi^*(Q_2)\psi^*(Q_3)]\,\delta(-Q_1+Q_2+Q_3) \\ &- \kappa\int_{Q_1,Q_2,\ldots,Q_4} F_d(l)\psi^*(Q_1)\psi(Q_2)\psi^*(Q_3)\psi(Q_4)\delta(-Q_1+Q_2-Q_3+Q_4). \end{aligned} \tag{3.54}$$

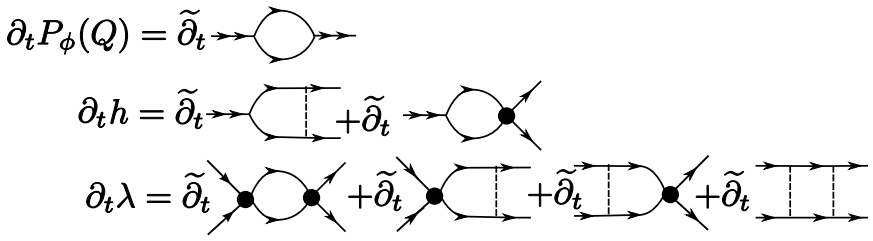

Figure 3.8: Flow equations of $P_\phi(Q)$, h and λ in the form of Feynman diagrams. The solid lines with one (two) arrow(s) denote regularized propagator for the field ψ (ϕ), the dashed lines correspond to the long-range interaction vertex, the dark blob represents the contact coupling λ.

During the renormalization group evolution the massive field ϕ becomes dynamical and develops an inverse propagator $P_\phi(Q) = f(i\omega + \frac{q^2}{2} + m^2)$, where f is some yet unknown function. The argument of the inverse propagator is fixed by the Galilean symmetry of the nonrelativistic vacuum, while the function f is determined by the dynamics. Our truncation of the flowing action within the s-channel bosonization approach is

$$\begin{aligned}\Gamma_k[\psi,\psi^*,\phi,\phi^*] &= \int_Q \psi^*(Q)P_\psi(Q)\psi(Q) + \int_Q \phi^*(Q)P_\phi(Q)\phi(Q) \\ &+ \frac{h}{2}\int_{Q_1,Q_2,Q_3} \left(\phi^*(Q_1)\psi(Q_2)\psi(Q_3) + \phi(Q_1)\psi^*(Q_2)\psi^*(Q_3)\right)\delta(-Q_1+Q_2+Q_3) \\ &- \kappa\int_{Q_1,Q_2,\ldots,Q_4} F_d(l)\psi^*(Q_1)\psi(Q_2)\psi^*(Q_3)\psi(Q_4)\delta(-Q_1+Q_2-Q_3+Q_4) \\ &- \frac{\lambda}{2}\int_{Q_1,Q_2,\ldots,Q_4} \psi^*(Q_1)\psi(Q_2)\psi^*(Q_3)\psi(Q_4)\delta(-Q_1+Q_2-Q_3+Q_4),\end{aligned} \tag{3.55}$$

where h denotes the momentum-independent Yukawa-like coupling introduced above and λ stands for the contact four-boson 1PI vertex, which is regenerated during the flow through the box diagram. The nontrivial flow equations for the couplings of the average action (3.55) are depicted in Figure 3.8 in terms of Feynman diagrams.

It is desirable and possible to cancel the RG flow of the coupling λ by absorbing it into the flows of the other couplings. This can be achieved by a rebosonization procedure [23, 18, 24]. The idea is to make the composite field scale-dependent $\phi \to \phi_k$ with the choice

$$\partial_k \phi_k = \alpha_k \psi\psi \qquad \partial_k \phi_k^* = \alpha_k \psi^*\psi^*, \tag{3.56}$$

where α_k is some real, scale-dependent function. The one-loop Wetterich flow equation (2.1) for the average action generalizes to[10]

$$\partial_k \Gamma_k = \frac{1}{2}\mathrm{Tr}\,\partial_k R_k \left(\Gamma_k^{(2)} + R_k\right)^{-1} + \int \frac{\delta \Gamma_k}{\delta \phi_k}\partial_k \phi_k + \int \frac{\delta \Gamma_k}{\delta \phi_k^*}\partial_k \phi_k^*. \tag{3.57}$$

The unknown scale-dependent coefficient α_k can now be fixed by the condition that the flow of the contact coupling λ is zero

$$\partial_t \lambda = 0 \Rightarrow \lambda = 0. \tag{3.58}$$

The resulting flow equations (with unspecified cutoff) for the Yukawa coupling h and the inverse propagator $P_\phi(Q)$ now read

$$\begin{aligned} \partial_t P_\phi(Q) &= -\frac{1}{2}h^2 J_{0,d}(Q) \\ \partial_t h &= 2h\kappa J_{1,d} + \frac{4\kappa^2 P_\phi(Q=0) J_{2,d}}{h}, \end{aligned} \tag{3.59}$$

where $J_{n,d}$ was defined in Eq. (3.14), and for $J_{0,d}$ we introduce the momentum-dependent generalization

$$J_{0,d}(Q) = \int \frac{d\omega}{2\pi}\frac{d^d l}{(2\pi)^d}\partial_t \frac{1}{[i(\omega+\omega_q) + (\vec{l}+\vec{q})^2 + R_k(L+Q)][-i\omega + \vec{l}^2 + R_k(-L)]}. \tag{3.60}$$

In order to proceed we must specify the cutoff function and the ansatz for the inverse propagator of the field ϕ. We choose the sharp cutoff, introduced in Section 3.1 and take the simple ansatz $P_\phi(Q) = A_\phi(i\omega + \frac{q^2}{2}) + m^2$. With this choice the flow equations become

$$\begin{aligned} \partial_t m_R^2 &= (2\xi - d - 2)m_R^2 + \frac{1}{2}h_R^2, \\ \partial_t h_R &= (\xi - 2 - \frac{\kappa}{d-2})h_R - \frac{\kappa^2}{(d-2)^2}\frac{m_R^2}{h_R}, \\ \partial_t A_{\phi R} &= (2\xi - d)A_{\phi R} - \frac{1}{4}h_R^2, \end{aligned} \tag{3.61}$$

where we expressed the flows in terms of the rescaled parameters $m_R^2 = k^{-2-d+2\xi}m^2$, $A_{\phi R} = k^{-d+2\xi}A_\phi$, and $h_R = \sqrt{\frac{1}{(4\pi)^{d/2}\Gamma(\frac{d}{2})}}k^{\xi-2}h$. The parameter

[10]Note that in addition to the extra terms, written in Eq. (3.57), a general rebosonization includes terms of the form $\mathrm{Tr}\,(\Gamma_k^{(2)} + R_k)^{-1}\frac{\delta}{\delta\phi_k^*}R_k\partial_k\phi_k + c.c$ [10, 18]. We checked explicitly that these terms do not contribute to the flow equations of the two-body sector.

ξ is not specified yet, but can be identified with the naive scaling dimension of the composite field, i.e. $[\phi] = \xi$. At this point it is convenient to multiply the second equation in (3.61) by $2h_R$ and obtain flow equations for m_R^2 and h_R^2

$$\begin{aligned} \partial_t m_R^2 &= (2\xi - d - 2)m_R^2 + \frac{1}{2}h_R^2, \\ \partial_t h_R^2 &= -\frac{2\kappa^2}{(d-2)^2}m_R^2 + 2(\xi - 2 - \frac{\kappa}{d-2})h_R^2. \end{aligned} \tag{3.62}$$

The equations in (3.62) form a closed linear system of first order ordinary differential equations. The eigenvalues $\lambda_\pm$ of this system can be readily found

$$\lambda_\pm = 2\xi - 3 - \frac{d}{2} - \frac{\kappa}{d-2} \pm \frac{1}{2}\sqrt{(d-2)^2 - 4\kappa}. \tag{3.63}$$

We note that $\kappa_{cr} = \frac{(d-2)^2}{4}$, found in Section 3.1, provides an important boundary value also in the current analysis. While for $\kappa < \kappa_{cr}$ (repulsion and weak attraction) the eigenvalues are purely real, for $\kappa > \kappa_{cr}$ (strong attraction) $\lambda^\pm$ acquires a nontrivial imaginary part.

Let us investigate the latter case in more detail. It is convenient to cancel the real part of $\lambda^\pm$ by choosing $\xi = \frac{1}{2}\left(3 + \frac{d}{2} + \frac{\kappa}{d-2}\right)$. With this choice the eigenvalues $\lambda^\pm$ are imaginary, leading to a pure oscillatory behavior of the flows of m_R^2 and h_R^2. Choosing the initial conditions $m_R^2(t=0) = M$, $h_R^2(t=0) = H$, we obtain

$$\begin{aligned} m_R^2(t) &= M\cos(\frac{\sqrt{-D}}{2}t) + W_M \sin(\frac{\sqrt{-D}}{2}t) \\ h_R^2(t) &= H\cos(\frac{\sqrt{-D}}{2}t) + W_H \sin(\frac{\sqrt{-D}}{2}t), \end{aligned} \tag{3.64}$$

where $D = (d-2)^2 - 4\kappa$ is the discriminant of the quadratic β-function introduced in Section 3.1 and W_M and W_H can be expressed as

$$\begin{aligned} W_M &= \frac{1}{\sqrt{-D}}\left(\left[2 - d + \frac{2\kappa}{d-2}\right]M + H\right) \\ W_H &= -\frac{1}{\sqrt{-D}}\left(\frac{4\kappa^2}{(d-2)^2}M + \left[2 - d + \frac{2\kappa}{d-2}\right]H\right). \end{aligned} \tag{3.65}$$

As expected, we obtain a finite (bounded) limit cycle solution (3.64) for the pair (m_R^2, h_R^2) for strong attraction $\kappa > \kappa_{cr}$. It is clear that the infinite number of the two-body bound states, present in this case, manifest themselves as zeros of the mass coupling $m_R^2(t)$ during the RG flow.

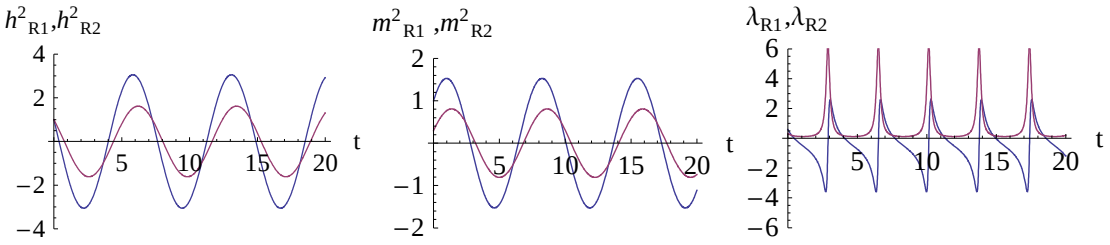

Figure 3.9: Periodic flows of the real part (blue) and imaginary part (red) of the complex couplings h_R^2, m_R^2 and $\lambda_R = \frac{h_R^2}{2m_R^2}$ for the specific choice of parameters $d = 3$ and $\kappa = 1$. The amplitude of the m_{R2}^2 oscillations is related to the decay rate, which must be fixed by experiment. The width of the peaks of λ_{R2} is of the order of magnitude of the decay rate.

It is possible to complexify the flow equations (3.62) in a similar manner as presented in Section 3.3 by extending the couplings h_R^2 and m_R^2 to the complex plane

$$h_R^2 = h_{R1}^2 + ih_{R2}^2 \qquad m_R^2 = m_{R1}^2 + im_{R2}^2. \tag{3.66}$$

In this extension the nonzero value of m_{R2}^2 makes the composite particle ϕ unstable. If small compared to m_{R1}^2, it equals to the decay width, which is inverse proportional to the life-time of the particle. Due to the linearity of the evolution equations (3.62), the flow equations for the pairs (m_{R1}^2, h_{R1}^2), (m_{R2}^2, h_{R2}^2) decouple. They have exactly the same form as Eq. (3.62) with the solution (3.64, 3.65), provided we perform the substitution $m_R^2 \to m_{Ri}^2$, $h_R^2 \to h_{Ri}^2, M \to M_i, H \to H_i$ with $i = 1, 2$. We depict the numerical solution of the complexified system in Figure 3.9. As expected, the flow of the coupling $\lambda_R = \frac{h_R^2}{2m_R^2}$ reproduces our finding from Figure 3.5.

Most importantly, we are now in the position to find an analytical solution of the general nonlinear system of flow equations introduced in Section 3.3

$$\begin{aligned} \partial_t \lambda_{R1} &= \alpha\lambda_{R1}^2 - \alpha\lambda_{R2}^2 + \beta\lambda_{R1} + \gamma \\ \partial_t \lambda_{R2} &= 2\alpha\lambda_{R1}\lambda_{R2} + \beta\lambda_{R2}, \end{aligned} \tag{3.67}$$

with $\alpha, \beta, \gamma \in \mathbb{R}$ and $D = \beta^2 - 4\alpha\gamma < 0$. In order to achieve this goal, it is sufficient to project the complex coupling

$$\lambda_R = \frac{h_R^2}{2m_R^2} = \frac{h_{R1}^2 + ih_{R2}^2}{2[m_{R1}^2 + im_{R2}^2]} \tag{3.68}$$

onto its real and imaginary part λ_{R1} and λ_{R2}

$$\lambda_{R1} = \frac{m_{R1}^2 h_{R1}^2 + m_{R2}^2 h_{R2}^2}{2[m_{R1}^4 + m_{R2}^4]} \qquad \lambda_{R2} = \frac{m_{R1}^2 h_{R2}^2 - m_{R2}^2 h_{R1}^2}{2[m_{R1}^4 + m_{R2}^4]}. \tag{3.69}$$

This expression comprises an explicit solution of the system (3.67) provided we substitute

$$\begin{aligned} m_{Ri}^2 &= M_i \cos(\frac{\sqrt{-D}}{2}t) + W_{Mi} \sin(\frac{\sqrt{-D}}{2}t) \\ h_{Ri}^2 &= H_i \cos(\frac{\sqrt{-D}}{2}t) + W_{Hi} \sin(\frac{\sqrt{-D}}{2}t) \end{aligned} \tag{3.70}$$

with $D = \beta^2 - 4\alpha\gamma$ and

$$\begin{aligned} W_{Mi} &= -\frac{1}{\sqrt{-D}} \left(\beta M_i + \alpha H_i\right) \\ W_{Hi} &= \frac{1}{\sqrt{-D}} \left(4\gamma M_i + \beta H_i\right), \end{aligned} \tag{3.71}$$

where $i = 1, 2$.

We comment on the issue of initial conditions. Obviously, the first-order system (3.67) must be supplemented with two initial conditions $\lambda_{R1}(t = 0)$ and $\lambda_{R2}(t = 0)$. In our description, however, there are four unknown constants M_1, M_2, H_1 and H_2 to be fixed. The identification

$$\lambda_{R1}(t=0) = \frac{1}{2}\frac{M_1 H_1 + M_2 H_2}{M_1^2 + M_2^2} \qquad \lambda_{R2}(t=0) = \frac{1}{2}\frac{M_1 H_2 - M_2 H_1}{M_1^2 + M_2^2} \tag{3.72}$$

fixes only two of them, leaving the remaining two ambiguous. This is the known arbitrariness arising in the Hubbard-Stratonovich transformation. Remarkably, one can fix the remaining two constants almost arbitrarily.[11] An especially convenient choice corresponds to $M_1 = 1$ and $M_2 = 0$. With this choice we have

$$\lambda_{R1}(t=0) = \frac{1}{2}H_1 \qquad \lambda_{R2}(t=0) = \frac{1}{2}H_2. \tag{3.73}$$

We present also the analytic solution of Eq. (3.67) in the conformal phase with $D > 0$. The solution is still given by Eq. (3.69) provided we substitute

$$\begin{aligned} m_{Ri}^2 &= M_i \cosh(\frac{\sqrt{D}}{2}t) + W_{Mi} \sinh(\frac{\sqrt{D}}{2}t) \\ h_{Ri}^2 &= H_i \cosh(\frac{\sqrt{D}}{2}t) + W_{Hi} \sinh(\frac{\sqrt{D}}{2}t) \end{aligned} \tag{3.74}$$

[11] Some discrete values of two constants lead to a degenerate solution and are therefore forbidden.

with

$$\begin{aligned} W_{Mi} &= -\frac{1}{\sqrt{D}}\left(\beta M_i + \alpha H_i\right) \\ W_{Hi} &= \frac{1}{\sqrt{D}}\left(4\gamma M_i + \beta H_i\right). \end{aligned} \tag{3.75}$$

Finally we note that the analytic solution (3.68) can be expressed in the unified, compact form

$$\lambda_R = \frac{1}{2\alpha}\left(-\beta - \sqrt{D}\frac{e^{\frac{\sqrt{D}t}{2}} - Ce^{-\frac{\sqrt{D}t}{2}}}{e^{\frac{\sqrt{D}t}{2}} + Ce^{\frac{-\sqrt{D}t}{2}}}\right) \tag{3.76}$$

for both conformal and nonconformal phase. In the last expression $\sqrt{D} \equiv \sqrt{D + i\epsilon} = i\sqrt{-D}$ for $D < 0$, and the complex constant C determines the initial condition for λ_R. Using Eq. (3.76) we compute the curvature $\widetilde{\kappa}$ and the related radius R of the complex RG trajectories, which are given by

$$\widetilde{\kappa} = \frac{1}{R} = \frac{|\lambda'_{R1}\lambda''_{R2} - \lambda'_{R2}\lambda''_{R1}|}{[\lambda'^2_{R1} + \lambda'^2_{R2}]^{3/2}}. \tag{3.77}$$

Here the primes denote the first and second derivative with respect to t. We observe that the curvature does not depend on the "RG time" t in both the conformal and nonconformal phase. For $D > 0$ the trajectories form arcs of circles of radius $R = |\frac{C}{2\alpha \mathrm{Im} C}|\sqrt{D}$ (see Figure 3.6), while for $D < 0$ the trajectories constitute closed circles of radius $R = |\frac{C}{\alpha(1-|C|^2)}|\sqrt{-D}$ (see Figure 3.5).

3.5 Complex RG flows on the Riemann sphere

As has already been noted in Section 3.3, the generalized RG flow of the complex coupling $\lambda = \lambda_1 + i\lambda_2$ can be most conveniently studied on the Riemann sphere. The Riemann sphere is a unit sphere S^2 in three dimensional real space $\mathbb{R}^3$, which intersects the complex plane $\overline{\mathbb{C}} = \mathbb{C} \cup \{\infty\}$ at the equator. The map σ: $S^2 \to \overline{\mathbb{C}}$ onto the complex plane (λ_1, λ_2) is given by the stereographic projection (see Figure 3.10) and reads in the Cartesian coordinates $(x, y, z) \in S^2$

$$\begin{aligned} \lambda_1 = \frac{x}{1-z}, \quad \lambda_2 = \frac{y}{1-z} \qquad &\text{if} \quad (x, y, z) \neq (0, 0, 1) \\ (\lambda_1, \lambda_2) = \infty \qquad &\text{if} \quad (x, y, z) = (0, 0, 1). \end{aligned} \tag{3.78}$$

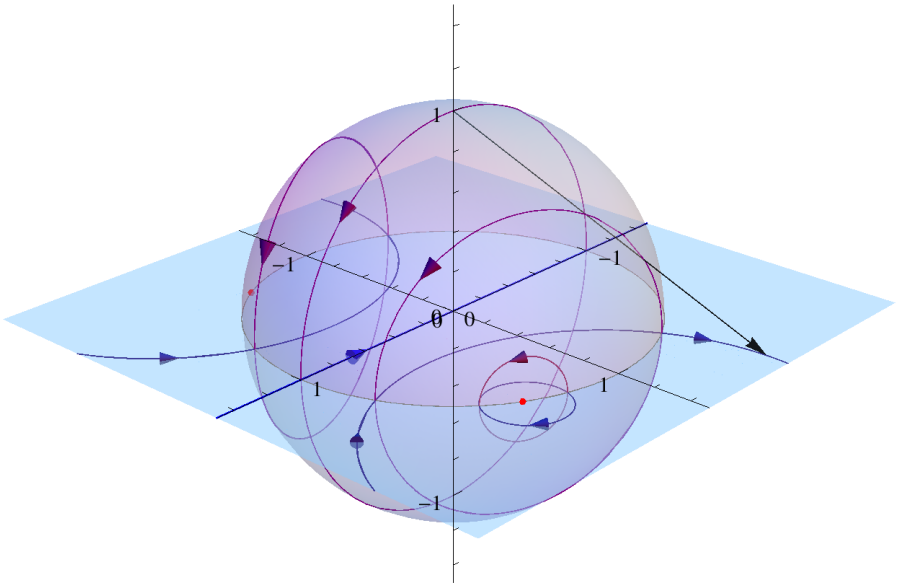

Figure 3.10: RG flows on the complex plane and the corresponding map onto the Riemann sphere in the nonconformal phase. The pink dots represent the two complex fixed points. The solid lines with arrows, pointing towards the UV, correspond to different RG trajectories. Additionally, the black straight solid line from the north pole illustrates the stereographic projection of the Riemann sphere S^2 onto the complex plane $\mathbb{C}$.

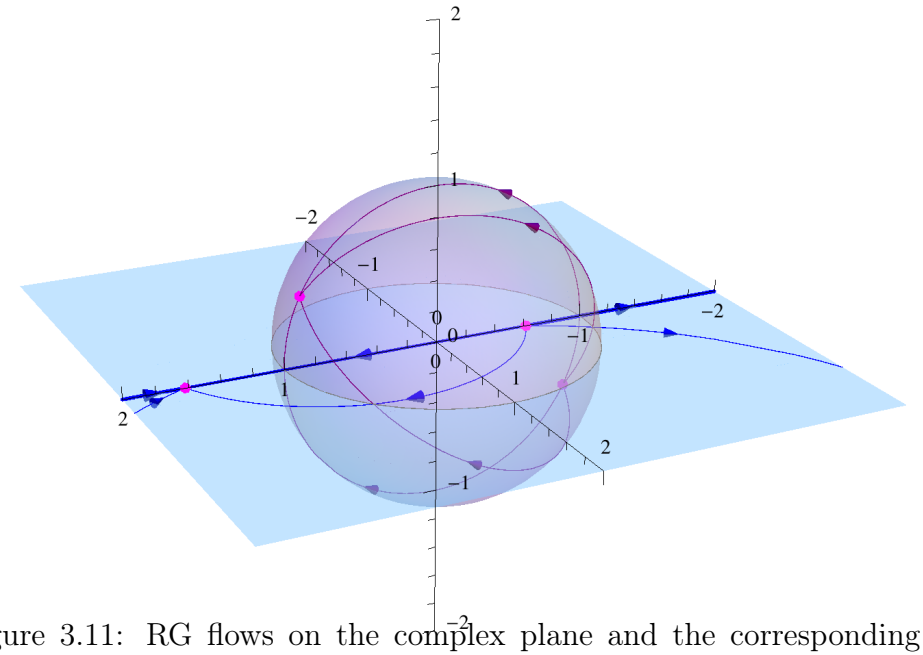

Figure 3.11: RG flows on the complex plane and the corresponding map onto the Riemann sphere in the conformal phase. The pink dots represent the two real fixed points. The solid lines with arrows, pointing towards the UV, correspond to different RG trajectories.

The inverse map is given by

$$x = \frac{2\lambda_1}{\lambda_1^2+\lambda_2^2+1}, \qquad y = \frac{2\lambda_2}{\lambda_1^2+\lambda_2^2+1}, \qquad z = \frac{\lambda_1^2+\lambda_2^2-1}{\lambda_1^2+\lambda_2^2+1}, \qquad \lambda \neq \infty$$
$$x = 0, \qquad y = 0, \qquad z = 1, \qquad \lambda = \infty \tag{3.79}$$

The analytical solution of the complex flow equations (3.30) was obtained in Section 3.4. We substitute these solutions into Eq. (3.79) and obtain the analytical solution on the Riemann sphere, which we plot for both the nonconformal ($D < 0$) and the conformal ($D > 0$) phases in Figures 3.10, and 3.11.

3.6 Summary

In this Chapter we investigated the nonrelativistic, quantum-mechanical problem with an inverse square potential using functional renormalization. The potential is classically scale-invariant. Additionally, it is singular at the origin

and the model must be augmented by a contact term, which is necessary for renormalization. We demonstrated that the RG flow of the contact coupling λ either approaches a real fixed point (conformal phase) in the IR and UV or undergoes a scale anomaly which manifests itself in an infinite, unbounded limit cycle (nonconformal case). The overall behavior is determined by the sign of the discriminant D of the quadratic β-function of the contact coupling, and depends on the strength of the long-range inverse square potential and spatial dimension. Remarkably, in the nonconformal phase ($D < 0$) the β-function possesses a pair of complex conjugate fixed points. This observation led us naturally to the extension of the RG analysis to complex values of the coupling $\lambda \to \lambda_1 + i\lambda_2$. The RG evolution was computed numerically and the phase portraits of the flows were obtained. Additionally, we provided a geometric description of the complex flows on the Riemann sphere. We observed that in the nonconformal phase the real part λ_1 and the imaginary part λ_2 develop a finite (bounded) limit cycle in the complex plane. This suggests that the complex extension can be utilized as an efficient numerical tool for investigation of various problems with infinite (unbounded) limit cycles, as for example, in few-body physics of cold atoms near unitarity. One should simply add a small imaginary part λ_2 to the real part λ_1 and follow the extended RG evolution. This procedure regulates the periodic singularities during the RG flow making the numerical treatment feasible. From a physical point of view, the introduction of the complex coupling constant appears quite natural since it arises from an inelastic channel in the two-body scattering. The bosonization procedure allowed us to view the problem from a different perspective. More importantly, it enabled us to find an analytical solution of the extended set of nonlinear flow equations.

Quite surprisingly, a similar RG behavior as in our case of an inverse square potential appears also in the context of chiral dynamics in QCD with a large number of flavors [59, 60]. Here, gluon exchange between the quarks induces quark self-interactions. The flow equations governing the RG evolution of these self-interactions exhibit the same behavior as shown in Figure 3.2. Depending on the value of the gauge coupling α the flow equations possess either two fixed points ($\alpha < \alpha_{cr}$) and the system is in the chiral symmetric phase, or as α increases above this critical value α_{cr} one ends up in the chiral symmetry broken phase. The analog to the conformal symmetry breaking in dependence on the value of κ in our simple case of an inverse square potential appears to be quite remarkable.

Finally, we comment on a possible connection between our work and the recent studies of nonFermi liquids using the AdS/CFT correspondence [61, 62, 63]. The authors of [62, 63] studied the relativistic many-body physics of fermions at vanishing temperature in d spacetime dimensions by mapping

onto a classical gravity problem with an extremal charged black hole in anti-de Sitter spacetime (AdS_{d+1}). In this description the low-energy scaling behavior around the Fermi surface is related to the near-horizon geometry, which turns out to be $AdS_2 \times \mathbb{R}^{d-1}$. Notably, the isometry group of the AdS_2 part is $SO(2,1)$, which is exactly the symmetry group of the quantum mechanics of the inverse square potential in the conformal phase [44]. This suggests that the emergent IR CFT, defined in [63], might be conformal quantum mechanics with the inverse square potential. Another evidence in this direction is given by the observation that the low-energy behavior of the real and imaginary parts of the retarded Green functions, computed numerically in [62, 63], agrees remarkably well with the RG flows of the real and imaginary part of the contact coupling in conformal and nonconformal phases (see Figures 3.5, 3.6). This suggests that the complex extension and its analytical solution, described in this Chapter, might be useful for a better understanding of nonFermi liquids from the AdS/CFT correspondence.

Chapter 4

Universal Three-body Problem: Efimov Effect

The physics of ultracold atoms is a broad area of research which develops rapidly both experimentally and theoretically (for recent reviews see [64, 65]). To a large extend this is due to the excellent tunability and control of the studied systems. In particular the interaction strength of atoms near a Feshbach resonance can be changed in broad ranges by tuning the magnetic field, which makes these systems an ideal playground for testing the predictions of theoretical models at strong coupling. Both, few-body and many-body quantum, and thermodynamic effects have been extensively studied with ultracold gases.

This made it possible, that, about forty years after the seminal prediction [3] of Vitaly Efimov of the existence of universal three-body bound states in systems with large two-body interactions, first evidence in favor of the presence of these states had been found in the remarkable experiment by Kraemer et al. in 2006 [4]. The findings of Kraemer et al. stimulated extensive activity in the field of three-body physics, both experimentally [66, 89, 90, 67, 68, 69] and theoretically; for recent reviews on also the latter see [1, 100] and references therein. As a result, the Efimov effect in three-body systems is a well-understood phenomenon today.

Near a broad Feshbach resonance the atom-atom s-wave scattering length a is large in comparison to the effective range r_{eff} of the microscopic interaction. The low-energy vacuum physics (for vanishing temperature and density) becomes universal: some physical observables become insensitive to the detailed form of the microscopic interaction and depend only on the scattering length a [1]. For example, for $a > 0$ the theory admits a stable shallow diatom (dimer). For this atom-atom bound state the universal binding energy is determined simply by dimensional analysis. In the unitarity limit all

energy scales drop out of the problem and the theory is scale invariant in the two-body sector. As we mentined in the previous Chapter, the Efimov three-body problem can be mapped onto the quantum-mechanical problem with an inverse square potential.[1] Thus, at unitarity the energy spectrum forms a geometric series which is a signature of the limit cycle behavior of the renormalization group flow. Even in the case of a scale symmetry in the two-body sector, the running of the renormalized three-body couplings indicates a violation of the dilatation symmetry and is associated with a quantum anomaly [44].

The low-energy few-body scattering of atoms has been investigated using various computational nonperturbative techniques ranging from effective field theory [70, 71, 72, 73] to quantum mechanics [3, 74]. The perturbative ϵ expansion around critical $d = 4$ and $d = 2$ dimensions has also been applied to this problem [75, 76]. A field theoretical functional renormalization group approach has been used to investigate the two-body and three-body sectors of two-component fermions recently [77, 78]. As a convenient truncation in vacuum, the authors used a vertex expansion and reproduced the well-known Skorniakov and Ter-Martirosian integral equation [79]. In this way, the universal ratio of the atom-diatom to the atom-atom scattering length $\frac{a_{AD}}{a_{aa}} \approx 1.2$ was computed.

In this Chapter we consider the two- and three-body physics of nonrelativistic atoms near a Feshbach resonance which may be described by a simple two-channel model of particles with short-range interactions. We study three different systems: bosons with a $U(1)$ symmetry (System I), fermions with a $U(1) \times SU(2)$ symmetry (System II) and fermions with a $U(1) \times SU(3)$ symmetry (System III). Both, Systems I and II have been well-studied during the last decade. The model of $SU(3)$ fermions might be of relevance for three-component mixtures of ^{6}Li atoms near the broad Feshbach resonances. Many-body properties of this model have been studied, for example, in [80, 82, 81, 83, 84]. Recently, the three-component fermion system has been studied with functional renormalization group methods using an approximation including a trion field [85] (for more details see [86, 87]).

In the present Chapter we summarize our studies, which are based on the vertex expansion, that complement and extend the results of [85]. In Section 4.1 we introduce the three models we are going to discuss. In Section 4.2 we investigate the effective action in the vacuum state, i.e. for vanishing temperature $T = 0$ and density $n = 0$. The following Section 4.3 is devoted to the exact solution of the two-body sector for positive scattering lengths $a > 0$ (diatom phase). In Section 4.4 we turn to the analysis of the three-

[1] For recent pedagogical exposition see [7].

body sector and derive the RG flow equation for the atom-diatom vertex at unitarity. This RG equation is solved analytically employing a simple point-like approximation in Section 4.5. In Sections 4.6 and 4.7 we reproduce the Skorniakov and Ter-Martirosian integral equation and present a numerical solution of the three-body RG flow equation. We summarize our findings concerning the Efimov effect in Section 4.8.

4.1 Vertex expansion and definition of the models

As has already been mentioned in the previous Section, we perform a systematic vertex expansion of Γ_k taking the full momentum dependence of the relevant vertex in the three-body sector into account. The vertex expansion is an expansion in powers of fields; hence schematically

$$\Gamma_k = \sum_{n=2}^{\infty} \Gamma_k(n) = \Gamma_k(2) + \Gamma_k(3) + \Gamma_k(4) + ..., \tag{4.1}$$

where the index in brackets denotes the number of fields n in the monomial term $\Gamma_k(n)$. In the last equation $\Gamma_k(0)$ and $\Gamma_k(1)$ are missing because the nonrelativistic vacuum (Fock) energy is zero and the term linear in fields is absent due to symmetry. It is important to stress that, even if absent in the microscopic action $S = \Gamma_{k=\Lambda}$, the vertices $\Gamma_k(n)$ are generated and become in general nonlocal in position space during the RG flow. Due to translation invariance of few-body problems that we consider here, it is convenient to Fourier transform to momentum space, where the monomials $\Gamma_k(n)$ are functions of $n-1$ kinematically independent momenta and energies. At the infrared scale ($k = 0$) this kinematic dependence of Γ_k directly translates into energy and momentum dependence of scattering and binding properties of the system.

In this Chapter we describe nonrelativistic physics of atoms interacting via a Feshbach resonance, which can be described by a simple two-channel model.[2] In particular, we consider and compare three different systems:

- System I: Single bosonic field near a Feshbach resonance

[2]In fact, near a broad Feshbach resonance a more simple one-channel model with the four-atom interaction term $\lambda_\psi(\psi^*\psi)^2$ can be used. Nevertheless, it is very convenient to introduce the diatom field $\varphi \sim \psi\psi$ by means of the Hubbard-Stratonovich transformation and arrive in this way to the two-channel model.

Our truncation of the scale-dependent flowing action, written in the Fourier space, is

$$\begin{aligned}
\Gamma_k(2) &= \int_Q \psi^*(Q)(i\omega_{\vec{q}} + \vec{q}^2 - \mu_\psi)\psi(Q) + \int_Q \varphi^*(Q)P_\varphi(Q)\varphi(Q), \\
\Gamma_k(3) &= \frac{h}{2}\int_{Q_1,Q_2,Q_3} \Big[\varphi^*(Q_1)\psi(Q_2)\psi(Q_3) + \varphi(Q_1)\psi^*(Q_2)\psi^*(Q_3)\Big], \\
\Gamma_k(4) &= -\int_{Q_1,\dots Q_4} \lambda_3(Q_1,Q_2,Q_3)\varphi(Q_1)\psi(Q_2)\varphi^*(Q_3)\psi^*(Q_4), \qquad (4.2)
\end{aligned}$$

where $Q = (\omega, \vec{q})$ and $\int\limits_Q = \int_{-\infty}^{\infty}\frac{d\omega}{2\pi}\int_{-\infty}^{\infty}\frac{d^3\vec{q}}{(2\pi)^3}$. Here the energy and momentum conservation restrictions are implicitly assumed.[3] The field ψ represents an elementary complex bosonic atom, while $\varphi(Q)$ is a complex bosonic composite diatom (dimer) which mediates the Feshbach interaction. At the initial UV scale we take $\lambda_3 = 0$. The action for φ becomes Gaussian, and one may integrate out φ using its field equation $\varphi \sim \psi\psi$. As will be demonstrated in Section 4.3, the Yukawa coupling h is simply related to the width of the Feshbach resonance. For $k \to 0$ the coupling $\lambda_3(Q_1,Q_2,Q_3)$ becomes the 1PI vertex which can be connected to the atom-diatom scattering amplitude. The system has an obvious $U(1)$ symmetry which reflects the conserved number of atoms.[4]

- System II: Fermionic doublet near a Feshbach resonance

$$\begin{aligned}
\Gamma_k(2) &= \sum_{i=1}^{2}\int_Q \psi_i^*(Q)(i\omega_{\vec{q}} + \vec{q}^2 - \mu_\psi)\psi_i(Q) + \int_Q \varphi^*(Q)P_\varphi(Q)\varphi(Q), \\
\Gamma_k(3) &= -h\int_{Q_1,Q_2,Q_3} \Big[\varphi^*(Q_1)\psi_1(Q_2)\psi_2(Q_3) - \varphi(Q_1)\psi_1^*(Q_2)\psi_2^*(Q_3)\Big], \\
\Gamma_k(4) &= \int_{Q_1,\dots Q_4} \lambda_3(Q_1,Q_2,Q_3)\sum_{i=1}^{2}\varphi(Q_1)\psi_i(Q_2)\varphi^*(Q_3)\psi_i^*(Q_4). \qquad (4.3)
\end{aligned}$$

[3] We adopt this shortcut notation in the rest of the Chapter.

[4] In general, the $U(1)$ symmetry can be spontaneously broken due to many-body effects and our truncation (4.2) would be insufficient. In this thesis, however, we are interested only in the few-body physics (for more details see Section 4.2) and the symmetry-preserving truncation is sufficient. Similar remark applies to the Systems II and III.

Here, the two species of elementary fermionic atoms ψ_1, ψ_2 are described by Grassmann-valued fields, and φ is a composite bosonic diatom. At the UV scale one has $\varphi \sim \psi_1\psi_2$. This fermionic system has an $SU(2) \times U(1)$ internal symmetry with (ψ_1, ψ_2) transforming as a doublet and φ as a singlet of the $SU(2)$ flavor subgroup. Two-species fermion systems near Feshbach resonances were realized experimentally with ^{6}Li and ^{40}Ka atoms [88].

- System III: Fermionic triplet near a Feshbach resonance

$$\begin{aligned}
\Gamma_k(2) &= \int\limits_Q \sum_{i=1}^{3} \psi_i^*(Q)(i\omega_{\vec{q}} + \vec{q}^2 - \mu_\psi)\psi_i(Q) + \int\limits_Q \sum_{i=1}^{3} \varphi_i^*(Q) P_\varphi(Q) \varphi_i(Q), \\
\Gamma_k(3) &= \frac{h}{2} \int\limits_{Q_1,Q_2,Q_3} \sum_{i,j,k=1}^{3} \epsilon_{ijk} \Big[\varphi_i^*(Q_1)\psi_j(Q_2)\psi_k(Q_3) - \varphi_i(Q_1)\psi_j^*(Q_2)\psi_k^*(Q_3) \Big], \\
\Gamma_k(4) &= \int\limits_{Q_1,\dots Q_4} \Big[\lambda_{3a}(Q_1,Q_2,Q_3) \sum_{i=1}^{3} \varphi_i(Q_1)\psi_i(Q_2) \sum_{j=1}^{3} \varphi_j^*(Q_3)\psi_j^*(Q_4) + \\
&+ \lambda_{3b}(Q_1,Q_2,Q_3) \sum_{i=1}^{3} \psi_i(Q_2)\psi_i^*(Q_4) \sum_{j=1}^{3} \varphi_j(Q_1)\varphi_j^*(Q_3) \Big]. \qquad (4.4)
\end{aligned}$$

The three species of the elementary Grassmann-valued fermion field can be assembled into a vector $\psi = (\psi_1, \psi_2, \psi_3)$. Similarly the three composite Feshbach bosonic diatoms form the vector $\varphi = (\varphi_1, \varphi_2, \varphi_3) \sim (\psi_2\psi_3, \psi_3\psi_1, \psi_1\psi_2)$. The action has an $SU(3) \times U(1)$ symmetry with ψ transforming as $\mathbf{3}$, and φ as $\bar{\mathbf{3}}$ for the $SU(3)$ flavor subgroup. Two different couplings λ_{3a} and λ_{3b} are allowed by the $SU(3)$ symmetry. This model might be of relevance for three-component mixtures of ^{6}Li atoms. There are three distinct broad Feshbach resonances for three scattering channels near $B \approx 800\,\mathrm{G}$ for ^{6}Li atoms. As a first approximation we assume that the resonances for all channels are degenerate, which leads to the $SU(3)$ flavor symmetry and to the model (4.4). A stable three-component mixture of ^{6}Li atoms has been recently created [89, 90]. The theoretical investigation of the 3-body losses in [89, 90] has been recently published [91, 92, 93].

To unify our language for the different models considered in this Chapter, we refer to the elementary particles ψ as atoms (and denote corresponding quantities with the subscript ψ), while the composite φ is called diatom or dimer. All considered systems have Galilean spacetime symmetry, which

consequences we discuss in Appendix B. Our units are $\hbar = k_B = 1$. Moreover we choose the energy units such that $2M_\psi = 1$, where M_ψ is the mass of the atom.

Finally let us stress that $\Gamma(2)$ and $\Gamma(3)$ do not have the most general form allowed by symmetries. The most general form of the vertex expansion includes an arbitrary inverse atom propagator $P_\psi(Q)$ and a momentum-dependent Yukawa coupling $h(Q_1, Q_2, Q_3)$. However, due to special properties of the vacuum state (see Section 4.2), $P_\psi(Q)$ and $h(Q_1, Q_2, Q_3)$ are not renormalized and keep their microscopic values $P_\psi(Q) = (i\omega_{\vec{q}} + \vec{q}^2 - \mu_\psi)$ and $h(Q_1, Q_2, Q_3) = h$ during the RG flow. At this point it is also important to note that our vertex expansion is complete to the third order in the fields. At fourth order in the fields there are only two more vertices, which are compatible with the internal symmetries of the considered models[5]

$$\begin{aligned}\Gamma(4)_\psi &= \tfrac{1}{2} \int\limits_{Q_1,\dots Q_4} \lambda_\psi(Q_1, Q_2, Q_3)\psi^\dagger(Q_1)\psi(Q_2)\psi^\dagger(Q_3)\psi(Q_4),\\ \Gamma(4)_\varphi &= \tfrac{1}{2} \int\limits_{Q_1,\dots Q_4} \lambda_\varphi(Q_1, Q_2, Q_3)\varphi^\dagger(Q_1)\varphi(Q_2)\varphi^\dagger(Q_3)\varphi(Q_4). \end{aligned} \tag{4.5}$$

In the two-channel model considered in this work, we choose the initial UV value of the vertex λ_ψ to be zero, $\lambda_\psi = 0$. This means that the interaction between the atoms are described at the microscopic level solely by the exchange of diatom states. With $\lambda_\psi = 0$ at the UV scale this coupling is not regenerated by the flow in vacuum. The one-loop diagrams contributing to the flow have inner lines pointing in the same direction with respect to the loop momentum and therefore vanish in vacuum (see discussion in Section 4.2). The 1PI vertex λ_φ belongs to the four-body sector and it decouples from the flow equations of the two and three-body sectors due to the vacuum hierarchy (for more details see Section 4.2). Thus our truncations (4.2,4.3,4.4) are sufficient to obtain the exact vacuum physics of the three-body sector.

4.2 Vacuum limit

Usually, in quantum field theory studies of nonrelativistic few-body physics the real-time formalism[6] is employed. The advantage of field-theoretical setting, however, is that it allows to treat on the same footing a more complicated case of systems in equilibrium at nonzero temperature ($T \neq 0$)

[5]For simplicity we explicitly write the remaining vertices for System I only. The vertices for the more complicated Systems II and III can be written straightforwardly and general arguments we present here remain valid for both System II and III.

[6]Here we use a standard notation and denote real (imaginary) time by t (τ) which are related by $t = -i\tau$.

and density ($n \neq 0$). For this reason, although in this Chapter we are interested solely in the scattering and bound states of few particles excited above the nonrelativistic (Fock) vacuum, we employ here the imaginary time formalism. This allows us to perform direct comparison with FRG studies of many-body problems. On the other hand, for direct comparison of energy-dependent observables obtained by other methods, our results must by analytically continued to real (kinetic) energies.

The projection of the many-body effective action $\Gamma_{k=0}$ onto the vacuum state was developed in [95, 77] and must be performed with care. Here we shortly summarize the procedure: The vacuum projection of $\Gamma_{k=0}$ is formally performed as follows

$$\Gamma_{vac} = \lim_{k_F \to 0, T \to 0} \Gamma_{k=0}\Big|_{T > T_c(k_F)}, \tag{4.6}$$

where $k_F = (3\pi^2 n)^{1/3}$ is a "Fermi" wave vector (defined for both bosons and fermions) and n is the atom density of the system. Thus we start with the effective action at finite density and temperature. The system is then made dilute by taking the limit $k_F \to 0$. It is crucial, however, to keep the temperature T above its critical value in order to avoid many-body effects (e.g. Bose-Einstein condensation). One may perform the vacuum limit for a fixed dimensionless $\frac{T}{T_c}$ such that the temperature goes to zero because T_c scales $\sim k_F^2$.

Let us now examine the momentum-independent part of the atom inverse propagator $P_{\psi,k=0}(Q=0) = -\mu_\psi$, as well as its diatom counterpart $m_\varphi^2 \equiv P_{\varphi,k=0}(Q=0)$, in some detail.[7] There is no Fermi surface in vacuum, hence $\mu_\psi \leq 0$. The system is above criticality in the vacuum limit, i.e. it is in the symmetric phase; hence $m_\varphi^2 \geq 0$. These two conditions define a quadrant in the $m_\varphi^2 - \mu_\psi$ plane. In this region $P_\psi(Q=0) = -\mu_\psi > 0$ and $P_\varphi(Q=0) = m_\varphi^2 > 0$ and they act as positive gaps for atoms and diatoms respectively. Moreover, due to the nonrelativistic nature of the problem, the zero energy level can be shifted by an arbitrary constant. This is a result of the symmetries of our models. The real-time ($t = -i\tau$) version of the microscopic action $S = \Gamma_\Lambda$ in coordinate space $(t, \vec{x})$ is symmetric with respect to the energy shift symmetry [97]

$$\psi \to e^{iEt}\psi \qquad \varphi \to e^{2iEt}\varphi \qquad \mu \to \mu + E. \tag{4.7}$$

Since no anomaly of this symmetry is expected and our cutoff respects this symmetry (see below), this is a symmetry of the flow equations and the

[7] Flavor indices applicable for Systems II and III are suppressed in this Section.

effective action $\Gamma_{k=0}$. Hence, by the appropriate energy shift, we can make one energy state gapless, i.e. put it on the boundary of the quadrant in $m_\varphi^2 - \mu_\psi$ plane. We end up with three distinct branches [95]

$$\begin{array}{llll} m_\varphi^2 > 0, & \mu_\psi = 0 & \text{atom phase} & (a^{-1} < 0), \\ m_\varphi^2 = 0, & \mu_\psi < 0 & \text{diatom phase} & (a^{-1} > 0), \\ m_\varphi^2 = 0, & \mu_\psi = 0 & \text{resonance} & (a^{-1} = 0). \end{array} \tag{4.8}$$

For all Systems the gapless state is the lowest energy state in every n-body sector. In the atom phase ($a^{-1} < 0$) diatoms φ are gaped and the scattering threshold is determined by the lowest energy of a two-atom state $\psi\psi$. In the diatom phase ($a^{-1} > 0$) the situation is reversed: diatoms φ determine the scattering threshold and ψ has a gap $-\mu_\psi$, which can be interpreted as a half of the binding energy of φ, $\epsilon = 2\mu_\psi$. At resonance ($a^{-1} = 0$) both, φ and ψ, are gapless. In the three-body problem, for Systems I and III, and for small values of $|a|^{-1}$, one finds a whole spectrum of trions, bound states of three atoms, which have lower energy then $\psi\psi\psi$ and $\varphi\psi$ states. This effect has been first predicted and calculated by Efimov in a quantum mechanical computation [3]. In the trion phase both atoms and diatoms show a gap, i.e. the ground state has $\mu_\psi < 0$, $m_\varphi^2 > 0$. However, for an investigation of the excited Efimov states we may as well use the vacuum fixing condition (4.8). At resonance this corresponds to degenerate energy levels of the Efimov states and the atoms/diatoms, which becomes a good approximation for the high Efimov states which are close to the atom/diatom threshold [85].

The vacuum limit, which we described above, leads to numerous mathematical simplifications. For example, all diagrams with loop lines pointing in the same direction *vanish* in the vacuum limit. Two simple examples of this type of diagrams are depicted in Figure 4.1. Physically, this simplification originates from a simple observation that there are only particles, but no holes as excitations of the nonrelativistic vacuum. Mathematically, this can be demonstrated by employing the residue theorem for the frequency loop integration. Indeed, the inverse propagators have non-negative gaps and all considered diagrams have poles in the upper half plane of the complex loop frequency. Thus we can close the contour such that it does not enclose any poles and the frequency integral vanishes. The argument works also for the 1PI vertices provided they have poles in the same half-plane as the propagators. This finding simplifies the RG analysis in vacuum considerably. For example, one can show that in vacuum the atom inverse propagator $P_\psi(Q)$ is not renormalized [96]. The only one-loop diagram, which renormalizes P_ψ, has inner lines pointing in the same direction, and therefore vanishes. We remind that it is sufficient to analyze only one-loop diagrams because the RG flow equation (2.1) has a general one-loop form [9].

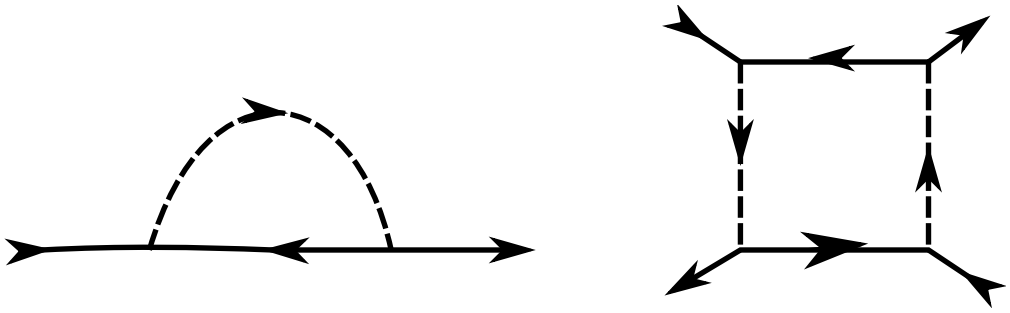

Figure 4.1: Two examples of the Feynman diagrams which vanish in the nonrelativistic vacuum. Solid lines represent atoms ψ, while dashed lines denote diatoms $\varphi \sim \psi\psi$.

Another very important simplification in vacuum comes from a special hierarchy, which is respected by the flow equations. We define the n-body sector as a set of 2n-point 1PI vertices written in terms of elementary atoms.[8] The vacuum hierarchy consists in the fact that the flow of the n-body sector *is not influenced* by any higher-body sectors. The flow equations for the n-body sector simply decouple from the flow of the (n+1)-body sector (and higher). The observed hierarchy is a consequence of the diagrammatic simplification described above (see also [87] for a mathematical proof of the hierarchy). At nonzero density ($n \neq 0$) or temperature ($T \neq 0$) the decoupling of the low-sector vertices from the high-sector vertices is not valid anymore.

4.3 Two-body sector: exact solution

The two-body sector truncation is defined by

$$\Gamma_k = \Gamma_k(2) + \Gamma_k(3) \tag{4.9}$$

in all three models (4.2),(4.3) and (4.4). As discussed in Section 4.2, the RG flows belonging to the two-body sector decouple from higher-body sectors in vacuum. Due to the nonrenormalization of the atom propagator, it is sufficient to solve the flow equations only for the Yukawa coupling h and the diatom inverse propagator P_φ.

It turns out that the Yukawa coupling is not renormalized in vacuum for all three models

$$\partial_t h = 0. \tag{4.10}$$

[8] in this sense $P_\varphi(Q)$ belongs to the two-body sector because $\varphi \sim \psi\psi$ is composed of two atoms

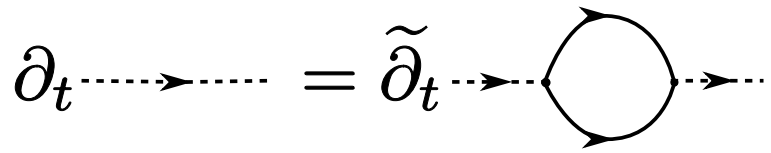

Figure 4.2: Schematic graphical representation of the flow for the inverse diatom propagator P_φ. Diatoms are denoted by dashed lines, atoms by solid lines.

There is no one-loop Feynman diagram in our truncations (4.2,4.3,4.4), which renormalizes the Yukawa coupling h. The only one-loop diagram, which could contribute to the flow of h, contains the four-atom vertex $\lambda_\psi(Q_1, Q_2, Q_3)$. The vertex $\lambda_\psi(Q_1, Q_2, Q_3)$ is not renormalized in vacuum (see our discussion in Section 4.1) and vanishes on all scales, provided its microscopic value is zero. The argument can be extended to a momentum-dependent Yukawa coupling $h(Q_1, Q_2, Q_3)$.

In order to solve the two-body sector, it remains to calculate the flow of the diatom inverse propagator $P_\varphi(Q)$, which is schematically shown in Figure (4.2) and can be written as follows

$$\partial_t P_\varphi(Q) = -\frac{2}{3+p}\int\limits_L \tilde{\partial}_t \frac{h^2}{(P_\psi(L)+R_\psi(L))(P_\psi(Q-L)+R_\psi(Q-L))}, \tag{4.11}$$

where $p = +1$ for bosons and $p = -1$ for fermions. It turns out that the flow of the inverse diatom propagator in System III is exactly the same as in the System II. In the last formula one has

$$P_\psi(Q) = (i\omega_{\vec{q}} + \vec{q}^2 - \mu_\psi) \tag{4.12}$$

and $R_\psi(Q)$ stands for the atom regulator.

It is remarkable that using a special choice of the regulator, we can integrate the flow (4.11) exactly. We follow [77, 94] by choosing a regulator, which is frequency and momentum independent and has the form $R_\psi = k^2 = \Lambda^2 \exp 2t$. This regulator has the advantage that it is Galilean invariant and hence the Galilean symmetry of the microscopic action is preserved during the RG evolution. First, we perform the frequency loop integration in Eq. (4.11) with help of the residue theorem

$$\begin{aligned}\partial_t P_\varphi(Q) &= -\frac{2}{3+p}\int \frac{d^3l}{(2\pi)^3}\tilde{\partial}_t \frac{h^2}{i\omega_{\vec{q}} + \vec{l}^2 + (\vec{l}-\vec{q})^2 - 2\mu_\psi + 2R_\psi} \\ &= -\frac{2h^2}{3+p}\partial_t \int \frac{d^3l}{(2\pi)^3}\frac{1}{i\omega_{\vec{q}} + \vec{l}^2 + (\vec{l}-\vec{q})^2 - 2\mu_\psi + 2R_\psi},\end{aligned} \tag{4.13}$$

where in the second equality we substituted $\tilde{\partial}_t \to \partial_t$ due to the nonrenormalization of the Yukawa coupling h and atom inverse propagator P_ψ. Using the specific values of the regulator $R_\psi(t_{IR}) = 0$ and $R_\psi(t = 0) = \Lambda^2$ we integrate out the flow equation from the UV scale $t = 0$ to the IR scale $t_{IR} = -\infty$ and obtain

$$\begin{aligned} & P_\varphi^{IR}(Q) - P_\varphi^{UV}(Q) = \\ = & -\frac{h^2}{3+p}\int \frac{dl}{2\pi^2}\left(\frac{l^2}{l^2 + \left(\frac{i\omega_{\vec{q}}}{2} + \frac{\vec{q}^2}{4} - \mu_\psi\right)} - \frac{l^2}{l^2 + \left(\frac{i\omega_{\vec{q}}}{2} + \frac{\vec{q}^2}{4} - \mu_\psi + \Lambda^2\right)}\right) \\ = & -\frac{h^2}{4\pi(3+p)}\left(\Lambda - \sqrt{\frac{i\omega_{\vec{q}}}{2} + \frac{\vec{q}^2}{4} - \mu_\psi}\right). \end{aligned} \tag{4.14}$$

In the last identity we assumed $\Lambda >> |\mu_\psi|, |\vec{q}|, |\omega_{\vec{q}}|$.

At this point we must fix the initial condition $P_\varphi^{UV}(Q)$ at $k = \Lambda$ in order to obtain the physical inverse propagator $P_\varphi^{IR}(Q)$ at $k = 0$. This is done in [95, 96, 77] and we follow the same steps here. For broad resonances with $h^2 \to \infty$ the inverse diatom propagator at the microscopic scale Λ is given by

$$P_\varphi^{UV} = \nu(B) + \delta\nu, \qquad \nu(B) = \mu_B(B - B_0). \tag{4.15}$$

Here $\nu(B)$ is the detuning of the magnetic field B which measures the distance to the Feshbach resonance located at B_0. The magnetic moment of the diatom is denoted by μ_B. The counter term $\delta\nu$ depends on the ultraviolet cutoff Λ. Neglecting a possible background scattering length a_{bg}, the scattering length a and the detuning $\nu(B)$ are related by [95]

$$a = -\frac{h^2}{4\pi(3+p)\nu(B)}. \tag{4.16}$$

Thus the Yukawa coupling is proportional to the square root of the width of the Feshbach resonance. For narrow Feshbach resonances ($h \to 0$) perturbation theory is applicable, while for broad Feshbach resonances ($h \to \infty$), which are of main interest here work, the problem becomes strongly coupled. Using Eq. (4.15) and (4.16), we rewrite Eq. (4.14) as

$$P_\varphi^{IR}(Q) - \delta\nu + \frac{h^2}{4\pi(3+p)a} = -\frac{h^2}{4\pi(3+p)}\left(\Lambda - \sqrt{\frac{i\omega_{\vec{q}}}{2} + \frac{\vec{q}^2}{4} - \mu_\psi}\right). \tag{4.17}$$

At this point the momentum independent counter term $\delta\nu$ can be identified

$$\delta\nu = \frac{h^2}{4\pi(3+p)}\Lambda \tag{4.18}$$

and we obtain our final result for the k-dependent inverse diatom propagator $P_{\varphi,k}(Q)$

$$P_{\varphi,k}(Q) = \frac{h^2}{4\pi(3+p)}\Big(- a^{-1} + \sqrt{\frac{i\omega_{\vec{q}}}{2} + \frac{\vec{q}^2}{4} - \mu_\psi + k^2}\Big). \tag{4.19}$$

The wave-function renormalization $Z_{\varphi,k}$ can now be defined

$$Z_{\varphi,k} \equiv \frac{\partial P_{\varphi,k}(Q)}{\partial(i\omega_{\vec{q}})}\Big|_{\omega_{\vec{q}}=0} = \underbrace{\frac{h^2}{4\pi(3+p)}}_{\tilde{Z}} \frac{1}{4\sqrt{k^2-\mu_\psi}}, \tag{4.20}$$

and the IR inverse diatom propagator $P_\varphi(Q)$ reads

$$P_\varphi(Q) \equiv P_{\varphi,k=0}(Q) = \frac{h^2}{4\pi(3+p)}\Big(- a^{-1} + \sqrt{\frac{i\omega_{\vec{q}}}{2} + \frac{\vec{q}^2}{4} - \mu_\psi}\Big). \tag{4.21}$$

In vacuum and for positive scattering length ($a > 0$) the vacuum condition, (4.8), $P_\varphi(Q=0) = m_\varphi^2 = 0$, must be fulfilled. This leads to

$$a = \frac{1}{\sqrt{-\mu_\psi}}. \tag{4.22}$$

For positive scattering lengths in vacuum $P_\psi(Q=0) = -\mu_\psi$ is positive and is interpreted as half of the binding energy of the diatom ϵ_φ. Hence, the binding energy can be expressed as

$$\epsilon_\varphi = 2\mu_\psi = -\frac{2}{a^2}, \qquad \epsilon_\varphi = -\frac{\hbar}{Ma^2}. \tag{4.23}$$

The second equation is expressed in conventional units and is the well-known universal relation for the binding energy of the shallow diatom [1]. It should be mentioned here that the two-body sector can also be solved exactly using a nonrelativistic version of the Litim cutoff [78], which is optimized in the sense of [19, 20, 18]. The drawback of this cutoff is that it breaks Galilean symmetry and one has to put some Galilean noninvariant counter terms into $P_\varphi^{UV}(Q)$ to restore Galilean symmetry in the IR.

It is important to stress the appearance of universality in the broad resonance limit ($h^2 \to \infty$) [95]: The IR physics becomes insensitive to the initial conditions in the UV. For example, one may consider possible momentum-dependent modifications of the microscopic inverse propagator $P_{\varphi,k=\Lambda}$, which result in deviations from an exactly pointlike form. Their effect on $P_{\varphi,k=0}$ is suppressed by h^{-2} with respect to the quantum loop contribution and it

therefore becomes irrelevant in the broad resonance limit. In vacuum, and for $h \to \infty$, the only physically relevant scale is given by the scattering length a.

Physics becomes *completely universal* if we perform the unitarity limit, $h^2 \to \infty$ (broad resonance limit) and $a^{-1} \to 0$ (resonance limit) [36]. In vacuum, all scales drop out in this limit. The atom and diatom inverse propagators take the following form

$$P_\psi(Q) = i\omega_{\vec{q}} + \vec{q}^2, \qquad P_\varphi(Q) = \tilde{Z}\sqrt{\frac{i\omega_{\vec{q}}}{2} + \frac{\vec{q}^2}{4}}. \tag{4.24}$$

An alternative quantum-mechanical derivation of Eq. (4.24) can be found in Appendix C.

Let us perform a scaling dimension counting in the unitary limit.[9] We start with the fact that $[\Gamma] = 0$. In nonrelativistic physics, energy scales as two powers of momentum[10] and the free field scaling reads

$$[q] = 1, \qquad [\omega] = 2, \qquad [\psi] = 3/2, \qquad [\varphi] = 3/2, \qquad [h] = 1/2. \tag{4.25}$$

For the universal interacting theory the scaling of φ is modified according to Eq. (4.24). The scaling dimension of the diatom field φ and Yukawa coupling h can be computed from the Yukawa term and the kinetic term of φ

$$[h] + [\varphi] + 2[\psi] = 5 \qquad \text{Yukawa}, \qquad 2[h] + 2[\varphi] + 1 = 5 \qquad \text{Kinetic}. \tag{4.26}$$

This system is degenerate and we get a solution $[h] = \alpha$ and $[\varphi] = 2-\alpha$, where α is some real number. The absence of a scaling of h in Eq. (4.10), however, fixes $[h] = 0$ and $[\varphi] = 2$. Note that the scaling of the diatom field at unitarity is different to the scaling of the atom field ψ. This is a manifestation of the fact that the scaling in the two-body sector is governed by a fixed point,[11] which is different from the Gaussian fixed point [98, 99, 94]. Exactly at unitarity no obvious scales are left in the problem and the theory seems to be scale invariant. Even more, at the level of two-body sector the theory seems to be an example of a nonrelativistic conformal field theory (NRCFT).[12] This type of theories are symmetric with respect to the *Schrödinger group*, which is an extension of the Galilean symmetry group (for more details see Appendix B). It is known, however, that the Schrödinger symmetry can be

[9] We denote a scaling dimension of some quantity X by $[X]$.

[10] This is known as the dynamical exponent $z = 2$.

[11] called a unitarity fixed point

[12] Another example of NRCFT in two spatial dimensions is a theory of anyons [43].

broken by a quantum anomaly in higher-body sectors [44]. The fate of the Schrödinger symmetry is different for the different systems considered. For the resonantly interacting particles (Systems I and III) it was demonstrated by Efimov [3] a long time ago that in the three-body sector the continuous scaling symmetry, which is a part of the Schrödinger symmetry, is broken to the discrete scaling subgroup Z [1]. This manifests itself in the appearance of a geometric spectrum of bound states in the three body sector. For the System II of SU(2) symmetric fermions it is believed that the Schrödinger symmetry is not broken in the higher sectors of the theory and that this is a real example of an NRCFT [43].

To summarize, in this section we have solved exactly the two-body sector in vacuum. The solution (4.21) was obtained for the specific initial conditions $h_{k=\Lambda}(Q_1, Q_2) = h$, $\lambda_{\psi,k=\Lambda} = 0$ and $P_{\varphi,k=\Lambda}(Q)$ given by Eq. (4.15). This choice corresponds to a pointlike microscopic atom interaction. However, the presented calculations can be generalized to an arbitrary boson mediated atom interaction with $\lambda_{\psi,k=\Lambda} = 0$ while $h_{k=\Lambda}(Q_1, Q_2)$ and $P_{\varphi,k=\Lambda}(Q)$ can be chosen freely.

4.4 Three-body Sector: flow equations

The main emphasis of this Chapter is devoted to the analysis of the three-body sector of the three models (4.2), (4.3) and (4.4) in the unitarity limit. We demonstrate the appearance of the Efimov effect in Systems I and III and its absence in System II from the field theoretical RG perspective. In the present Section we formulate a flow equation for the coupling $\lambda_3(Q_1, Q_2, Q_3)$ and make some general simplifications. In the next Section we use the pointlike approximation for $\lambda_3(Q_1, Q_2, Q_3)$ to solve the problem. The last two Sections are devoted to the solution of the general momentum-dependent form of the flow equation.

The closed, exact solution for the two-body sector provides a simple strategy for a computation of the coupling λ_3 in the three-body sector. In general, one may introduce separate cutoffs R_ψ and R_φ for the atoms ψ and diatoms φ. The presence of the cutoff R_φ does not affect our computation in the two-body sector. We may therefore first lower the cutoff R_ψ from Λ^2 to zero, while keeping R_φ fixed, and subsequently lower R_φ to zero in a second step [9]. As the result of the first step the diatom inverse propagator P_φ is modified according to Eq. (4.21). This step also induces diatom interactions, as for example a term $\sim (\varphi^*\varphi)^2$. However, these interactions belong to the four-body and higher sectors. By virtue of the vacuum hierarchy, they do not influence the flow of λ_3. For the second step of our computation we can

therefore use a version of the flow equation where only the diatom cutoff R_φ is present. In this flow equation P_φ and P_ψ are fixed according to Eqs. (4.21) and (4.12).

Similar to our studies of the inverse square potential in Chapter 3, for the diatoms we use a sharp cutoff

$$R_\varphi(Q,k) = P_\varphi(Q)\left(\frac{1}{\theta(|q|-k)} - 1\right). \tag{4.27}$$

The special feature of this cutoff is that the regularized diatom propagator takes a simple form

$$\frac{1}{P_\varphi(Q) + R_\varphi(Q,k)} = \theta(|q|-k)\frac{1}{P_\varphi(Q)}. \tag{4.28}$$

Thus the propagator is cut off sharply at the sliding scale k. Our choice of the cutoff is motivated by technical simplicity as well as effective theory [1] and quantum mechanical [3] approaches to this problem. The advantage of this cutoff is the property of locality in the momentum space, which means that it chops off momentum shells locally.

Let us now calculate the flow equation of the 1PI atom-diatom vertex λ_3. For SU(3) fermions there are two atom-diatom vertices, λ_{3a} and λ_{3b}, and we postpone the analysis of this model to the end of the Section. In Minkowski space (the real time version of our theory) the atom-diatom scattering amplitude is given by the amputated connected part of the Green function $\langle 0|\varphi\psi\varphi^\dagger\psi^\dagger|0\rangle$, and thus it can be simply calculated from the knowledge of λ_3.

We first consider the kinematics of the problem. The 1PI atom-diatom vertex $\lambda_3(Q_1,Q_2,Q_3)$ depends generally on three four vectors, i.e. six independent rotation invariant variables in the center-of-mass frame. We take the incoming atom and diatom to have momenta $\vec{q}_1$ and $-\vec{q}_1$, and energies $E_{\psi 1}$ and $E-E_{\psi 1}$, while the outgoing atom and diatom have momenta $\vec{q}_2$ and $-\vec{q}_2$ and energies $E_{\psi 2}$ and $E-E_{\psi 2}$. We denote the vertex in the center-of-mass frame by $\lambda_3(Q_1^\psi, Q_2^\psi, E)$ (see Figure 4.3). This configuration is in general off-shell which is necessary since, in the flow equations, the vertex also appears inside a loop.

The flow equation for the atom-diatom vertex λ_3 for the Systems I and

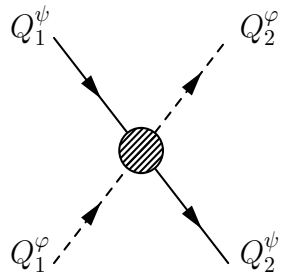

Figure 4.3: Kinematics of the vertex $\lambda_3(Q_1^\psi, Q_2^\psi, E)$ in the center-of-mass frame. The atoms and diatoms have momenta $Q_1^\psi = (E_{\psi 1}, \vec{q}_1)$, $Q_1^\varphi = (-E_{\psi 1} + E, -\vec{q}_1)$ and $Q_2^\psi = (E_{\psi 2}, \vec{q}_2)$, $Q_2^\varphi = (-E_{\psi 2} + E, -\vec{q}_2)$.

Model	A	B	C
System I	1	2	1
System II	1	-2	1
System III(a)	1	-2	1
System III(b)	4	4	1

Table 4.1: Numerical coefficients A, B and C in the flow equation (4.29) for the three examined systems. In the case of System III(a) we consider the scattering of the type $\psi_i\varphi_j \to \psi_i\varphi_j$ with $i \neq j$, while System III(b) corresponds to the the vertex $\lambda_3 = 3\lambda_{3a} + \lambda_{3b}$

II reads

$$\partial_t \lambda_3(Q_1^\psi, Q_2^\psi; E) = \int_L \tilde{\partial}_t \frac{\theta(|\vec{l}| - k)}{P_\psi(L) P_\varphi(-L+Q)} \Big[C\lambda_3(Q_1^\psi, L; E)\lambda_3(L, Q_2^\psi; E)$$
$$+ \frac{B}{2}\Big(\frac{h^2}{P_\psi(-L+Q_1^\varphi)}\lambda_3(L, Q_2^\psi; E) + \lambda_3(Q_1^\psi, L; E)\frac{h^2}{P_\psi(-L+Q_2^\varphi)}\Big)$$
$$+ A\frac{h^2}{P_\psi(-L+Q_1^\varphi)}\,\frac{h^2}{P_\psi(-L+Q_2^\varphi)}\Big], \tag{4.29}$$

where $Q = Q_1^\varphi + Q_1^\psi = (E, \vec{0})$. The coefficients A, B and C for Systems I, II can be found in Table 4.1. The graphical representation of this equation is depicted in Figure 4.4. The scale derivative on the RHS acts only on the cutoff and can be computed easily, $\tilde{\partial}_t \theta(|\vec{l}| - k) = -k\delta(|\vec{l}| - k)$.

Fortunately, the flow equation can be simplified considerably. First note that there is only one inverse propagator $P_\psi(L)$ with a loop momentum L of positive sign in Eq. (4.29). For this reason the whole integrand in Eq. (4.29)

has a single frequency pole in the upper half plane. Thus the frequency integration in Eq. (4.29) can be performed with the help of the residue theorem by performing the substitution $\omega_{\vec{l}} \to i\vec{l}^2$. This puts the atom in the loop on-shell, corresponding to $P_\psi(L)$ in Eq. (4.29). We obtain a simpler equation if we also put the energies of the incoming and outgoing atoms on-shell ($Q_1^\psi = (i\vec{q}_1^2, \vec{q}_1)$, $Q_2^\psi = (i\vec{q}_2^2, \vec{q}_2)$). The diatoms in the loop in Eq. (4.29) are generally off-shell. To solve this "half-off-shell" equation only the values $\lambda_3(\vec{q}_1, \vec{q}_2, E) \equiv \lambda_3(Q_1^\psi = (i\vec{q}_1^2, \vec{q}_1), Q_2^\psi = (i\vec{q}_2^2, \vec{q}_2), E)$ are needed [1].

Remember that the flow equation of the effective action (2.1) is formulated in Euclidean spacetime (imaginary time formalism). In order to make connection to the effective field theory studies [1] we transform the flow equation to Minkowski space. To achieve this goal it is sufficient to take external frequencies ω_{ext} to be imaginary, i.e. perform a transformation $\omega_{\rm ext} \to i\omega_{\rm ext}$, which is the inverse Wick rotation.

Our aim is the calculation of the atom-diatom scattering amplitude at *low energies and momenta*. For low momenta the dominant contribution is given by s-wave scattering. In principle, the right hand side of Eq. (4.29) has also contributions from higher partial waves, which we neglect in our approximation and simplify the flow equation (4.29) by projecting on the s-wave. This is done by averaging Eq. (4.29) over the cosine of the angle between incoming momentum $\vec{q}_1$ and outgoing momentum $\vec{q}_2$. Introducing the averaged 1PI renormalized vertex, which depends on three scalar variables

$$\lambda_3(q_1, q_2, E) \equiv \frac{1}{2h^2} \int_{-1}^{1} d(\cos\theta) \lambda_3(\vec{q}_1, \vec{q}_2, E), \tag{4.30}$$

we end up with the flow equation

$$\partial_t \lambda_3(q_1, q_2, E) = -\frac{2(3+p)}{\pi} \frac{k^3}{\sqrt{\frac{3k^2}{4} - \frac{E}{2} - i\epsilon}} \Big[C\lambda_3(q_1, k, E)\lambda_3(k, q_2, E) + \frac{B}{2} \{\lambda_3(q_1, k, E)G(k, q_2) + G(q_1, k)\lambda_3(k, q_2, E)\} + AG(q_1, k)G(k, q_2) \Big], \tag{4.31}$$

where the symmetric function $G(q_1, q_2)$ is defined by[13]

$$G(q_1, q_2) = \frac{1}{4q_1 q_2} \log \frac{q_1^2 + q_2^2 + q_1 q_2 - \frac{E}{2} - i\epsilon}{q_1^2 + q_2^2 - q_1 q_2 - \frac{E}{2} - i\epsilon}. \tag{4.32}$$

[13]This is in fact coincides with a s-wave projected tree (one-particle-reducible) contribution to the fully connected atom-diatom vertex $\lambda_3(q_1, q_2, E)$.

The infinitesimally positive $i\epsilon$ term arises from the Wick rotation and makes both Eq. (4.31) and (4.32) well-defined. Note that Eq. (4.31) is completely independent of the Yukawa coupling h and thus is a well-defined equation in the limit of infinite h.

For $SU(3)$ fermions the situation is more complicated because there are two vertices λ_{3a} and λ_{3b} in our truncation (4.4). To extract the flow equation for λ_{3a} we consider the scattering channel $\varphi_i\psi_i \to \varphi_j\psi_j$ with $i \neq j$ (e.g. $\varphi_1\psi_1 \to \varphi_2\psi_2$). After performing the same steps as for System I and II, we obtain with a flow equation

$$\begin{aligned}
\partial_t \lambda_{3a}(q_1,q_2,E) = &-\frac{2(3+p)}{\pi}\frac{k^3}{\sqrt{\frac{3k^2}{4}-\frac{E}{2}-i\epsilon}}\times \\
&\Big[3\lambda_{3a}(q_1,k,E)\lambda_{3a}(k,q_2,E)+2\lambda_{3a}(q_1,k,E)\lambda_{3b}(k,q_2,E) \\
&+2\left\{\lambda_{3a}(q_1,k,E)G(k,q_2)+G(q_1,k)\lambda_{3a}(k,q_2,E)\right\} \\
&+\left\{\lambda_{3b}(q_1,k,E)G(k,q_2)+G(q_1,k)\lambda_{3b}(k,q_2,E)\right\} \\
&+G(q_1,k)G(k,q_2)\Big],
\end{aligned} \tag{4.33}$$

where $p=-1$ and $G(q_1,q_2)$ is defined in Eq. (4.32). Note, that the coupling λ_{3b} appears in the flow equation for λ_{3a}. The flow equation for λ_{3b} can be extracted by considering the scattering channel $\varphi_i\psi_j \to \varphi_i\psi_j$ with $i \neq j$ (e.g. $\varphi_2\psi_1 \to \varphi_2\psi_1$)

$$\begin{aligned}
\partial_t \lambda_{3b}(q_1,q_2,E) = &-\frac{2(3+p)}{\pi}\frac{k^3}{\sqrt{\frac{3k^2}{4}-\frac{E}{2}-i\epsilon}}\times \\
&\Big[\lambda_{3b}(q_1,k,E)\lambda_{3b}(k,q_2,E) \\
&+\left\{\lambda_{3b}(q_1,k,E)G(k,q_2)+G(q_1,k)\lambda_{3b}(k,q_2,E)\right\} \\
&+G(q_1,k)G(k,q_2)\Big].
\end{aligned} \tag{4.34}$$

This equation is completely decoupled from Eq. (4.33) and has exactly the same form as Eq. (4.31) for $SU(2)$ fermions. The reason for this is simple: The RG equation (4.34) has the graphical representation depicted in Figure 4.4. It turns out that in this channel only one type of diatom (in our example φ_2) and two types of atoms (ψ_1 and ψ_3) appear, which is exactly the same as in the case of $SU(2)$ fermions. Remarkably, it is possible to introduce a linear combination $\lambda_3 \equiv 3\lambda_{3a}+\lambda_{3b}$ for $SU(3)$ fermions, which has a simple flow equation of the form (4.31) with coefficients A, B and C given in Table 4.1 (forth line). We call this System III(b). In the SU(3) fermion model the

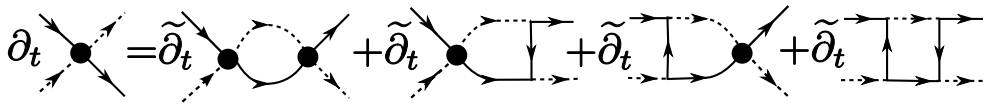

Figure 4.4: Graphical representation of the flow equation for λ_3. Full lines denote atoms ψ and dashed lines diatoms φ. The shaded circle denotes the three-point vertex λ_3.

diatom-atom in-state $\varphi_i\psi_i$ can lead to the different diatom-atom out-states $\varphi_1\psi_1$, $\varphi_2\psi_2$ and $\varphi_3\psi_3$. If the diatom-atom out-state is not a final but only an intermediate state (e.g. one is interested in the scattering into a three atom final state), we must sum the scattering amplitudes for all possible atom-diatom pairs. It easy to show that $\lambda_3 = 3\lambda_{3a} + \lambda_{3b}$ corresponds to the 1PI contribution to the full scattering amplitude $\varphi_i\psi_i \to \textit{anything}$ (e.g. $\varphi_i\psi_i \to \varphi_1\psi_1 + \varphi_2\psi_2 + \varphi_3\psi_3$).

To summarize, although at first sight it seems that for SU(3) fermions we must solve a system of two flow equations, it turns out that for the two specific situations it is sufficient to solve only *one equation* (4.31). This equation is the main result of this Section. In the next Sections we solve this final version of the RG flow equation for atom-diatom 1PI vertex for all three systems using various approaches.

4.5 Three-body sector: pointlike approximation

In this Section the flow equation (4.31) will be solved employing a simple and intuitive pointlike approximation. The 1PI vertex $\lambda_3(q_1, q_2, E)$ will be replaced by a single momentum-independent coupling $\lambda_3(E)$. In the low energy limit ($E \to 0$) the flow equation (4.31) takes a simple form in the pointlike approximation

$$\partial_t \lambda_3^R = -\frac{4(3+p)}{\sqrt{3}\pi}\left[\frac{A}{4} + \frac{B}{2}\lambda_3^R + C(\lambda_3^R)^2\right] + 2\lambda_3^R, \tag{4.35}$$

where we use $G(q \to 0, k) \to \frac{1}{2k^2}$ from Eq. (4.32). The renormalized coupling is defined as $\lambda_3^R = \lambda_3 k^2$. This definition is motivated by a simple power counting near the unitary fixed point ($[\varphi\psi\varphi^*\psi^*] = 7 \to [\lambda_3] = -2 \to [\lambda_3^R] = 0$). The RHS of Eq. (4.35) is a quadratic polynomial in λ_3^R with constant coefficients. This type of RG equation was discussed in detail in Section 3.2.

Model	D	T	s_0
System I	-7.762	2.255	1.393
System II	9.881	–	–
System III(a)	9.881	–	–
System III(b)	-7.762	2.255	1.393

Table 4.2: Discriminant D, temporal RG period T (if applicable) and Efimov parameter s_0 (if applicable) in the pointlike approximation for Systems I, II, III(a) and III(b).

We remind that the behavior of the solution is governed by the *sign* of the discriminant D of the quadratic polynomial on the RHS of Eq. (4.35)

- $D > 0$ – a solution with two fixed points.
- $D = 0$ – a solution with a sigle fixed point.
- $D < 0$ – periodic limit cycle solutions with a period $T = \frac{2\pi}{\sqrt{-D}}$.

The discriminant is given by

$$D = 4\left(1 - \frac{B(3+p)}{\sqrt{3}\pi}\right)^2 - \frac{16AC(3+p)^2}{3\pi^2}. \tag{4.36}$$

In the special case of the Systems I, II and III the solution in the pointlike approximation is summarized in Table 4.2. For Systems II and III(a) we find the solution with an IR fixed point. For Systems I and III(b) the situation is completely different. We obtain a periodic limit cycle solution of the form $\lambda_3^R(t) \sim \tan[\pi t/T]$. The intuitive interpretation of this solution is that during the RG flow we hit three-body diatom-atom bound states, which manifest themselves as divergences of λ_3^R. In the unitary limit there are infinitely many of these bound states, which are equidistant in a logarithmic scale. The continuous scaling symmetry is broken to the discrete Z group. This is a manifestation of the Efimov effect [3, 1], which indeed is present for equivalent bosons (System I) and is absent in the case of SU(2) fermions. In the case of equivalent bosons (System I) the Efimov result is

$$\frac{E_{n+1}}{E_n} = \exp(-2\pi/s_0) \tag{4.37}$$

with E_{n+1} and E_n denoting neighboring bound state energies. The Efimov parameter s_0 is given by the solution of a transcendental equation and one

finds $s_0 \approx 1.00624$ [3]. By dimensional arguments we can connect the artificial sliding scale k^2 with the scattering energy E as $E \sim k^2$ [85]. The proportionality factor disappears in the ratio of the energies and hence the Efimov parameter can be read off from the RG period

$$\frac{k_{n+1}^2}{k_n^2} = \frac{E_{n+1}}{E_n} = \exp(-2T) \Rightarrow s_0 = \frac{\pi}{T}. \tag{4.38}$$

The values of the Efimov parameter for Systems I and III(b) can be found in Table 4.2. We obtain $s_0 \sim 1.393$, which differs from the correct result by 40%. In the next two Sections we demonstrate that the simple pointlike approximation is too crude to get the correct quantitative agreement. Nevertheless it provides us with the first hint how the Efimov effect appears also in the functional renormalization group framework.

4.6 Three-body sector: systems I and II

In this Section we only discuss Systems I and II leaving the analysis of System III to the next Section. It turns out that in these two cases the flow equation (4.31) for $E = 0$ can be formally solved exactly. For two-component fermions this was shown by Diehl et. al. in [77]. To find the exact solution most easily we perform the following redefinition

$$f_t(t_1, t_2, E) \equiv 4(3+p)q_1 q_2 \lambda_3(q_1, q_2, E) \qquad g(t_1, t_2) \equiv 4(3+p)q_1 q_2 G(q_1, q_2), \tag{4.39}$$

where, from now on, we prefer to work with logarithms of momenta $t_1 = \ln(q_1/\Lambda)$ and $t_2 = \ln(q_2/\Lambda)$. As before $p = +1$ ($p = -1$) in the case of bosons (fermions). The RG scale dependence of the reduced atom-diatom vertex $f_t(t_1, t_2, E)$ is denoted by the subscript t. It is important to stress that we are generally interested in the solution of Eq. (4.31) for the scattering of particles of nonzero energy E. Nevertheless, we observe that the energy E cuts off the RG flow in Eq. (4.31) in a similar way as the regulator $R = k^2$. With this relation between k^2 and E in mind, the coupling for $k \neq 0$ and $E = 0$ imitates the effect of a nonzero energy of the scattering particles, i.e. $k = 0$, $E \neq 0$.

The flow equation at vanishing energy $E = 0$ now reads

$$\begin{aligned} \partial_t f_t(t_1, t_2) = -\frac{1}{\sqrt{3}\pi}\Big[& A g(t_1, t) g(t, t_2) \\ & + \frac{B}{2}\left\{ f_t(t_1, t) g(t, t_2) + g(t_1, t) f_t(t, t_2) \right\} \\ & + C f_t(t_1, t) f_t(t, t_2) \Big]. \end{aligned} \tag{4.40}$$

We assume that in the UV the reduced atom-diatom 1PI vertex is vanishing, i.e. the initial condition is $f_{t=0}(t_1, t_2) = 0$. In general we are dealing with the Riccati differential equation in matrix form, where both matrices g and f_t have a continuous index running in the interval $t_1, t_2 \in (-\infty, 0)$. The RHS of Eq. (4.40) is a complete square, which is a special feature of the Systems I and II (see Table 4.1). In order to find the formal solution of Eq. (4.40) we define

$$\bar{f}_t(t_1, t_2) = p f_t(t_1, t_2) + g(t_1, t_2), \tag{4.41}$$

which can be recognized as the reduced, fully connected atom-diatom vertex. The flow equation for the full vertex $\bar{f}_t(t_1, t_2)$ and the initial condition take the simple form

$$\partial_t \bar{f}_t(t_1, t_2) = -\frac{p}{\sqrt{3}\pi} \bar{f}_t(t_1, t) \bar{f}_t(t, t_2), \qquad \bar{f}_{t=0}(t_1, t_2) = g(t_1, t_2). \tag{4.42}$$

It is convenient to rewrite Eq. (4.42) in matrix notation ($\bar{f}_t(t_1, t_2) \to \bar{f}_t$)

$$\partial_t \bar{f}_t = -\frac{p}{\sqrt{3}\pi} \bar{f}_t \cdot A_t \cdot \bar{f}_t, \qquad \bar{f}_{t=0} = g, \tag{4.43}$$

where A_t has matrix elements $A_t(t_1, t_2) = \delta(t - t_1)\delta(t - t_2)$ and matrix multiplication denotes t-integration. Multiplying both sides of Eq. (4.43) from the left and right by $\bar{f}_t^{-1}$ we obtain

$$\partial_t \bar{f}_t^{-1} = -\bar{f}_t^{-1} \cdot \partial_t \bar{f}_t \cdot \bar{f}_t^{-1} = \frac{p}{\sqrt{3}\pi} A_t, \qquad \bar{f}_{t=0}^{-1} = g^{-1}, \tag{4.44}$$

which is formally solved by

$$\bar{f}_t = \left(I + \frac{p}{\sqrt{3}\pi} \int_0^t ds g \cdot A_s \right)^{-1} \cdot g \tag{4.45}$$

for $t \in (-\infty, 0)$. I denotes the identity matrix.

In the IR limit $t \to -\infty$, which corresponds to integration of all quantum fluctuations, $\bar{f} \equiv \bar{f}_{t=-\infty}$ solves the following matrix equation

$$\bar{f} = g + \frac{p}{\sqrt{3}\pi} g \cdot \bar{f}. \tag{4.46}$$

This is the well-known STM integral equation[14] for bosons ($p = +1$) and fermions ($p = -1$) for the half-off-shell, amputated, connected Green function [1].

[14] up to our redefinition (4.39)

The difference of the signs in Eq. (4.45) between System I and II turns out to be crucial. In order to see that, we solve Eq. (4.45) numerically by discretization. A series of cartoons of the evolution of the reduced 1PI vertex $f_t(t_1, t_2)$ for both systems is shown in Figure 4.5. For fermions, first a peak appears in the UV ($t_1 = 0, t_2 = 0$), which propagates in the diagonal direction ($t_1 = t_2$) during the RG evolution. On the other hand, for bosons, a periodic structure (with period $T_{spatial} \approx 6.2$ in both directions) develops gradually. Now it is clear why the approximation investigated in the last Section failed to give the quantitatively correct result. The pointlike approximation, which corresponds to a planar landscape (no t_1 and t_2 dependence, see Section 4.5), is not valid in the three-body sector (for more details see Appendix C). The evolution in the RG time t of a single point $f_t(t_1 = 0, t_2 = 0)$ in the landscape for both systems is depicted in Figure 4.6. While for fermions the evolution is monotonic in time, in the case of bosons we obtain a "temporal" oscillation of period $T_{temp} \approx 3.1$. For different points in the $t_1 - t_2$ plane the "time" evolution is triggered at the scale $t_{in} \sim O(t_1, t_2)$.

The numerical solution for bosons is consistent with the results of [70, 71]. Spatial and temporal oscillations are correlated. As found in [70, 71] evolution in the RG time develops a limit cycle behavior. The Efimov parameter s_0 can be calculated $s_0 = \frac{\pi}{T_{temp}} \approx 1.0$ (see Section 4.5) which is in a good agreement with the Efimov result $s_0 \approx 1.00624$. The accuracy of our result is limited by the numerical procedure only.

4.7 Three-body sector: system III

As introduced in Section 4.4 for $SU(3)$ fermions there are two specific situations (System III(a) and System III(b)), when there is a single flow equation instead of the general two. Fortunately, both cases can formally be solved for $E = 0$ in a similar fashion to Section 4.6. In fact, System III(a) is completely equivalent to System II (see Table 4.2) such that we obtain a fixed point solution in this case (see Figure 4.6). For System III(a) we follow similar steps as in Section 4.6: we define a reduced atom-diatom 1PI vertex $f_t(t_1, t_2, E)$ (4.39) and obtain a flow equation for the reduced vertex (4.40) with the coefficients $A = 4$, $B = 4$ and $C = 1$. These coefficients form a complete square and thus it is useful to define the fully connected atom-diatom vertex

$$\bar{f}_t(t_1, t_2) = f_t(t_1, t_2) + 2g(t_1, t_2). \tag{4.47}$$

The flow equation (4.40) now reads

$$\partial_t \bar{f}_t(t_1, t_2) = -\frac{1}{\sqrt{3}\pi} \bar{f}_t(t_1, t) \bar{f}_t(t, t_2), \qquad \bar{f}_{t=0}(t_1, t_2) = 2g(t_1, t_2). \tag{4.48}$$

The equation and the initial condition are identical to Eq. (4.42) for bosons.[15] For this reason we expect the appearance of the Efimov effect for the $SU(3)$ fermionic System III(b) with the Efimov parameter $s_0 \sim 1.00624$.

At first sight it seems surprising that both bosons and $SU(3)$ fermions have the identical Efimov parameter s_0. As explanation, we propose a simple possible quantum mechanical argument: In order to find a bound state spectrum for SU(3) fermions one must solve the three-body Schrödinger equation. The total wave function must be totally *antisymmetric* for fermions. We can achieve this by taking the total wave function as the product of a totally antisymmetric flavor part ($\epsilon_{ijk}|i> |j> |k>$) times a totally *symmetric* orbital part. Hence the orbital part has the same symmetry property as the bosonic case. Only the orbital part is needed for the quantum mechanical calculation of the bound state problem, which leads to the identical Efimov parameters for bosons and SU(3) fermions.

4.8 Summary

In this Chapter we applied the method of functional renormalization to the two- and three-body physics of atoms near a Feshbach resonance. We investigated three different systems, namely identical bosons as well as two and three species of fermions. The two-body sector was solved exactly. The unitarity limit is governed by a fixed point and all three systems seem to be examples of the nonrelativistic conformal field theories. In the three-body sector, however, no infrared fixed point exists for bosons and three-component fermions. We solved the momentum-dependent problem of the three-body sector at unitarity. This leads to the Skorniakov-Ter-Martirosian equation, well-known from quantum mechanics. A numerical solution for $U(1)$ bosons and $SU(3)$ fermions shows the emergence of the Efimov effect; the appearance of an infinite geometric spectrum of triatom states. Hence in these systems the continuous scaling symmetry is broken to the discrete scaling subgroup Z by a quantum anomaly. The renormalization group flow develops a limit cycle behavior (see Figure 4.6). The Efimov parameter s_0 for the three-component fermions is found to be identical to the Efimov parameter of the well-studied bosonic case, which agrees with the quantum-mechanical prediction.

[15] The initial condition for $SU(3)$ fermions is $\bar{f}_{t=0}(t_1, t_2) = 2g(t_1, t_2)$, while for bosons one has $\bar{f}_{t=0}(t_1, t_2) = g(t_1, t_2)$. However, for bosons $g(t_1, t_2)$ is two times larger than for fermions (4.39). Thus the initial conditions are identical.

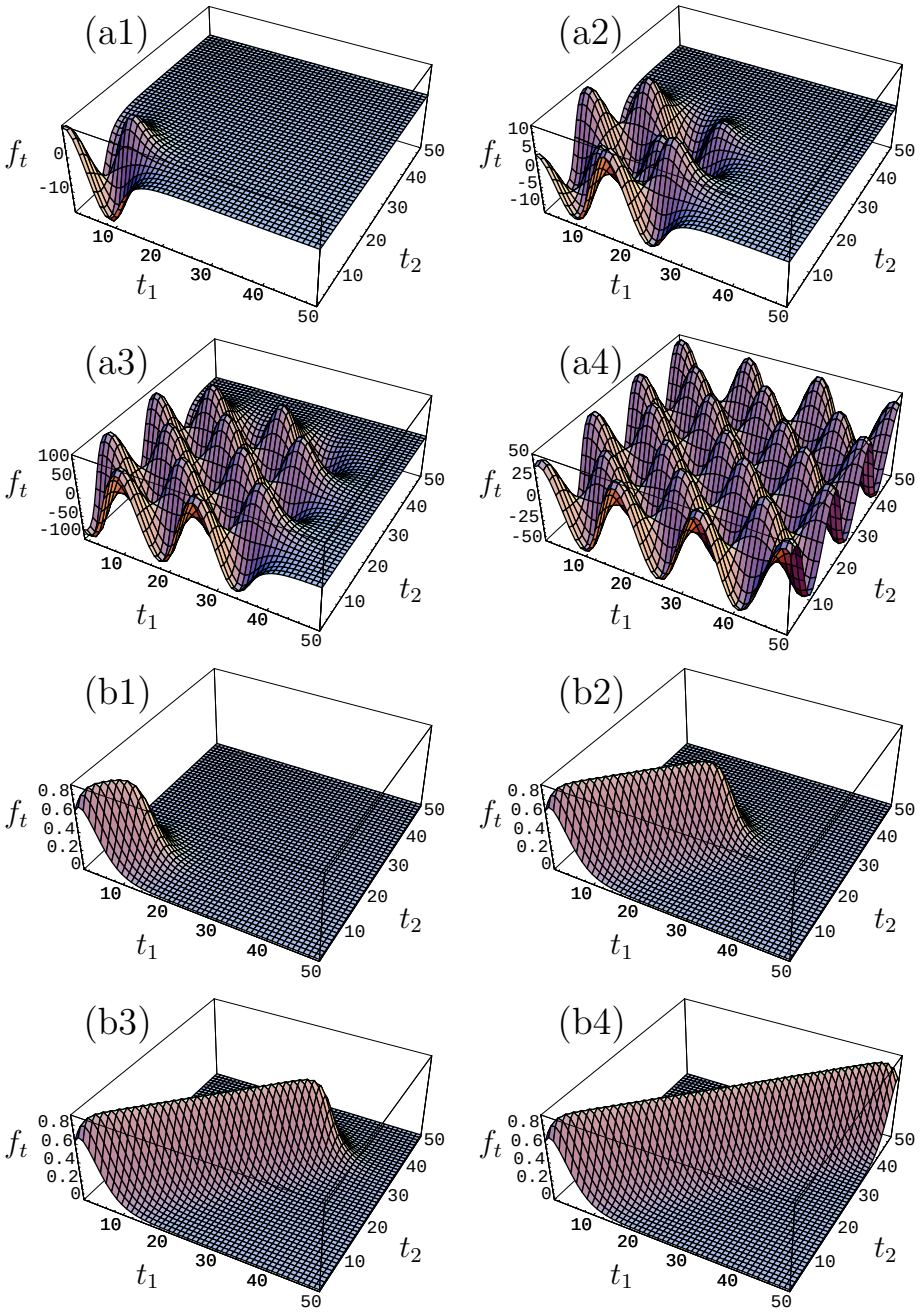

Figure 4.5: The RG evolution of the momentum dependent modified vertex $f_t(t_1, t_2) = 4(3+p)q_1q_2\lambda_3(q_1, q_2, E)$ for bosons (a1-a4) and SU(2) fermions (b1-b4). Spatial momenta t_1, t_2 and the RG time t are descritized to $N = 50$ intervals with a step $\Delta t = 0.4$. The cartoons for bosons and fermions correspond to the descritized steps $10, 25, 35, 50$.

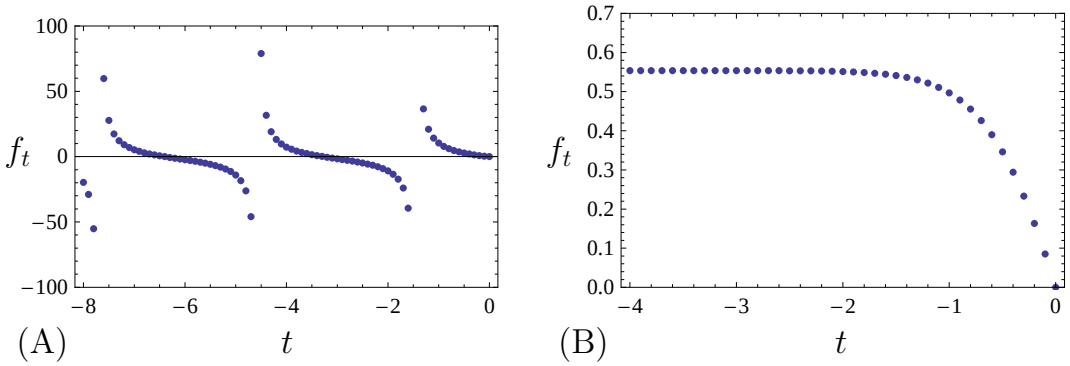

Figure 4.6: Numerical evolution in the RG time t of $f_t(t_1 = 0, t_2 = 0)$ for System I (A) and System II (B). For SU(2) fermions (B) the modified vertex approaches a fixed point solution; in the case of bosons (A), a limit cycle behavior is developed with a period $T_{temp} \approx 3.1$.

Chapter 5

Four-body Problem: Universal Tetramers

In Efimov physics the next natural step is to raise the following question: "What is the solution of the universal problem of four interacting particles?" Early attempts towards an understanding of this system were made in the context of nuclear physics using a variety of approaches [101, 102, 103, 104]. Also the four-body physics of ^{4}He atoms has been investigated in much detail, for an overview see, e. g. [105]. The simpler four-body physics of fermions with two spin states, relevant for the dimer-dimer repulsion, has also been studied [106].

In their pioneering work, Platter and Hammer, et al. [107, 108] investigated the four-body problem using effective interaction potentials and made the conjecture that the four-boson system exhibits universal behavior. They also found that no four-body parameter is needed for a self-consistent renormalization of the theory. Calculating the energy spectrum of the lowest bound states in dependence on the scattering length a the existence of two tetramer (four-body bound) states associated with each trimer was conjectured.

In 2009 von Stecher, D'Incao, and Greene [109, 110] investigated the four-body problem in a remarkable quantum mechanical calculation. They found that the Efimov trimer and tetramer states always appear as sets of states with two tetramers associated with each of the trimer levels and calculated the bound state energy spectrum of the lowest few sets of states. The calculation suggests that the energy levels within one set of states are related to each other by universal ratios, which were obtained from the behavior of these lowest sets of states. In accordance with the results of Platter et al. [107, 108] the absence of any four-body parameter was also demonstrated. Similar results were obtained recently by Deltuva in [111]. In order to find

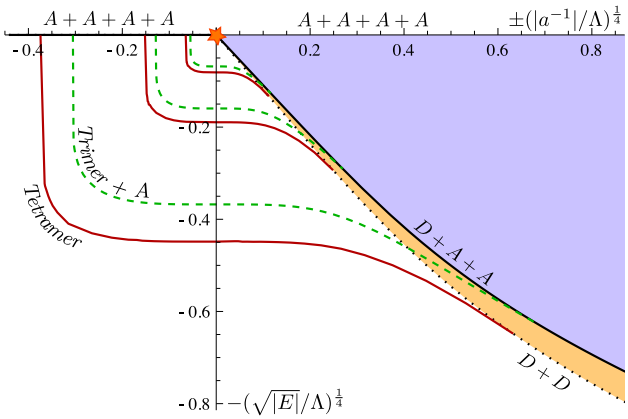

Figure 5.1: (Color online) The generalized Efimov plot for four identical bosons. Here, we plot the energy levels of the various bound states as a function of the inverse s-wave scattering length a as numerically calculated in our approximative, effective theory. In order to improve the visibility of the energy levels we rescale both the dimensionless energy E/Λ^2 and the dimensionless inverse scattering length a^{-1}/Λ where Λ denotes the UV cutoff of our model. Also, we only show the first three sets of Efimov levels. The solid black line denotes the atom-atom-dimer threshold, while the dotted black line gives the dimer-dimer threshold. In the three-body sector one finds the well known spectrum of infinitely many Efimov trimer states (green, dashed) which accumulate at the unitarity point $E_\psi = a^{-1} = 0$, indicated by the orange star. In our pointlike approximation the four-body sector features a single tetramer (solid, red) associated with each trimer state.

experimental evidence of the tetramer states extremely precise measurements are required. Remarkably, Ferlaino et al. were able to observe signatures of the lowest two of the tetramer states in the recent Innsbruck experiment [112] with cesium atoms. Four-body features were also observed by the Rice group [69] in the experiment with lithium atoms.

While the calculations by Platter et al. [107, 108], von Stecher et al. [109, 110] and Deltuva [111] rely on quantum mechanical approaches, in this Chapter we want to shed light onto the four-body problem from the perspective of functional renormalization group.

Of our special interest is the investigation of universality in the four-body system. In this context the unitarity point, illustrated by the star in Figure 5.1, is of particular importance. At this point not only the scattering length a is infinite but also all binding energies in the problem accumulate at the atom threshold at zero energy. Only at the unitarity point physics becomes truly universal in the sense that, for example, the ratio between the

binding energies of consecutive trimer levels assumes exactly its universal value, $E_{n+1}/E_n = \exp(-2\pi/s_0)$, with the Efimov parameter $s_0 \approx 1.00624$. The unitarity point is therefore the most interesting one from a theory point of view. Unfortunately, in the previous calculations only few lowest lying states were determined. The major advantage of the FRG approach is that it allows to investigate analytically the complete spectrum and to address directly the unitarity point in order to extract the universal relations between the three- and four-body bound states in this limit.

In the previous Chapter we studied the Efimov problem in the unitary limit employing the vertex expansion. In this Chapter we use the derivative expansion to study few-body physics of ultracold atoms. This complements our findings in Chapter 4. In addition, here we investigate the renormalization group behavior of the four-body interactions with an approximate, but simple and physically intuitive model which allows only for pointlike (i.e. momentum independent[1]) three- and four-body interactions. We will find that the three-body limit cycle, discussed in detail in the previous Chapter, leads to a more complicated limit cycle of the four-body sector which is, however, attached to the three-body limit cycle. This in turn leaves no room for any four-body parameter.

The Chapter is structured as follows: In Section 5.1 we set up the microscopic model and introduce our truncation for the effective flowing action within the derivative expansion. Sections 5.2 and 5.3 are devoted to the FRG analysis of the two- and three-body sectors. In Section 5.4 we discuss the four-body sector and present our numerical results. Our findings are summarized in Section 5.5.

[1]We use the term momentum independence to refer to combined spatial momentum and frequency independence.

5.1 Derivative expansion and definition of the model

Our truncation for the Euclidean flowing action is given by a simple two-channel model

$$\begin{aligned}\Gamma_k &= \int_x \{\psi^*(\partial_\tau - \Delta + E_\psi)\psi \\ &+ \phi^* \left(A_\phi(\partial_\tau - \frac{\Delta}{2}) + m_\phi^2 \right) \phi + \frac{h}{2}(\phi^*\psi\psi + \phi\psi^*\psi^*) \\ &+ \lambda_{AD}\phi^*\psi^*\phi\psi + \lambda_\phi(\phi^*\phi)^2 \\ &+ \beta(\phi^*\phi^*\phi\psi\psi + \phi\phi\phi^*\psi^*\psi^*) + \gamma\phi^*\psi^*\psi^*\phi\psi\psi\}, \end{aligned} \tag{5.1}$$

where Δ denotes the Laplace operator and we use the natural, nonrelativistic convention $2M = \hbar = 1$ with the atom mass M. ψ denotes the field of the elementary bosonic atom, while the dimer, the bosonic bound state consisting of two elementary atoms, is represented by the field $\phi \sim \psi\psi$. Both the atom and the dimer fields are supplemented with nonrelativistic propagators with energy gaps E_ψ and m_ϕ^2, respectively. In our approximation the fundamental four-boson interaction $\sim \lambda_\psi(\psi^*\psi)^2$ is mediated by a dimer exchange, which yields $\lambda_\psi = -h^2/m_\phi^2$ in the limit of pointlike two-body interactions. The dynamical dimer field ϕ allows us to capture essential details of the momentum dependence of the two-body interaction. The linear ansatz for the inverse dimer propagator with the flowing wave function renormalization factor differs from the exact result, discussed in the previous Chapter. Nevertheless, it allows us to take into account the anomalous dimension of the dimer field and is very convenient for practical calculations. The only nonzero interaction, present at the microscopic UV scale $k = \Lambda$, is taken to be the Yukawa-type term with the coupling h. Together with the microscopic value of A_ϕ the Yukawa interaction h at the UV scale can be connected to the effective range r_{eff} in an effective range expansion (see Appendix D). The atom-dimer interaction λ_{AD} as well as the various four-body interactions λ_ϕ, β, and γ vanish at the UV scale and are built up via quantum fluctuations during the RG flow.

At this stage we want to emphasize the meaning of the term pointlike approximation which must not be confused with the notion of a zero-range (contact) model. Consider for example the two-body contact interaction $\sim \lambda_\psi(\psi^*\psi)^2$, which has no momentum dependence at the UV scale, $k = \Lambda$. In order to describe the scattering of two particles in quantum mechanics one proceeds by solving the two-body Schrödinger equation. From this one obtains the well-known result for the zero-range s-wave scattering amplitude

$f_0(p) = (-a^{-1} - ip)^{-1}$ (with $p = |\vec{p}|$ denoting the momentum of the colliding particles). The scattering amplitude becomes momentum-dependent. In the RG approach one deals with the effective vertex λ_ψ which varies with the RG scale k. On the UV ($k = \Lambda$) scale λ_ψ is momentum-independent. When including more and more quantum fluctuations – meaning lowering the RG scale k from Λ to eventually $k = 0$ – the effective vertex function λ_ψ acquire a momentum dependence which in the IR limit $k = 0$ is equivalent to the result for f_0 in the zero-range model. In a pointlike approximation one ignores this generated momentum dependence. In the simple model Eq. (5.1) the three- and four-body sectors are treated strictly in the pointlike approximation. However, in the two-body sector the momentum dependence of effective vertex λ_ψ is captured by the exchange of the dynamic (i.e. momentum-dependent) dimer propagator, such that the two-body sector is treated beyond the pointlike approximation.
In the general case of nonzero density and temperature one works in the Matsubara formalism and the integral in Eq. (5.1) sums over homogeneous three-dimensional space and over imaginary time $\int_x = \int d^3x \int_0^{1/T} d\tau$. Although our method allows us to tackle a full, many-body problem at finite temperature in this way, in this thesis we are interested solely in the few-body (vacuum) physics, for which density n and temperature T vanish. For $T = 0$, $\int_x$ reduces to an integral over infinite space and time. Our truncation (5.1) is based on the simple structure of the nonrelativistic vacuum and, as demonstrated in the previous Chapter, numerous simplifications occur when solving Eq. (2.1) compared with the general, many-body case. The flowing action (5.1) has a global $U(1)$ symmetry which corresponds to particle number conservation. In the vacuum limit it is also invariant under space-time Galilei transformations which restricts the form of the nonrelativistic propagators to be functions of $\partial_\tau - \Delta$ for the atoms and $\partial_\tau - \Delta/2$ for the dimers. All couplings present in Eq. (5.1) are allowed to flow during the RG evolution and are taken to be momentum-independent in Fourier space as explained above.
Besides the ansatz of Γ_k we must choose a suitable regulator function R_k in order to solve Eq. (2.1). In this Chapter we choose optimized regulators,

$$\begin{aligned} R_\psi &= (k^2 - q^2)\theta(k^2 - q^2), \\ R_\phi &= \frac{A_\phi}{2}(k^2 - q^2)\theta(k^2 - q^2), \end{aligned} \tag{5.2}$$

with $q = |\vec{q}|$. These regulators are optimized in the sense of [19, 18] and allow to obtain analytical results.

5.2 Two-body sector

We remind that a remarkable and very useful feature of the vacuum flow equations is comprised by the special hierarchy: the flow equations of the N-body sector do not influence the renormalization group flows of the lower $N-1$-body sector. For this reason the different N-body sectors can be solved subsequently. In this spirit we first solve the two-body sector, then investigate the three-body sector in order to finally approach the four-body problem.

The solution for the two-body sector can be found analytically in our approximation.[2] The only running couplings in the two-body sector are the dimer gap m_ϕ^2 and its wave function renormalization A_ϕ. The flow equations of the two-body sector are shown in terms of Feynman diagrams in Figure 5.2(a) and read

$$\begin{aligned} \partial_t m_\phi^2 &= \frac{h^2}{12\pi^2}\frac{k^5}{(k^2+E_\psi)^2}, \\ \partial_t A_\phi &= -\frac{h^2}{12\pi^2}\frac{k^5}{(k^2+E_\psi)^3}, \end{aligned} \tag{5.3}$$

where $t = \ln\frac{k}{\Lambda}$. As there are no possible nonzero flow diagrams for the Yukawa coupling h, it does not flow in the vacuum limit.
The infrared values of the couplings h and m_ϕ^2 can be related to the low-energy s-wave scattering length a via

$$a = -\frac{h^2(k=0)}{16\pi m_\phi^2(k=0, E_\psi=0)}. \tag{5.4}$$

Knowing the analytical solution of the two-body sector, this relation can be used to fix the initial values of our model. For the UV value of the dimer gap m_ϕ^2 we find

$$m_\phi^2(\Lambda) = -\frac{h^2}{16\pi}a^{-1} + \frac{h^2}{12\pi^2}\Lambda + 2E_\psi. \tag{5.5}$$

The first term fixes the s-wave scattering length according to Eq. (5.4), while the second term represents a counterterm taking care of the UV renormalization of the two-body sector. Finally, the last term accounts for the fact that the dimer consists of two elementary atoms. Additionally, we choose $A_\phi(\Lambda) = 1$ which corresponds to the effective range $r_{\text{eff}} = -\frac{64\pi}{h^2}$ (see Appendix D for details).

[2] As we discussed in Chapter 4, the atom inverse propagator (one-body sector) is not renormalized in the nonrelativistic vacuum.

The action (5.1) can also be used for a quite accurate description of Feshbach resonances. In this context Eq. (5.1) is referred to as resonance model. In such a model m_ϕ^2 is proportional to the detuning energy of the molecule in the closed channel with respect to the atom-atom threshold [113] and the coupling h is proportional to the width of the associated Feshbach resonance being a function of the strength of the coupling to the closed channel. The choice $A_\phi(\Lambda) = 1$ then corresponds to the so-called characteristic length $r^* = -\frac{1}{2} r_{\text{eff}}$ often used in literature [1, 65].
As demonstrated in the previous Chapter, in the limit of large, positive scattering length there exists a universal, weakly bound dimer state. In order to find its binding energy we calculate the pole of the dimer propagator, corresponding to the condition $m_\phi^2(E_\psi, k = 0) = 0$, which yields in the limit $E_\psi/\Lambda^2 \ll 1$

$$\begin{aligned} E_D = -2E_\psi &= -2\left(\frac{h^2}{64\pi} - \sqrt{\frac{h^4}{(64\pi)^2} + \frac{h^2 a^{-1}}{32\pi}}\right)^2 \\ &= -\frac{2}{r_{\text{eff}}^2}\left(1 - \sqrt{1 - \frac{2r_{\text{eff}}}{a}}\right)^2 . \end{aligned} \tag{5.6}$$

In the limit $h \to \infty$, corresponding to $r_{\text{eff}} \to 0$ one recovers the result $E_D = -2/a^2$, obtained in the previous Chapter within the vertex expansion. For finite values of h Eq. (5.6) predicts deviations from the universal scaling for large inverse scattering lengths. Specifically, for finite h in the regime of intermediate values of the scattering length one finds a crossover of the dimer binding energy from the universal behavior $1/a^2$ (for $a^{-1} \ll 1$) to the behavior $E_D = 4/(a r_{\text{eff}})$ (for $a^{-1} \gg 1$).

5.3 Three-body sector

As was discussed extensively in Chapter 4, the bound state spectrum of the three-body sector is much richer than the one of the two-body system. Recall that the energy of the Efimov states exhibits a universal geometric scaling law as one approaches the unitarity point $E_\psi = a^{-1} = 0$. Remarkably, these three-body bound trimer states exist even for negative scattering lengths a where no two-body bound state is present; they become degenerate with the three-atom threshold for negative scattering length and merge into the atom-dimer threshold for positive a. An additional three-body parameter is needed in order to determine the actual positions of the degeneracies [70, 71]. In this Section we want to shortly demonstrate how Efimov physics can be treated within the derivative expansion scheme.

In our truncation, the three-body sector contains a single, pointlike $\phi^*\psi^*\phi\psi$ term with a coupling λ_{AD}, which is assumed to vanish in the UV. It is built up by quantum fluctuations during the RG flow and the corresponding Feynman diagrams of the flow equation for λ_{AD} are shown in Figure 5.2(b). First, we investigate the unitarity point, $E_\psi = a^{-1} = 0$. For this limit we are able to obtain an analytical solution for the flow equation of λ_{AD} while away from unitarity we have to rely on a numerical solution.

We remind that at the unitarity point all intrinsic length scales drop out of the problem and the system becomes classically scale invariant. At unitarity, the Yukawa coupling h is dimensionless and the only (extrinsic) length scale present is the inverse ultraviolet cutoff Λ^{-1}, which defines the validity limit of our effective theory.
In our approximation the dimer field ϕ develops a large anomalous dimension $\eta = -\frac{\partial_t A_\phi}{A_\phi} = 1$ at unitarity which is consistent with the exact solution of the two-body sector presented in the previous Chapter. As the atom and dimer propagators have vanishing gaps in the IR the two-body sector respects a continuous scaling symmetry.

In order to find the solution of the three-body sector we switch to the rescaled, dimensionless coupling $\tilde{\lambda}_{AD} \equiv \frac{k^2}{h^2}\lambda_{AD}$. One finds that the flow equation for $\tilde{\lambda}_{AD}$ becomes independent of k and h,

$$\begin{aligned}\partial_t \tilde{\lambda}_{AD} &= \underbrace{\frac{24}{25}\left(1-\frac{\eta}{15}\right)}_{a}\tilde{\lambda}_{AD}^2 \underbrace{-\frac{14}{25}\left(1-\frac{4\eta}{35}\right)}_{b}\tilde{\lambda}_{AD} \\ &+ \underbrace{\frac{26}{25}\left(1-\frac{\eta}{65}\right)}_{c}. \end{aligned} \tag{5.7}$$

As was demonstrated in Chapter 3, the behavior of the solution of this type of flow equation is determined by the sign of the discriminant D of the right hand side of Eq. (5.7) which is $D = b^2 - 4ac < 0$. Eq. (5.7) can be solved analytically and one finds (compare with Eq. (3.26))

$$\tilde{\lambda}_{AD}(t) = \frac{-b + \sqrt{-D}\tan\left(\frac{\sqrt{-D}}{2}(t+\delta)\right)}{2a}, \tag{5.8}$$

where δ is connected to the three-body parameter and determines the initial condition. We observe that also with the derivative expansion, the three-body sector exhibits a quantum anomaly: The RG flow of the renormalized coupling $\tilde{\lambda}_{AD}$ exhibits a limit cycle, which, due to its periodicity, breaks the classically continuous scaling symmetry to the discrete subgroup Z. Follow-

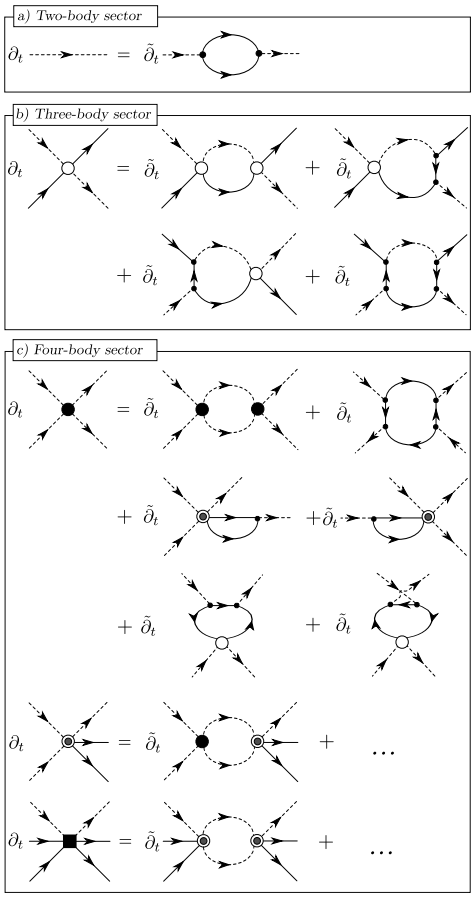

Figure 5.2: The flow equations in terms of Feynman diagrams for the (a) two-body, (b) three-body, and (c) four-body sector. Solid lines represent elementary bosons ψ, while dashed lines denote composite dimers ϕ. The vertices are: Yukawa coupling h (small black dot), atom-dimer vertex λ_{AD} (open circle), dimer-dimer coupling λ_ϕ (black circle), coupling β (two circles), and the atom-atom-dimer vertex γ (black square). Due to the large number of diagrams for the latter two vertex functions, we only show two exemplary diagrams.

ing our arguments in Chapter 4, the Efimov parameter can be now determined from the period of the limit cycle and is given in our approximation by

$$s_0 = \frac{\sqrt{-D}}{2} \approx 0.925203. \tag{5.9}$$

Considering the simplicity of our pointlike approximation, which, as discussed

in Section 5.2, does not resolve any momentum or frequency structure of the effective (k dependent) interaction vertex of the three-body sector, the agreement with the "exact" result $s_0 = 1.00624$ is quite good. In fact, the result is quantitatively much better than our finding in Section 4.5.

The presence of N-body bound states leads to divergencies in the corresponding N-body vertices. The periodic divergencies in the analytical solution of $\tilde{\lambda}_{AD}$ in Eq. (5.8) correspond therefore to the presence of the infinitely many Efimov trimer states at the unitarity point.

We can use the latter correspondence to calculate the bound state spectrum also away from unitarity. The trimer binding energies are calculated by determining the atom energies E_ψ for which $\tilde{\lambda}_{AD}$ exhibits divergencies in the IR as function of a^{-1}. The trimer binding energy is then given by $E_T = -3E_\psi$. The result is shown in Figure 5.1. In this plot the dashed, green lines indicate the binding energies of the Efimov trimer states. For calculational purposes we switch to the static trimer approximation which is completely equivalent to our two-channel model in Eq. (5.1). This procedure is described in Appendix of [114].

There is an additional universal relation obeyed by the trimer energy levels which we may take as a measure of the quality of our approximation. It is given as the relation between the trimer binding energy E^* for $a \to \infty$ and value of a for which the trimer becomes degenerate with the atom-dimer (a_+^*) and three-atom threshold (a_-^*), respectively. For comparison we define a wave number κ^* by $E^* = -\hbar^2\kappa^{*2}/M$ (in our convention, $E^* = -2\kappa^{*2}$) and find

$$a_-^*\kappa^* \approx -1.68, \quad a_+^*\kappa^* \approx 0.08 \tag{5.10}$$

which has to be compared with the exact result $a_-^*\kappa^* = -1.56(5)$, $a_+^*\kappa^* = 0.07076$ from the fully momentum-dependent calculation in [1]. The agreement with our approximate solution suggests that our model should provide a solid basis for the step to the four-body problem.

5.4 Four-body sector

Recently, the solution of the four-body problem in the low-energy limit has gained a lot of interest. In quantum mechanical calculations the existence of two tetramer (four-body bound) states was conjectured for each of the infinitely many Efimov trimers [107, 108]. By calculating the lowest few sets of bound state levels von Stecher et al. [109, 110] and Deltuva [111] concluded that both ratios of energies between the different tetramers and the trimer state approach universal constants. However, with the quantum mechanical

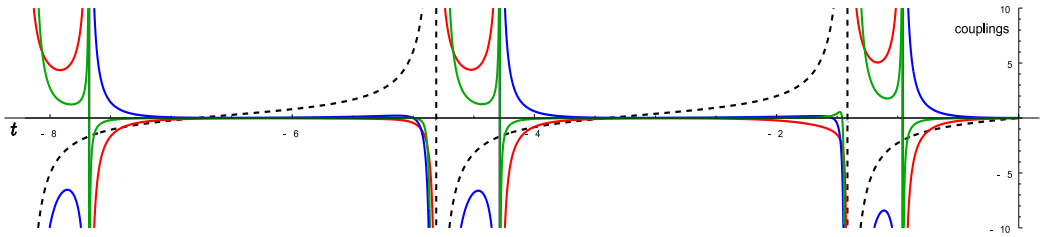

Figure 5.3: Renormalization group limit cycle behavior of the three- and four-body sector at the unitarity point $E_\psi = a^{-1} = 0$. The rescaled, dimensionless couplings $\tilde{\lambda}_{AD,1}$, $4\tilde{\lambda}_{\phi,1}$, $\tilde{\beta}_1/6$, and $\tilde{\gamma}_1/1000$ are plotted as functions of $t = \ln(k/\Lambda)$. Not only the three-body coupling $\tilde{\lambda}_{AD,1}$ (dashed, black) exhibits a limit cycle behavior, but also the four-body sector couplings $\tilde{\lambda}_{\phi,1}$ (red, solid), $\tilde{\beta}_1$ (blue, solid), and $\tilde{\gamma}_1$ (green, solid) obey a limit cycle attached to the three-body sector with the same period.

approach the calculation directly at the unitarity point ($a^{-1} = E_\psi = 0$), marked explicitly in Figure 5.1, turns out to be difficult, although this point is of great interest when one wants to gather evidence for universality of the four-body system. In fact, in the three-body sector the infinite RG limit cycle appears only exactly at the unitarity point and its universal appearance is directly connected to the breaking of the continuous scale symmetry. Within our approach, the unitarity region is easily accessible.

In order to investigate the four-body sector we include all possible, U(1) symmetric, momentum-independent interaction couplings in the effective flowing action Γ_k. If one assumes all these couplings to be zero at the microscopic UV scale Λ, one can show, by evaluating all possible Feynman diagrams and using the vacuum hierarchy described in Chapter 4, that from all possible four-body couplings only the three couplings λ_ϕ, β, and γ are built up by quantum fluctuations and are therefore included in Eq. (5.1). Couplings other than λ_ϕ, β, and γ, such as, for instance, the term $\sim (\psi^*\psi)^4$ are not generated during the RG evolution. This consideration leads to our ansatz for the effective average action (5.1).

For the investigation of the unitarity point we first switch to rescaled, dimensionless couplings

$$\tilde{\lambda}_\phi = \frac{k^3}{\pi^2 h^4}\lambda_\phi, \quad \tilde{\beta} = \frac{k^4}{h^3}\beta, \quad \tilde{\gamma} = \frac{\pi^2 k^5}{h^2}\gamma, \tag{5.11}$$

and obtain the corresponding flow equations by inserting the effective flowing action Γ_k, Eq. (5.1), into the Wetterich equation (2.1). By the use of the rescaled couplings we find three coupled ordinary differential equations,

which are again coupled to the two- and three-body sectors, but become explicitly independent of h and k. We show the diagrammatic representation of the flow equations in Figure 5.2(c). Their analytical form at the unitarity point is given by[3]

$$\partial_t \tilde{\lambda}_{AD} = \frac{128}{125} - \frac{62}{125}\tilde{\lambda}_{AD} + \frac{112}{125}\tilde{\lambda}_{AD}^2, \tag{5.12}$$

$$\partial_t \tilde{\lambda}_{\phi} = \frac{1}{16} + \frac{1}{3}\tilde{\beta} - \frac{1}{6}\tilde{\lambda}_{AD} + 3\tilde{\lambda}_{\phi} + \frac{128}{15}\tilde{\lambda}_{\phi}^2, \tag{5.13}$$

$$\begin{aligned} \partial_t \tilde{\beta} &= \frac{188}{125}\tilde{\beta} + \frac{1}{6}\tilde{\gamma} + \frac{128}{125}\tilde{\lambda}_{AD} \\ &+ \frac{224}{125}\tilde{\lambda}_{AD}\tilde{\beta} - \frac{156}{125}\tilde{\lambda}_{AD}^2 + \frac{4384}{375}\tilde{\lambda}_{\phi} \\ &+ \frac{128}{15}\tilde{\beta}\tilde{\lambda}_{\phi} - \frac{3968}{375}\tilde{\lambda}_{AD}\tilde{\lambda}_{\phi}, \end{aligned} \tag{5.14}$$

$$\begin{aligned} \partial_t \tilde{\gamma} &= \frac{4592}{375} + \frac{8768}{375}\tilde{\beta} + \frac{128}{15}\tilde{\beta}^2 \\ &+ \frac{1}{125}\tilde{\gamma} - \frac{79072}{1875}\tilde{\lambda}_{AD} - \frac{7936}{375}\tilde{\beta}\tilde{\lambda}_{AD} \\ &+ \frac{448}{125}\tilde{\gamma}\tilde{\lambda}_{AD} + \frac{74368}{1875}\tilde{\lambda}_{AD}^2 - \frac{5376}{625}\tilde{\lambda}_{AD}^3. \end{aligned} \tag{5.15}$$

We pointed out in the last Section that the appearance of bound states is connected with divergent vertex functions $\Gamma_k^{(n)}$ and we exploit this behavior to determine the bound state spectrum of the three- and four-boson system. At this point we must note that these infinities are complicated to handle in a numerical solution of the theory. In particular, the numerical treatment of unbounded limit cycles is problematic due to the periodic infinities during the RG flow. In order to circumvent this difficulty we used the method of inverse couplings. The basic idea is very simple. In the neighborhood of the resonances, where the flowing couplings diverge, we switch to the flow of inverse couplings which is regular and crosses zero at the resonances. After passing a resonance, we transform back to the flows of original couplings. Since the infinities occur periodically during the flow, we switch to inverse couplings whenever the absolute value of a given coupling exceeds some critical value.

The result of the numerical calculation of the four-body sector at unitarity is shown in Figure 5.3. Here, we display the RG flows of all three- and four-body couplings as a function of the RG scale $t = \ln(k/\Lambda)$. The three-body coupling $\tilde{\lambda}_{AD}$ (black dotted line) exhibits the limit cycle behavior, described

[3]For illustrative purpose we show the analytical form of the flow equations at the unitarity point only. Away from this limit their explicit expressions become much more complex.

in Section 5.3. Remarkably, there is an additional limit cycle in the flow of the four-body sector couplings with a periodic structure of exactly the same frequency as the three-body sector. This four-body sector limit cycle exhibits resonances which are shifted with respect to the ones of the three-body system. The magnitude of this shift is given by a new universal number, which is inherent to the four-body sector.

Our observation is that the four-body sector is intimately connected with the three-body sector at the unitarity point. It is permanently attached to the running of the three-body sector from the first three-body resonance on. From here on the periodic structure of the flow remains unchanged as one goes to smaller values of k. Due to this tight bond between the three- and four-body sector, there stays no room for an additional four-body parameter.

We also find that the magnitude of the shift beyond the first resonance is neither dependent on the initial values of the four-body sector couplings in the UV nor is it influenced by finite range corrections which we are able to check by choosing different values for the Yukawa coupling h. Arbitrary choices lead to the same behavior. Having done this calculation directly at the unitarity point our conclusion is, that, within our simple approximation, the four-body sector behaves truly universal and independent of any four-body parameter confirming the conjecture made by Platter et al. and von Stecher et al.. We expect that universality will also hold for an improved truncation.

Naively one expects that each resonance in the flow of the vertex functions is connected to the presence of a bound state. As one observes there are also additional resonances in the four-body sector being degenerate with the three-body sector resonances. However, we arrive at the conclusion that these resonances are artifacts of our approximation. The mathematical structure of the flow equations is of a kind that divergencies in the three-body sector directly lead to a divergent four-body sector. We believe that the resonances at these positions will disappear as one includes further momentum dependencies in the field theoretical model. Therefore we can already infer from the calculation at unitarity that within our approximation we are only able to resolve a single tetramer state attached to each trimer state also away from unitarity. In contrast, the "exact" quantum mechanical calculations in [107, 108, 109, 110] predict the existence of two tetramer states which have recently been observed by Ferlaino et al. [112] and Pollack et al. [69]. As one includes further momentum dependencies, it is well possible that not only the degenerate resonance disappears but also new, genuine resonances associated with the "missing" tetramer state will appear at the same time. This effect indeed occurs in the three-body problem. There, it is essential to include the momentum dependent two-atom vertex. Only under this condi-

tion one arrives at the quadratic equation as in (5.7) which gives rise to the Efimov effect. This can easily be seen by taking a look at the flow equation of λ_{AD} depicted as Feynman diagrams in Figure 5.2(b). The assumption of a momentum independent two-atom interaction corresponds to a momentum (and frequency) independent dimer propagator. In this approximation the first term on the RHS of Figure 5.2(b) vanishes because all poles of the loop frequency integration lie on the same complex frequency half-plane. This directly leads to the loss of the Efimov effect in this crude level of approximation.
We can also use our model to investigate the full bound state energy spectrum by solving the flow equations for arbitrary values of the scattering length a. The energy levels of the various bound states are then determined by varying the energy of the fundamental atoms E_ψ such that one finds a resonant four-body coupling in the IR. The result of this calculation is shown in Figure 5.1, where we plot the energy levels of the various bound states versus the inverse scattering length. We find one tetramer state attached to each of the Efimov trimer states. These tetramer states become degenerate with the four-atom threshold for negative scattering length and merge into the dimer-dimer threshold for positive a. In the experiment this leads to the measured resonance peaks in the four-body loss coefficient. In order not to overload the plot we show only the first three sets of levels, although the FRG method allows to calculate an arbitrary number of them. One also observes that the shape of the tetramer levels follows the shape of the trimer levels.

5.5 Summary

In this Chapter we investigated the four-body problem with the help of the functional renormalization group. Employing a simple two-channel model with pointlike three- and four-body interactions we were able to investigate universal properties at the unitarity point $a \to \infty$, $E_\psi = 0$ as well as to perform computations away from it.

In the RG language Efimov physics of the three-body problem manifests itself as an infinite RG limit cycle behavior of the three-body coupling constant at unitarity. We found that also the four-body sector is governed by such a limit cycle which is solely induced by the RG running of the three-body sector, signaling the absence of a four-body parameter.We also computed the energy spectrum away from unitarity.

Considering the simplicity of our model, the agreement with the previous studies in [107, 108, 109] is quite good. There had been some disagreement in literature about universality and the absence or existence of a four-body

parameter, see e.g. [115, 116, 117]. Our RG results support the conclusion that the four-body system is universal and independent of any four-body parameter.

An important shortcoming of the pointlike approximation is the absence of the shallower of the two tetramer states. Obviously the pointlike approximation of the three- and four-body sectors is not sufficient and in future work one should include momentum dependent interactions. From the energy spectrum in Figure 5.1 it becomes also evident that the excited tetramer states can decay into an energetically lower lying trimer plus atom. The higher excited states in the four-body system are therefore expected to have an intrinsic finite decay width [108]. Whether this width has a universal character still remains an open question as well as in which way the corresponding coupling constants, which become complex in this case, will change the RG analysis.

The four boson system remains still a subject with many open questions. With our RG analysis in the pointlike approximation, we made the first step towards a renormalization group description of the four-body problem supplementing the previous quantum mechanical approaches. From this perspective our work provides a starting point for a deeper understanding of universality in the four-body problem.

Chapter 6

Operators with Complex Scaling Dimensions

Relativistic conformal field theory is a well-developed subject with numerous applications in statistical physics (systems near a continuous phase transition) and high-energy physics. Recently, Nishida and Son made an important step towards systematic understanding of nonrelativistic conformal field theories (NRCFT) [43, 118][1] defined as invariant with respect to the Schrödinger symmetry [120, 121]. This symmetry contains the usual Galilei symmetry of nonrelativistic systems extended by a scale and special conformal transformation (some details can be found in Appendix B). The symmetry transformations form a group, called the Schrödinger group, which is a direct nonrelativistic analogue of the relativistic conformal group. As a simple example, the free nonrelativistic field theory has the Schrödinger symmetry. However, also a number of theories with interactions such as cold fermions at unitarity are believed to be invariant with respect to the Schrödinger symmetry, which provides powerful constraints on the correlation functions.

Similar to relativistic conformal field theories the basis of a NRCFT is formed by primary operators [43, 118]. A local primary operator $\mathcal{O}(t, \vec{x})$ has a well-defined scaling dimension $\Delta_{\mathcal{O}}$ and particle number $N_{\mathcal{O}}$

$$[D, \mathcal{O}] = i\Delta_{\mathcal{O}}\mathcal{O}, \qquad [N, \mathcal{O}] = N_{\mathcal{O}}\mathcal{O}, \tag{6.1}$$

where $\mathcal{O} \equiv \mathcal{O}(t = 0, \vec{x} = 0)$, D and N denote the generators of scale and particle number symmetry, respectively. In addition, the primary operator $\mathcal{O}$ must commute with the generators of Galilei boost K_i and the special conformal generator C

$$[K_i, \mathcal{O}] = 0, \qquad [C, \mathcal{O}] = 0. \tag{6.2}$$

[1] for an earlier work see [119]

The set of descendant operators constructed by subsequent application of time and spatial derivatives on the primary operator $\mathcal{O}$ form the irreducible representation of the Schrödinger algebra [43]. The scaling dimensions of descendants are related in a simple way to the scaling dimension of the parent primary operator $\mathcal{O}$.

As we demonstrated in Chapters 3 and 4, in some nonrelativistic theories the classical Schrödinger symmetry can be broken by a quantum scale anomaly [44]. This leads to discrete scale invariance and a geometric bound state energy spectrum [3, 70]. In previous Chapters of this thesis we discussed in detail how the anomaly also manifests itself in the renormalization group flow of a contact coupling which develops a limit cycle. Another signature of the nonrelativistic scale anomaly is the appearance of composite operators with complex scaling dimension. In this Chapter we concentrate on the latter and discuss some properties of composite operators with complex scaling dimension in a nonrelativistic quantum theory. In particular, we consider a two-particle problem in the quantum theory with an inverse square potential interaction. In this simple example we analytically compute the propagator of the s-wave composite operator $\mathcal{O} = \psi\psi$ and examine its structure. In this Chapter we do not use FRG, but employ resummation of Feynman diagrams in perturbation theory.

Similar to Chapter 3, here we consider the nonrelativistic quantum theory of identical bose particles interacting through a long-range inverse square potential $V(r) = -\frac{\kappa}{r^2}$ in D spatial dimensions.[2] The detailed discussion of quantum mechanics with inverse square potential was presented in Chapter 3. The corresponding nonrelativistic quantum field theory is defined by the microscopic (classical) action

$$\begin{aligned} S[\psi,\psi^*] = &\int dt \int d^D x \psi^*(t,\vec{x})[i\partial_t + \frac{\nabla^2_{\vec{x}}}{2}]\psi(t,\vec{x}) \\ &- \frac{1}{2}\int dt \int d^D x d^D y \psi^*(t,\vec{x})\psi^*(t,\vec{y})V(|\vec{x}-\vec{y}|)\psi(t,\vec{y})\psi(t,\vec{x}). \end{aligned} \tag{6.3}$$

In this Chapter the particle mass M_ψ and the reduced Planck constant $\hbar$ are set to unity.

The Feynman rules for the particle propagator $iG_\psi = \langle 0|T\psi\psi^\dagger|0\rangle$ and the

[2] In this Chapter we use field-theoretic (second-quantized) formulation of nonrelativistic quantum theory. In contrast to Chapter 3, here we employ the real-time formalism.

interaction vertex in momentum space are

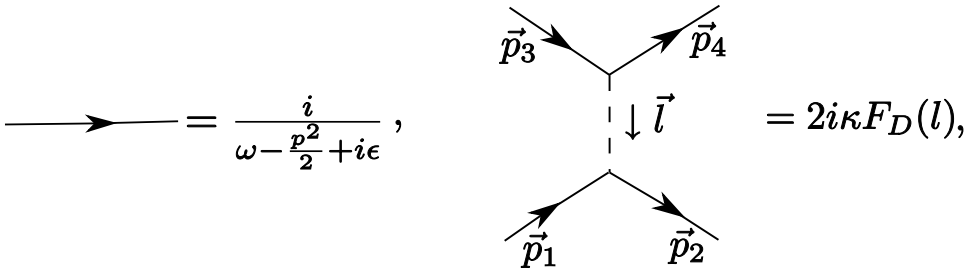

(6.4)

where $i\epsilon$ is an infinitesimal imaginary number, ensuring the retarded causal structure of the propagator. $\vec{l} = \vec{p}_2 - \vec{p}_1 = \vec{p}_3 - \vec{p}_4$ is the spatial momentum transfer during a collision ($l = |\vec{l}|$), and $F_D(l)$ denotes the Fourier transformation of the inverse square potential which in $D > 2$ reads

$$F_D(l) = \int d^D x \frac{1}{x^2} \exp[-i\vec{l} \cdot \vec{x}] = \frac{(4\pi)^{D/2}\Gamma(D/2-1)l^{2-D}}{4}. \tag{6.5}$$

In the rest of this Chapter we restrict our attention to spatial dimension $D > 2$.

6.1 Composite operator $\mathcal{O} = \psi\psi$

Consider a local two-particle s-wave operator $\mathcal{O}(t, \vec{x}) = \psi\psi(t, \vec{x})$ which annihilates two identical bose particles at the spacetime point $(t, \vec{x})$. As demonstrated in Appendix E, we can assign to the operator $\mathcal{O}$ a pair of scaling dimensions

$$\Delta_\pm = \frac{D+2}{2} \pm \sqrt{\frac{(D-2)^2}{4} - \kappa}. \tag{6.6}$$

The value of the interaction coupling κ determines two qualitatively different regimes:

- **Undercritical regime** $\kappa < \kappa_{cr} = \frac{(D-2)^2}{4}$: Both Δ_+ and Δ_- are real and the action (6.3) defines two conformal quantum field theories CFT_+ and CFT_-. As demonstrated in Chapter 3, the quantum field theory defined by the classical action (6.3) flows towards CFT_+ in the infrared and towards CFT_- in the ultraviolet in the renormalization group sense. To obtain the action of CFT_+ (CFT_-), we must add to the inverse square potential a delta function localized at the origin

$$V(r) \to -\frac{\kappa}{r^2} - \frac{\lambda}{\epsilon}\delta(r) \tag{6.7}$$

and fine-tune the value of the dimensionless contact coupling λ to the infrared (ultraviolet) fixed point. The operator $\mathcal{O}$ is a nonrelativistic two-particle primary operator because it is a local product of two primary operators ψ.

- **Overcritical regime** $\kappa > \kappa_{cr}$: The quantum field theory ceases to be conformal and renormalization group evolution of the coupling λ in Eq. (6.7) develops a limit cycle. $\Delta_\pm$ in Eq. (6.6) becomes complex and form a conjugate pair. Due to the loss of conformality $\Delta_\pm$ do not fulfill the definition for scaling dimension as given in Eq. (6.1). However, we will still use the term scaling dimensions for $\Delta_\pm$ even in the overcritical regime. This is motivated by observation made in Chapter 3 that one can formally extend parameter space of the contact coupling λ to the complex plane. In this extension two complex fixed points emerge in the overcritical regime. At these fixed points the operator $\mathcal{O}$ has scaling dimensions $\Delta_\pm$ in the sense of Eq. (6.1).

We now calculate the two-point function (two-particle propagator)

$$iG_{\mathcal{O}}(t_2, \vec{x}_2; t_1, \vec{x}_1) = \langle 0|T\mathcal{O}(t_2, \vec{x}_2)\mathcal{O}^\dagger(t_1, \vec{x}_1)|0\rangle \tag{6.8}$$

in the overcritical regime $\kappa > \kappa_{cr}$. Intuitively, the two-point function is proportional to the probability of creating two identical particles at the space-time point $(t_1, \vec{x}_1)$ and subsequent destruction of the pair at the distinct point $(t_2, \vec{x}_2)$.

The translational invariance of the action (6.3) allows us to transform $iG_{\mathcal{O}}$ to the momentum space

$$iG_{\mathcal{O}}(\omega, \vec{p}) = \int dt d^D x e^{i\omega t - i\vec{p}\cdot\vec{x}} iG_{\mathcal{O}}(t, \vec{x}; 0, \vec{0}). \tag{6.9}$$

The diagramatic expression of the propagator $iG_{\mathcal{O}}(\omega, \vec{p})$ is depicted in Figure 6.1. The first diagram in Figure 6.1 corresponds to a free propagation of two particles, while the remaining sum of diagrams takes into account the influence of the long-range interaction.

We remind that few-body problems in nonrelativistic quantum field theory are relatively simple because only particles (but no antiparticles) exist as excitations of the nonrelativistic vacuum.[3] This remarkable fact and the particle number conservation lead to the important diagrammatic simplification: *Any loop with line arrows pointing in the same direction vanishes.* For a detailed discussion of this important observation see Chapter 4.

[3]From this perspective, many-body problems are more difficult due to a more complicated vacuum state which allows the presence of hole excitations.

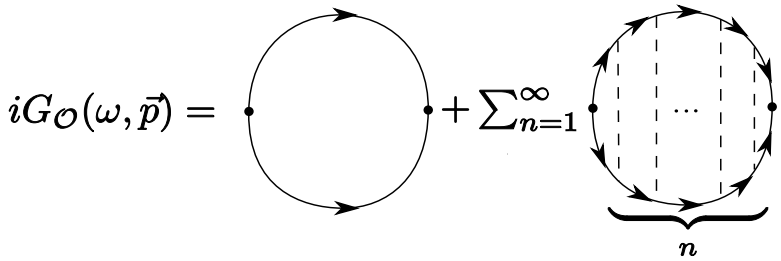

Figure 6.1: The two-particle propagator $iG_{\mathcal{O}}(\omega,\vec{p})$ illustrated as a sum of Feynman diagrams. The full circles denote the composite operator insertions.

In our specific problem the diagrammatic simplification has a number of important consequences:

- The particle propagator is not renormalized and coincides with the bare propagator depicted in Eq. (6.4). For this reason there are only bare propagators in Figure 6.1.
- The long-range interaction vertex is not renormalized (i.e. there is no screening). That is why there are only bare vertices in Figure 6.1.
- There are no "crossed" interaction lines in Figure 6.1.

We note that due to the Galilean symmetry of the action (6.3), the two-particle propagator $iG_{\mathcal{O}}(\omega,\vec{p})$ should be a function of only the Galilean invariant combination $\omega-\vec{p}^2/4$. Hence, it is advantageous to switch to the center-of-mass frame (i.e. set $\vec{p}=0$) first and calculate $iG_{\mathcal{O}}(\omega)\equiv iG_{\mathcal{O}}(\omega,\vec{p}=0)$. In the very end we can recover momentum dependence by the substitution $iG_{\mathcal{O}}(\omega)\to iG_{\mathcal{O}}(\omega-\vec{p}^2/4)$.

Separation of relative and center-of-mass motion in the two-body problem allows us to relate the two-particle propagator $iG_{\mathcal{O}}(\omega)$ to the energy Green function $G_D(\vec{r}\,'',\vec{r}\,';\omega)$ of a single particle with the reduced mass $M_{red}=\frac{M_\psi}{2}=\frac{1}{2}$ in the external inverse square potential. To clarify this point, consider the first diagram in Figure 6.1, which we shall call $iG^0_{\mathcal{O}}(\omega)$

$$\begin{aligned} iG^0_{\mathcal{O}}(\omega) &= \int_{\vec{l}}\int \frac{dl_0}{2\pi}\frac{i}{l_0-\frac{l^2}{2}+i\epsilon}\frac{i}{\omega-l_0-\frac{l^2}{2}+i\epsilon} = \int_{\vec{l}}\int_{\vec{l}\,'}\frac{i}{\omega-l^2+i\epsilon}\delta(\vec{l}-\vec{l}\,') \\ &= i\langle\vec{r}\,''=0|(\omega-\hat{p}^2+i\epsilon)^{-1}|\vec{r}\,'=0\rangle = iG^0_D(\vec{r}\,''=0,\vec{r}\,'=0;\omega), \end{aligned} \tag{6.10}$$

where $\int_{\vec{l}}=\int\frac{d^Dl}{(2\pi)^D}$. In the first line we performed frequency loop integration. In the last line the definition of the energy Green function $G^0_D(\vec{r}\,'',\vec{r}\,';\omega)$

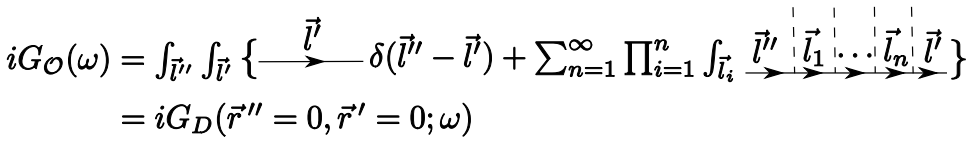

Figure 6.2: The relation between the two-particle propagator $iG_{\mathcal{O}}(\omega)$ and the energy Green function $G_D(\vec{r}\,'', \vec{r}\,'; \omega)$. Full lines with an arrow denote here the bare propagator of a particle of the reduced mass $M_{red} = \frac{1}{2}$.

evaluated at the origin $\vec{r}\,'' = \vec{r}\,' = 0$ was recognized. In the same way, we can perform frequency loop integrations in the diagrams with interaction vertices in Figure 6.1 and find that

$$iG_{\mathcal{O}}(\omega) = i\langle \vec{r}\,'' = 0|(\omega - \hat{H} + i\epsilon)^{-1}|\vec{r}\,' = 0\rangle = iG_D(\vec{r}\,'' = 0, \vec{r}\,' = 0; \omega), \quad (6.11)$$

where $\hat{H} = \hat{p}^2 - \frac{\kappa}{\hat{r}^2}$. In terms of Feynman diagrams the last relation can be expressed as depicted in Figure 6.2. The energy Green function $G_D(\vec{r}\,'', \vec{r}\,'; \omega)$ for the inverse square potential problem was calculated in [122], and a modified derivation is presented in the next Section.

6.2 Energy Green function $G_D(\vec{r}\,'', \vec{r}\,'; \omega)$

The energy Green function in position representation in D spatial dimensions is given by

$$G_D(\vec{r}\,'', \vec{r}\,'; \omega) = \langle \vec{r}\,''|(\omega - \hat{H} + i\epsilon)^{-1}|\vec{r}\,'\rangle, \quad (6.12)$$

where $\hat{H} = \hat{p}^2 + V(\hat{\vec{r}})$ is a single particle Hamiltonian. The definition (6.12) leads to the following inhomogeneous differential equation

$$\left[\nabla^2_{\vec{r}\,''} + \omega - V(\vec{r}\,'')\right] G_D(\vec{r}\,'', \vec{r}\,'; \omega) = \delta(\vec{r}\,'' - \vec{r}\,'). \quad (6.13)$$

For a central potential Eq. (6.13) can be solved by separation of variables. In particular, the energy Green function can be expanded in D-dimensional partial waves

$$G_D(\vec{r}\,'', \vec{r}\,'; \omega) = (r\,'' r\,')^{-\frac{D-1}{2}} \sum_{l=0}^{\infty} \sum_{m=1}^{d_l} Y_{lm}(\Omega\,'') Y^*_{lm}(\Omega\,') G_l(r\,'', r\,'; \omega), \quad (6.14)$$

where $Y_{lm}(\Omega)$ denote D-dimensional spherical harmonics and $d_l = \frac{(2l+D-2)(l+D-3)!}{l!(D-2)!}$.[4] Substitution of Eq. (6.14) in Eq. (6.13) gives the differential equation for

[4] We use the notation from [122] for the labelling of spherical harmonics in D dimensions.

the radial energy Green function

$$\left[\frac{d^2}{dr''^2}+\omega-V(r'')-\frac{(l+\nu)^2-\frac{1}{4}}{r''^2}\right]G_l(r'',r';\omega)=\delta(r''-r') \tag{6.15}$$

with $\nu=\frac{D-2}{2}$. Solution of this equation is now a textbook problem (see e.g. [123]). The radial energy Green function can be expressed as

$$G_l(r'',r';\omega)=\frac{u_l^{(<)}(r_<)u_l^{(>)}(r_>)}{W\{u_l^{(<)},u_l^{(>)}\}(r')} \tag{6.16}$$

with $r_<$ (resp. $r_>$) denoting the smaller (resp. larger) one of r' and r''. $W\{u_l^{(<)},u_l^{(>)}\}$ represents the Wronskian of $u_l^<$ and $u_l^>$, i.e.

$$W\{u_l^{(<)},u_l^{(>)}\}=u_l^{(<)}u_l^{(>)\prime}-u_l^{(<)\prime}u_l^{(>)}. \tag{6.17}$$

The function $u_l^{(<)}$ (resp. $u_l^{(>)}$) solves the homogeneous differential equation

$$\left[\frac{d^2}{dr^2}+\omega-V(r)-\frac{(l+\nu)^2-\frac{1}{4}}{r^2}\right]u_l(r)=0 \tag{6.18}$$

with a regular boundary condition at $r=0$ (resp. $r=\infty$).

Consider now the inverse square potential $V(r)=-\frac{\kappa}{r^2}$. Depending on the value of the coupling strength κ, the solution of Eq. (6.18) has two qualitatively different branches. We analyze these two regimes separately.

Undercritical regime $\kappa<(l+\nu)^2$

Two linearly independent solutions of Eq. (6.18) are

$$u_l(r)=\{\sqrt{r}I_{s_l}(\zeta r),\sqrt{r}K_{s_l}(\zeta r)\} \tag{6.19}$$

with $\zeta=\sqrt{-\omega-i\epsilon}$ and $s_l=\sqrt{(l+\nu)^2-\kappa}$. I_{s_l} and K_{s_l} denote modified Bessel functions. We find

$$\begin{aligned} &u_l^{(>)}(r)\sim\sqrt{r}K_{s_l}(\zeta r), \qquad && u_l^{(>)}(r)\overset{r\to\infty}{\longrightarrow}0,\\ &u_l^{(<)}(r)\sim\sqrt{r}I_{s_l}(\zeta r), && u_l^{(<)}(r)\overset{r\to 0}{\longrightarrow}0. \end{aligned} \tag{6.20}$$

Substitution of Eq. (6.20) in Eq. (6.16) yields the radial Green function

$$G_l(r'',r';\omega)=-\sqrt{r''r'}I_{s_l}(\zeta r_<)K_{s_l}(\zeta r_>). \tag{6.21}$$

Overcritical regime $\kappa > (l+\nu)^2$

In this case two linearly independent solutions of Eq. (6.18) are found to be

$$u_l(r) = \{\sqrt{r} I_{i\theta_l}(\zeta r), \sqrt{r} K_{i\theta_l}(\zeta r)\} \tag{6.22}$$

with $\theta = \sqrt{\kappa - (l+\nu)^2}$. It is straightforward to determine $u_l^{(>)}$, which is

$$u_l^{(>)}(r) \sim \sqrt{r} K_{i\theta_l}(\zeta r), \qquad u_l^{(>)}(r) \overset{r\to\infty}{\longrightarrow} 0. \tag{6.23}$$

On the other hand, determination of $u_l^{(<)}(r)$ turns out to be more subtle. It is easily demonstrated that any linear combination of two independent solutions (6.22) approaches zero as $r \to 0$, and thus satisfies the regular boundary condition. Mathematically, the problem originates from the singular behavior of the inverse square potential at $r = 0$. In the overcritical regime the potential is too singular and must be regularized. Regularization, introduced in [122], imposes the boundary condition at some small but finite $r = a$. Here, following [34], we use a different but equivalent regularization procedure which consists in fixing a phase angle of $u_l^{(<)}(r)$ as $r \to 0$. Specifically, we take the function $u_l^{(<)}(r)$ to be

$$u_l^{(<)}(r) \sim \sqrt{r} \left[e^{i\eta(\zeta)} I_{i\theta_l}(\zeta r) + e^{-i\eta(\zeta)} I_{-i\theta_l}(\zeta r) \right] \tag{6.24}$$

with $\eta(\zeta) = -\theta_l \ln\left(\frac{\zeta}{\zeta_l^*}\right)$. Here we introduced a momentum scale ζ_l^* that determines the phase shift of $u_l^{(<)}(r)$ near the origin

$$u_l^{(<)}(r) \sim \sqrt{r} \cos(\theta_l \ln r + \beta + \underbrace{\theta_l \ln \zeta_l^*}_{\delta_l \phi}), \tag{6.25}$$

where $\beta = \arg\left(\frac{2^{-i\theta_l}}{\Gamma(1+i\theta_l)}\right)$. We emphasize that the phase shift $\delta_l\phi$ is a physical parameter that fixes $u_l^{(<)}(r)$ in the unique way (up to normalization). Substitution of Eqs. (6.23, 6.25) in Eq. (6.16) yields the radial energy Green function

$$G_l(r'', r'; \omega) = -\frac{\sqrt{r'' r'} \left[e^{i\eta(\zeta)} I_{i\theta_l}(\zeta r_<) + e^{-i\eta(\zeta)} I_{-i\theta_l}(\zeta r_<) \right] K_{i\theta_l}(\zeta r_>)}{2\cos\left(\theta_l \ln(\zeta/\zeta_l^*)\right)}. \tag{6.26}$$

6.3 Two-particle propagator $iG_{\mathcal{O}}$

We are now in the position to finish the calculation of the two-particle propagator $iG_{\mathcal{O}}(\omega)$ in the overcritical (anamalous) regime. To this end, according

to Eq. (6.11) one must evaluate the energy Green function $G_D(\vec{r}\,'', \vec{r}\,'; \omega)$ at $\vec{r}\,'' = \vec{r}\,' = 0$. Inspection of Eqs. (6.14,6.26) reveals, however, that for $D > 2$ this leads to a divergent result. The finite propagator is obtained for the renormalized composite $\mathcal{O}^{ren} \equiv r^{\frac{D-2}{2}}\mathcal{O}$. It reads

$$iG_{\mathcal{O}^{ren}}(\omega) = \langle 0|T\mathcal{O}^{ren}\mathcal{O}^{\dagger\, ren}|0\rangle = i\lim_{r\to 0} r^{D-2}\int \frac{d\Omega\,'}{S^{D-1}}\int \frac{d\Omega\,''}{S^{D-1}} G_D(\vec{r}\,'', \vec{r}\,'; \omega)\Big|_{r\,''=r\,'=r}, \tag{6.27}$$

where $S^{D-1} = 2\frac{\pi^{D/2}}{\Gamma(D/2)}$. In the last expression we introduced two angular integration averages that should be performed before the radial limit. This ensures the final result to be independent of the directions of $\vec{r}\,'$ and $\vec{r}\,''$. We now substitute the partial wave expansion (6.14) in Eq. (6.27) and obtain

$$iG_{\mathcal{O}^{ren}}(\omega) = -i\lim_{r\to 0} \frac{\left[e^{i\eta(\zeta)}I_{i\theta_0}(\zeta r) + e^{-i\eta(\zeta)}I_{-i\theta_0}(\zeta r)\right] K_{i\theta_0}(\zeta r)}{2\cos\left(\theta_0 \ln(\zeta/\zeta_0^*)\right)}, \tag{6.28}$$

where only the s-wave ($l = 0$) survives the angular integrations. Finally, we perform the limit $r \to 0$ and find

$$iG_{\mathcal{O}}^{ren}(\omega) = i\tan\left(\theta_0 \ln\frac{\sqrt{-\omega - i\epsilon}}{\zeta_0^*}\right), \tag{6.29}$$

where computational details and the explicit definition of the renormalized two-particle propagator $iG_{\mathcal{O}}^{ren}(\omega)$ can be found in Appendix B of [124].

Our final result (6.29) is remarkably simple and has the following properties:

- For negative energies $\omega < 0$ the two-particle propagator $iG_{\mathcal{O}}^{ren}(\omega)$ has an infinite number of simple pole divergences at

$$\omega_n = -\zeta_0^{*2}\exp\left(-\frac{2\pi n}{\theta_0} + \frac{\pi}{\theta_0}\right), \quad n \in \mathbb{Z}. \tag{6.30}$$

  Hence, the composite field $\mathcal{O}^\dagger$ represents infinitely many different stable particles (two-particle s-wave bound states). The energy spectrum has an accumulation point at $\omega \to 0$ as $n \to \infty$. It exhibits geometric behavior

$$\frac{\omega_{n+1}}{\omega_n} = \exp\left(-\frac{2\pi}{\theta_0}\right). \tag{6.31}$$

  For positive energies $\omega > 0$ the two-point correlation function $iG_{\mathcal{O}}^{ren}(\omega)$ has a branch cut with a branch point at $\omega = 0$.

- The regularization momentum scale ζ_0^* introduced in Section 6.2 is a physical parameter of the theory. It determines the value of the reference (for example $n = 0$) two-particle bound state energy

$$\omega_0 = -\zeta_0^{*2} \exp\left(\frac{\pi}{\theta_0}\right). \tag{6.32}$$

- The propagator $iG_{\mathcal{O}}^{ren}(\omega)$ is invariant under the discrete scaling symmetry

$$\zeta_0^* \to \zeta_0^* \exp\left(\frac{\pi m}{\theta_0}\right), \quad m \in \mathbb{Z}. \tag{6.33}$$

  This transformation maps $\omega_n \to \omega_{n+m}$, but does not alter the energy spectrum. Physically inequivalent ζ_0^* may thus be chosen to lay within the interval $\zeta_0^* \in [1, \exp\left(\frac{\pi}{\theta_0}\right))$. This supports our observation in Section 6.2 that ζ_0^* determines the phase shift angle $\delta_0\phi = \theta_0 \ln \zeta_0^*$ of the wave function near the origin. We conclude that physically inequivalent phase shifts $\delta_0\phi$ span the interval $[0, \pi)$.

- Finally, as advocated in Section 6.1, the Galilean symmetry allows us to recover the momentum dependence of the two-particle propagator

$$iG_{\mathcal{O}}^{ren}(\omega, \vec{p}) = i \tan\left(\theta_0 \ln \frac{\sqrt{-\omega + \frac{\vec{p}^2}{4} - i\epsilon}}{\zeta_0^*}\right). \tag{6.34}$$

In the rest of this Section we attempt to compute the two-particle propagator in the position space. This can be achieved via the inverse Fourier transformation of Eq. (6.34)

$$iG_{\mathcal{O}}^{ren}(t, \vec{x}) = \int \frac{d\omega}{2\pi} \frac{d^D p}{(2\pi)^D} e^{-i\omega t + i\vec{p}\cdot\vec{x}} i \tan\left(\theta_0 \ln \frac{\sqrt{-\omega + \frac{\vec{p}^2}{4} - i\epsilon}}{\zeta_0^*}\right). \tag{6.35}$$

First we perform the angular integration and obtain

$$\begin{aligned} iG_{\mathcal{O}}^{ren}(t, \vec{x}) = \left(\frac{1}{2\pi}\right)^{D/2} \int_0^\infty dp p \left(\frac{p}{x}\right)^{D/2-1} J_{D/2-1}(px) \times \\ \int \frac{d\omega}{2\pi} e^{-i\omega t} i \tan\left(\theta_0 \ln \frac{\sqrt{-\omega + \frac{p^2}{4} - i\epsilon}}{\zeta_0^*}\right). \end{aligned} \tag{6.36}$$

Now we introduce a new variable $W \equiv -\omega + \frac{p^2}{4}$ and get

$$iG^{ren}_{\mathcal{O}}(t,\vec{x}) = \left(\frac{1}{2\pi}\right)^{D/2} \int_0^\infty dpp \left(\frac{p}{x}\right)^{D/2-1} J_{D/2-1}(px) e^{-i\frac{p^2}{4}t} \times \int \frac{dW}{2\pi} e^{iWt} i \tan\left(\theta_0 \ln \frac{\sqrt{W-i\epsilon}}{\zeta_0^*}\right). \tag{6.37}$$

Finally, the momentum integral can be done analytically with the result

$$iG^{ren}_{\mathcal{O}}(t,\vec{x}) = \left(\frac{-i}{\pi t}\right)^{D/2} \exp\left(-iN_{\mathcal{O}}\frac{\vec{x}^2}{2t}\right) \mathcal{S}(t), \tag{6.38}$$

where $N_{\mathcal{O}} = -2$ and $\mathcal{S}(t) = \int \frac{dW}{2\pi} e^{iWt} i \tan\left(\theta_0 \ln \frac{\sqrt{W-i\epsilon}}{\zeta_0^*}\right)$. We were not able to perform the integral over W explicitly. Based on the dimensional argument $\mathcal{S}(t) = t^{-1} f\left((\zeta_0^*)^2 t, \theta_0\right)$, where f is some function of the dimensionless arguments $(\zeta_0^*)^2 t$ and θ_0. We checked that the function $\mathcal{S}(t)$ is not restricted by the Galilean symmetry.

6.4 Composite operators $\mathcal{O}^{(l)}$ with higher angular momentum

The energy Green function (6.12) contains also information about the two-particle composite operators $\mathcal{O}^{(l)}$ which carry the higher angular momentum l. In the conformal regime, these operators are nonrelativistic primaries of [43]. The p-wave and d-wave operators in a theory with a one-component bose field ψ are explicitly given by

$$\mathcal{O}_i^{(l=1)} = \nabla_i\psi\psi - \psi\nabla_i\psi, \tag{6.39}$$

$$\mathcal{O}_{ij}^{(l=2)} = [\psi\nabla_i\nabla_j\psi - \nabla_i\psi\nabla_j\psi] - \frac{\delta_{ij}}{D}[\psi\Delta\psi - \nabla_k\psi\nabla_k\psi] \tag{6.40}$$

Up to normalization these operators are fixed by two requirements. First, they must be constructed from only two elementary fields ψ and spatial gradients. Second, they are nonrelativistic primaries of ref. [43] and satisfy Eqs. (6.1, 6.2). We expect that in a similar fashion the two-particle primaries with $l > 2$ can be constructed. It is clear from Eq. (6.39) that in the bosonic theory (6.3) the p-wave operator $\mathcal{O}_i^{(l=1)}$ vanishes, as well as all primary operators with odd angular momentum. The d-wave operator $\mathcal{O}_{ij}^{(l=2)}$ is a symmetric, traceless tensor.[5]

[5] In order to make the tensor traceless, one subtracts in Eq. (6.40) the s-wave part $\mathcal{O}_s = \psi\Delta\psi - \nabla_k\psi\nabla_k\psi$. It is instructive to express this operator as $\mathcal{O}_s = -\frac{1}{2}\nabla_k\nabla_k\mathcal{O} -$

The scaling dimensions of the composites $\mathcal{O}^{(l)}$ were computed in Appendix E and are given by

$$\Delta_{\pm}^{(l)} = \frac{D+2}{2} \pm \sqrt{\left(l + \frac{D-2}{2}\right)^2 - \kappa}. \tag{6.41}$$

They become complex for $\kappa > \left(l + \frac{D-2}{2}\right)^2$.

The two-particle propagator $iG_{\mathcal{O}^{(l)}} = \langle 0|T\mathcal{O}^{(l)}\mathcal{O}^{(l)\dagger}|0\rangle$ can be extracted from the l^{th} partial wave of the energy Green function, i.e. it is encoded in the radial Green function $G_l(r'', r'; \omega)$. Following closely the steps from Section 6.3, in the overcritical regime we obtain for the renormalized propagator

$$iG^{ren}_{\mathcal{O}^{(l)}}(\omega, \vec{p}) = i \tan\left(\theta_l \ln \frac{\sqrt{-\omega + \frac{\vec{p}^2}{4} - i\epsilon}}{\zeta_l^*}\right) T_{i_1 \ldots i_l, j_1 \ldots j_l}(\vec{p}), \tag{6.42}$$

where $T_{i_1 \ldots i_l, j_1 \ldots j_l}$ is a tensor symmetric and traceless in the indices $i_1 \ldots i_l$ and $j_i \ldots j_l$. This tensor does not depend on the energy ω, and thus we can extract the energies of the two-particle bound states with angular momentum l from Eq. (6.42). Similar to the s-wave bound states, for even angular momenta l the energy spectrum exhibits geometric behavior

$$\frac{\omega_{n+1}}{\omega_n} = \exp\left(-\frac{2\pi}{\theta_l}\right). \tag{6.43}$$

6.5 Summary

In this Chapter we examined composite operators in a nonrelativistic quantum field theory. In general, the presence of such operators is a signature of the quantum scale anomaly. As a concrete example, we considered quantum mechanics with the classically scale invariant inverse square potential and studied the two-particle local scalar composite operator $\mathcal{O} = \psi\psi$. We determined the complex scaling dimension of this operator and analytically calculated the two-particle propagator $\langle 0|T\mathcal{O}\mathcal{O}^\dagger|0\rangle$. In the nonconformal (anomalous) regime the operator $\mathcal{O}$ represents an infinite tower of s-wave two-particle bound states which form a geometric energy spectrum.

For simplicity, we considered the specific two-particle inverse square potential problem, which is the paradigmatic example of a nonrelativistic theory with the quantum scale anomaly. Nevertheless, we expect that our simple

$2i\partial_t\mathcal{O} + 4\psi\left(i\partial_t + \frac{\Delta}{2}\right)\psi$, where the first and the second terms are the descendants of the primary $\mathcal{O}$ and the third term is a primary operator.

result (6.34) for the two-point correlator $\langle 0|T\mathcal{O}\mathcal{O}^\dagger|0\rangle$ is universal and applies to other more complicated nonrelativistic theories containing composite operators with complex scaling dimensions. One prominent example, discussed in detail in Chapters 4 and 5, is a system of three identical bosons interacting through a contact potential tuned to the unitarity point. Due to the Efimov effect [3], the local atom-dimer composite operator $\mathcal{O} = \psi\phi$ acquires the complex scaling dimensions

$$\Delta_\pm = \frac{5}{2} \pm i s_0, \tag{6.44}$$

where the Efimov parameter $s_0 \approx 1.00624$. A similar system that exhibits the quantum scale anomaly in the three-particle sector is the two-component fermionic system with unequal masses [3]. Another interesting example is the one-dimensional model with a four-body resonant interaction [125] where the scaling dimension of the five-boson composite operator is complex, too.

Recently we used the method of the nonrelativistic AdS/CFT correspondence to study operators with complex scaling dimensions [51]. Using the standard AdS/CFT technique, we calculated the two-point correlation function $\langle 0|\mathcal{O}\mathcal{O}^\dagger|0\rangle$. The result has the same functional form as found in this work in Eq. (6.34). However, while Eq. (6.34) depends on the physical momentum parameter ζ_0^*, the holographic result of [51] depends on the value of the UV momentum cutoff. The latter is unphysical, and we expect that the cutoff dependence in the AdS/CFT calculation can be eliminated by inclusion of a proper boundary counterterms.

Chapter 7

Conclusions

During the recent years nonrelativistic few-body physics has experienced a revived interest and undergone a considerable progress. A wealth of experiments with ultracold atomic gases together with a significant theoretical effort initiated a birth of a new exciting field known as Efimov physics. In this thesis we studied various aspects of the Efimov effect with the method of functional renormalization.

Chapter 2 was devoted to a short introduction to the method of functional renormalization. We introduced the Wetterich flow equation, discussed few aspects of the technique and illustrated how the method works in practice using a simple example of a zero-dimensional field theory.

The problem of a singular, inverse square potential in nonrelativistic quantum mechanics was treated in Chapter 3. This problem is in the very core of Efimov physics and its solution is crucial for developing a proper physical understanding. We observed that the emergent contact coupling flows to a fixed point or develops a limit cycle depending on the discriminant of its quadratic beta function. We analyzed the fixed points in both conformal and nonconformal phases and performed a natural extension of the renormalization group analysis to complex values of the running coupling. Physical interpretation and motivation for this extension is the presence of an inelastic scattering channel in two-body collisions. We presented the geometric description of the complex generalization by considering renormalization group flows on the Riemann sphere. Finally, using bosonization, we found the compact analytical solution of the extended renormalization group flow equations.

Subsequently, in Chapter 4 we applied the functional renormalization group technique to the few-body problem of nonrelativistic atoms near a Feshbach resonance. Three systems were considered: one-component bosons with the $U(1)$ symmetry, two-component fermions with the $U(1) \times SU(2)$

symmetry and three-component fermions with the $U(1) \times SU(3)$ symmetry. We focused on the scale invariant unitarity limit of an infinite scattering length. The exact solution of the two-body problem was constructed and it turned out to be consistent with the unitary fixed point behavior of the three considered systems. Nevertheless, we observed that the solution of the original Efimov three-body problem develops a limit cycle scaling in case of $U(1)$ bosons and $SU(3)$ fermions. The Efimov parameter was determined from the period of the limit cycle. It was found to be $s \approx 1.006$ consistent with the quantum-mechanical result.

In Chapter 5 we performed the first step towards the renormalization group analysis of the nonrelativistic four-boson problem by means of a simple model with pointlike three- and four-body interactions. In particular, we investigated the region where the scattering length is infinite and all energies are close to the atom threshold. We found that the four-body problem behaves truly universally, independently of any four-body parameter. Our findings confirm the recent conjectures of Platter et al. [107, 108] and von Stecher et al. [109] that the four-body problem is universal, now also from a renormalization group perspective.

Finally, in Chapter 6 it was demonstrated that in the language of quantum field theory Efimov physics manifests itself in the appearance of composite operators with complex scaling dimensions. In particular, we studied the paradigmatic example of nonrelativistic quantum mechanics with the inverse square potential and considered a composite s-wave operator $\mathcal{O} = \psi\psi$. We computed analytically the scaling dimension of this operator and determined the propagator $\langle 0|T\mathcal{O}\mathcal{O}^\dagger|0\rangle$. We found that the operator $\mathcal{O}$ represents an infinite tower of bound states with a geometric energy spectrum. Operators with higher angular momenta were also briefly discussed.

We conclude that the functional renormalization is a very powerful method for the investigation of few-body nonrelativistic physics and of the Efimov effect in particular. It allows to address few-body problems from a different angle and provides an interesting alternative to the standard quantum-mechanical and effective field theory treatments. Noteworthy, the method is not limited to few-body problems and is widely used for studying various many-body phenomena in condensed matter physics.

There is a number of interesting questions related to Efimov physics which we intend to address in future with functional renormalization:

- In the three-body problem one can go away from unitarity and determine universal properties of the system such as recombination rates, positions where Efimov trimers merge with scattering thresholds, etc. First steps in this direction with FRG were done in [85, 93, 86]. One can

also study nonuniversal features such as the effective range corrections (see Appendix D).

- Our investigation in Chapter 5 is just the starting point for a complete renormalization group treatment of the four-body problem. In the original Efimov three-body problem the introduction of the dynamical dimer field is a decisive step towards the correct solution. From this perspective, in the four-body problem it seems important to introduce the Efimov trimer states directly into the model as a dynamical field. The trimer field has a complex scaling dimension and its propagator has a similar structure as the propagator obtained in Chapter 6. The FRG treatment of the model with the dynamical trimer field offers itself as a natural next step towards the complete solution.

- It is a very interesting question to study a transition between few-body to many-body physics by approximately solving five-, six- and higher-body problems in the universal regime. This has been recently addressed in [126] with the help of variational quantum-mechanical methods. Since the complexity grows substantially with the increasing number of particles, for a proper FRG treatment of this intriguing question efficient approximation schemes must first be developed.

Appendix A

$Z(j)$ in zero-dimensional field theory

Theorem: The integral $Z(j) = \int_{-\infty}^{\infty} dx e^{-S(x)+jx}$ with

- $S(x) \in \mathbb{R}$ and bounded from below
- $S(x) > 0$ for $|x| \to \infty$
- $\frac{x^2}{S(x)} < \infty$ as $|x| \to \infty$

is smooth (differentiable), i.e. $\frac{d^n Z}{dj^n}$ exists for any $n \in \mathbb{N}$ and $j \in \mathbb{R}$.
Proof: It is sufficient to demonstrate that

$$\lim_{\epsilon \to 0} \left(\frac{d^n Z}{dj^n}\Big|_{j+\epsilon} - \frac{d^n Z}{dj^n}\Big|_{j-\epsilon} \right) = 0, \tag{A.1}$$

i.e. that the right and the left derivatives coincide for any $n \in \mathbb{N}$ and $j \in \mathbb{R}$. To achieve this goal, we explicitly evaluate the difference (A.1)

$$\begin{aligned} \lim_{\epsilon \to 0} \left(\frac{d^n Z}{dj^n}\Big|_{j+\epsilon} - \frac{d^n Z}{dj^n}\Big|_{j-\epsilon} \right) &= \lim_{\epsilon \to 0} \int_{-\infty}^{\infty} dx x^n e^{-S(x)+jx} \left(e^{\epsilon x} - e^{-\epsilon x} \right) \\ &= \lim_{\epsilon \to 0} 2\epsilon \underbrace{\int_{-\infty}^{\infty} dx x^{n+1} e^{-S(x)+jx}}_{\text{bounded}} = 0, \end{aligned} \tag{A.2}$$

where we used $(e^{\epsilon x} - e^{-\epsilon x}) \approx 2\epsilon x$ and the integral $\int dx x^{n+1} e^{-S(x)+jx}$ is bounded for any $n \in \mathbb{N}$ and $j \in \mathbb{R}$ if the assumptions of the theorem are fulfilled. This concludes the proof.
Corollary: Under the assumptions of the above theorem the Schwinger function $W(j) = \ln Z(j)$ is smooth.

Appendix B

Galilean and nonrelativistic conformal symmetry

All systems considered in this thesis have a centrally extended Galilean spacetime symmetry.[1] The centrally extended Galilean algebra in a three-dimensional flat space consists of eleven generators: particle number N (central charge), time translation H, three spatial translations P_i, three spatial rotations M_{ij} and three Galilean boosts K_i. The nontrivial commutators are (in the real time formalism)

$$[M_{ij}, M_{kl}] = i(\delta_{ik}M_{jl} - \delta_{jk}M_{il} + \delta_{il}M_{kj} - \delta_{jl}M_{ki}), \tag{B.1}$$

$$[M_{ij}, K_k] = i(\delta_{ik}K_j - \delta_{jk}K_i), \qquad [M_{ij}, P_k] = i(\delta_{ik}P_j - \delta_{jk}P_i), \tag{B.2}$$

$$[P_i, K_j] = -i\delta_{ij}N, \qquad [H, K_j] = -iP_j. \tag{B.3}$$

In the case of a free nonrelativistic field theory the group of spacetime symmetries is in fact larger than the Galilean group [120, 121] and is called the Schrödinger group.[2] For the dynamical exponent $z = 2$ there are two additional generators: the scaling generator D and the special conformal generator C. The scale symmetry acts on the time and spatial coordinates according to

$$(x_i, t) \to (x_i', t') = (\lambda x_i, \lambda^2 t), \tag{B.4}$$

where λ is a scale parameter. A special conformal transformation of the temporal and spatial coordinates is given by [121]

$$(x_i, t) \to (x_i', t') = (\frac{x_i}{1 - ct}, \frac{t}{1 - ct}), \tag{B.5}$$

[1] This is the nonrelativistic analogue of the Poincare group in relativistic QFT.

[2] This is the nonrelativistic counterpart of the conformal group.

where c is a parameter of the special conformal transformation. The additional, nontrivial commutators of the Schrödinger algebra are

$$[P_i, D] = -iP_i, \quad [P_i, C] = -iK_i, \quad [K_i, D] = iK_i, \tag{B.6}$$

$$[D, C] = -2iC, \quad [D, H] = 2iH, \quad [C, H] = iD. \tag{B.7}$$

It is important to note that besides the free theory there are few known examples of interacting theories which are symmetric with respect to the Schrödinger group. These theories are called nonrelativistic conformal field theories (NRCFT) and $SU(2)$ nonrelativistic fermions at unitarity, discussed in Chapter 4, are believed to constitute one of them.

In analogy to relativistic conformal field theories it is possible to introduce primary operators in a NRCFT [43]. A local primary operator $\mathscr{O}(t, \vec{x})$ has a well defined scaling dimension $\Delta_{\mathscr{O}}$ and particle number $N_{\mathscr{O}}$

$$[D, \mathscr{O}] = i\Delta_{\mathscr{O}}\mathscr{O}, \qquad [N, \mathscr{O}] = N_{\mathscr{O}}\mathscr{O}, \tag{B.8}$$

where $\mathscr{O} \equiv \mathscr{O}(t = 0, \vec{x} = 0)$. The primary operator $\mathscr{O}$ also commutes with K_i and C

$$[K_i, \mathscr{O}] = 0 \qquad [C, \mathscr{O}] = 0. \tag{B.9}$$

It is possible to show that the operators, constructed by taking spatial and temporal derivatives of a primary operator $\mathscr{O}$, form an irreducible representation of the Schrödinger group. Similar to the relativistic case the form of the two-body Green function of any primary operator is fixed by the conformal symmetry (in the imaginary time formalism) [43]

$$< \mathscr{O}\mathscr{O}^\dagger > \sim (i\hat{\omega} + \frac{\vec{q}^2}{2MN_{\mathscr{O}}})^\nu, \tag{B.10}$$

where $\nu = \Delta_{\mathscr{O}} - 5/2$ for $d = 3$. The simplest examples of primary operators in the theory of SU(2) symmetric fermions are the atom operator ψ ($N_\psi = 1, \Delta_\psi = 3/2$) and the diatom operator φ ($N_\varphi = 2, \Delta_\varphi = 2$). The form of the inverse propagators at unitarity, which we found to be given by Eq. (4.24) in Chapter 4, is consistent with Eq. (B.10).

Appendix C

Bound state approximation and separable potential

In this appendix we present a solution of the two-body sector using the Lippmann-Schwinger equation of quantum mechanics, which helps to elucidate the efficiency of the two-channel model and the limitations of the trion approximation used in [85].

The one-channel model provides an alternative description of ultracold atoms near a broad Feshbach resonance. This model contains the atom field ψ only and the microscopic action is given by[1]

$$S = \int\limits_{Q} \psi^*(Q)(i\omega + q^2)\psi(Q) + \frac{\lambda_\psi}{2} \int\limits_{Q_1,\ldots,Q_4} \psi^*(Q_1)\psi(Q_2)\psi^*(Q_3)\psi(Q_4), \quad \text{(C.1)}$$

where λ_ψ is a pointlike four-atom interaction which is related to the s-wave scattering length in the IR. Roughly speaking, the quantum-mechanical atom-atom interaction potential of the one-channel model (C.1) in Minkowski space is given by[2]

$$V(\vec{x}) = \frac{\lambda_\psi}{2}\delta^{(3)}(\vec{x}). \quad \text{(C.2)}$$

Let us now perform a Fourier transformation of this potential

$$V(\vec{k}, \vec{k}') = \int d^3r \exp[-i(\vec{k}' - \vec{k}) \cdot \vec{r}] V(\vec{r}) = \frac{\lambda_\psi}{2}. \quad \text{(C.3)}$$

[1]For simplicity, we present the one-channel model for $U(1)$ bosons at *unitarity* only. However, our arguments can be extended away from unitarity and are applicable to both $SU(2)$ and $SU(3)$ fermion systems.

[2]Strictly speaking, the contact interaction is ill-defined and must be regularized. This can be done by introducing the pseudo-potential $V(\vec{r})\psi(\vec{r}) = \lambda_\psi \delta^{(3)}(\vec{r}) \frac{\partial}{\partial r}(r\psi(\vec{r}))$. Here we use an alternative regularization by introducing a momentum cutoff Λ directly into the Lippmann-Schwinger equation.

At this point two important remarks about the potential (C.3) can be made

- $V(\vec{k},\vec{k}')$ is a separable potential because it can be written in the following form $\frac{\lambda_\psi}{2}U(\vec{k})U(\vec{k}')$.
- $V(\vec{k},\vec{k}')$ is $\vec{k}$ and $\vec{k}'$ independent, i.e. $U(\vec{k}) = U(\vec{k}') = 1$.

We investigate the atom-atom scattering in the center-of-mass frame. The Lippmann-Schwinger integral equation for the K-matrix is [127, 98]

$$K(\vec{k},\vec{k}',E) = V(\vec{k},\vec{k}') + \mathscr{P}\int^{\Lambda}\frac{d^3q}{(2\pi)^3}\frac{V(\vec{k},\vec{q})K(\vec{q},\vec{k}',E)}{E-2\vec{q}^2}, \tag{C.4}$$

where $\mathscr{P}$ denotes the Cauchy principle value and Λ is a momentum cutoff, which regularizes the contact interaction. The K-matrix is similar to the T-matrix but uses a standing wave boundary condition which leads to the principal value prescription in Eq. (C.4). The kinematics of $K(\vec{k},\vec{k}',E)$ is similar to the kinematics depicted in Figure 4.3. The integral equation (C.4) can be easily solved in the special case of a *separable potential*. The solution factorizes

$$K(\vec{k},\vec{k}',E) = -\frac{U(\vec{k})U(\vec{k}')}{D(E)}, \tag{C.5}$$

where $D(E)$ is given by

$$D(E) = -\frac{2}{\lambda_\psi} + \mathscr{P}\int^{\Lambda}\frac{d^3q}{(2\pi)^3}\frac{U^2(\vec{q})}{E-2\vec{q}^2}. \tag{C.6}$$

In the special case of the contact interaction Eq. (C.5) depends only on E. This means that the exact atom-atom scattering amplitude in the center-of-mass frame can be rewritten in terms of the exchange of the composite diatom with inverse propagator $P_\phi(E,\vec{p}=0) \sim D(E)$. For the contact interaction $D(E)$ is given by

$$D(E) = -\frac{2}{\lambda_\psi} + \mathscr{P}\int^{\lambda}\frac{dq}{2\pi^2}\frac{q^2}{E-2q^2} = -\frac{2}{\lambda_\psi} - \frac{\Lambda}{4\pi^2} + \frac{E}{8\pi^2}\mathscr{P}\int^{\Lambda}\frac{dq}{q^2-E/2}. \tag{C.7}$$

The microscopic λ_ψ can be adjusted such that

$$\frac{2}{\lambda_\psi} + \frac{\Lambda}{4\pi^2} \sim a^{-1}. \tag{C.8}$$

At unitarity the first two terms in the second Eq. (C.7) cancel. The last integral is convergent, hence we take $\Lambda \to \infty$. By dimensional analysis we obtain

$$D(E) \sim \sqrt{E}. \tag{C.9}$$

To summarize, the atom-atom scattering amplitude is momentum-independent in the center-of-mass frame. Hence the two-body sector can be solved exactly by introducing a diatom exchange in the s-channel. By Galilean symmetry this result can be extended to a general inertial reference frame

$$D(E, \vec{k}) \sim \sqrt{E - \frac{\vec{k}^2}{4M_\psi}} \tag{C.10}$$

The functional form of the inverse diatom propagator is consistent with our findings (4.24) in Sect. 4.3.

In the three-body channel the atom-diatom interacting potential is momentum dependent in the center-of-mass frame. The momentum dependence is generated by the box diagram (see first diagram on RHS of Figure 4.4). For this reason the trion approximation, which we used in [85], and in particular the pointlike approximation (Sect. 4.5), do not fully capture this momentum dependence and is not as efficient as the "diatom trick". It leads to the quantitative inaccuracy of the Efimov parameter s_0.

Appendix D

Effective range expansion

In quantum mechanics the scattering of pointlike particles in the center of mass frame is described by the scattering amplitude $f_p(\theta, \phi)$ with p denoting the magnitude of the momentum of the colliding particles and θ and ϕ the spherical angles of direction of scattering. If the particles interact through a central potential, the scattering amplitude depends only on the angle θ and can be expanded into the partial waves according to

$$f_p(\theta) = \sum_{l=0}^{\infty} (2l+1) f_l(p) P_l(\cos\theta), \tag{D.1}$$

where $P_l(\cos\theta)$ denotes the Legendre polynomials. For small collision energies $E = \frac{p^2}{m}$ the dominant contribution in the sum (D.1) is given by the s-wave $f_0(p)$,[1] which can be expressed as [28]

$$f_0(p) = \frac{1}{p\cot\delta_0(p) - ip}, \tag{D.2}$$

with δ_0 denoting the s-wave phase shift. At low energies the function $p\cot\delta_0(p)$ can be expanded in even powers of p which yields the effective range expansion

$$p\cot\delta_0(p) = -a^{-1} + \frac{1}{2} r_{\text{eff}} p^2 + O(p^4). \tag{D.3}$$

This defines the s-wave scattering length a and the effective range r_{eff}.

In this appendix we aim to recover the formula for the quantum mechanical partial s-wave $f_0(p)$ and to find an expression for the effective range r_{eff} in terms of the QFT description of the two-body scattering. Specifically, we

[1] This does not apply to the scattering of two identical fermions, where even partial waves are prohibited by statistics.

consider the two-body sector of the theory of elementary bosons ψ interacting with molecular composite bosons ϕ via a Yukawa-type interaction. The two-body scattering of the elementary bosons is mediated by the exchange of the composite molecule ϕ and the field theoretical amplitude $\mathcal{A}$ is given by

$$\mathcal{A}(\omega, \vec{q}) = \frac{h^2}{P_\phi(\omega, \vec{q})}, \tag{D.4}$$

where $P_\phi(\omega, \vec{q})$ denotes the inverse molecular propagator, while ω and $\vec{q}$ are the energy and momentum of the exchanged particle. The inverse propagator can be calculated exactly in the non-relativistic vacuum and was determined in Chapter 4 using the functional renormalization group method. It was found to be

$$P_\phi(\omega, \vec{q}) = P_\phi^{UV}(\omega, \vec{q}) - \frac{h^2}{16\pi}\left(\Lambda - \sqrt{\frac{1}{2}\left[-\omega + \frac{\vec{q}^2}{2} - i\epsilon\right]}\right), \tag{D.5}$$

where Λ is the UV cutoff, which can be identified with the inverse of the range of interactions. In Chapter 4 the imaginary time formalism was employed. In this appendix we work in the real time formalism by performing an inverse Wick rotation $\omega = -i\omega_E - i\epsilon$. Moreover, the gap parameter E_ψ can be absorbed into the energy ω and for this reason we choose $E_\psi = 0$ in this Appendix. Our convention is $\hbar = 2M = 1$. Obviously, the inverse propagator must be renormalized and we choose

$$P_\phi^{UV}(\omega, \vec{q}) = \frac{h^2}{16\pi}\Lambda - \frac{h^2}{16\pi}a^{-1} + A_\phi^\Lambda\left(-\omega + \frac{\vec{q}^2}{2} - i\epsilon\right). \tag{D.6}$$

In addition to the divergent counterterm, two finite terms were introduced. These terms are necessary in order to recover the leading terms of the effective range expansion. The field theoretical amplitude $\mathcal{A}$ in the center of mass frame is related to the quantum mechanical s-wave amplitude $f_0(p)$ by

$$f_0(p) = (16\pi)^{-1}\mathcal{A}(\omega = 2p^2, \vec{q} = 0). \tag{D.7}$$

Substituting Eqs. (D.4, D.5, D.6) into Eq. (D.7) we obtain

$$f_0(p) = \frac{1}{-a^{-1} - \frac{32\pi A_\phi^\Lambda}{h^2}p^2 - ip}. \tag{D.8}$$

We observe that the finite part of the UV value of the inverse propagator (D.6) gives rise to the scattering length a and the effective range

$$r_{\text{eff}} = -\frac{64\pi A_\phi^\Lambda}{h^2} \tag{D.9}$$

in the scattering amplitude $f_0(p)$.

It is instructive to compute the scattering amplitude $f_0(p)$ choosing the linear ansatz of the dimer propagator

$$P_\phi(\omega, \vec{q}) = A_\phi \left(-\omega + \frac{\vec{q}^2}{2} - i\epsilon \right) + m_\phi^2, \tag{D.10}$$

which we used in this work and which is also employed frequently in two-channel calculations concerning the BEC-BCS crossover [13]. If we choose the cutoff (5.2) the flow equations (5.3) for A_ϕ and m_ϕ^2 for $E_\psi = 0$ read

$$\partial_t m_\phi^2 = \frac{h^2}{12\pi^2} k, \qquad \partial_t A_\phi = -\frac{h^2}{12\pi^2 k}, \tag{D.11}$$

and can be solved analytically. For $\Lambda \to \infty$ the solution as a function of the sliding scale k is given by

$$m_\phi^2 = -\frac{h^2}{16\pi} a^{-1} + \frac{h^2}{12\pi^2} k, \qquad A_\phi = A_\phi^\Lambda + \frac{h^2}{12\pi^2 k}. \tag{D.12}$$

We observe that the wave function renormalization A_ϕ diverges as $k \to 0$. The origin of this divergence can be understood by examining the exact solution (D.5). Obviously, the square root part of Eq. (D.5) can not be expanded in the Taylor series around the point $W = w - \frac{\vec{q}^2}{2} = 0$. This indicates that the linear ansatz (D.10) is not the best choice in vacuum and a different approximation should better be used. Nevertheless, we demonstrate that it is still possible to recover approximately $f_0(p)$ using the linear ansatz. To this end we expand the inverse propagator $P_\phi(\omega, \vec{q})$ not around $W = 0$, but around some finite value $W_p = 2(cp)^2$, where c is some unspecified real positive number

$$P_\phi(\omega, \vec{q}) = A_\phi^{(p)} \left(-\omega + \frac{\vec{q}^2}{2} + W_p - i\epsilon \right) + m_\phi^{2(p)}. \tag{D.13}$$

In our formulation this expansion corresponds to $E_\psi = -(cp)^2 - i\epsilon$. In this case the IR limit $k \to 0$ is regular and we obtain

$$m_\phi^{2(p)} = -\frac{h^2}{16\pi} a^{-1} - \frac{ih^2 c}{16\pi} p \qquad A_\phi^{(p)} = A_\phi^\Lambda + \frac{ih^2}{64\pi c} \frac{1}{p}. \tag{D.14}$$

From Eq. (D.7) follows the s-wave scattering amplitude $f_0(p)$ as

$$\begin{aligned} f_0(p) &= \frac{h^2}{16\pi P_\phi(\omega = 2p^2, \vec{q} = 0)} \\ &= \frac{1}{-a^{-1} - \frac{32\pi A_\phi^\Lambda}{h^2} p^2 - ig(c)p}. \end{aligned} \tag{D.15}$$

Notably, the effective range r_{eff} is independent on the number c and agrees with the exact result obtained above. On the other hand, the coefficient of the imaginary part of the effective range expansion depends on the value of the arbitrarily chosen number c as $g(c) = \frac{1+2c^2}{2c}$. The correct value $g(c) = 1$ can not be reproduced for any real choice of c. The function $g(c)$ attains its minimum value $g_{\text{min}} = \sqrt{2}$ at $c = 1/\sqrt{2}$.

Finally, we checked that the same results are obtained for different types of regulators such as the sharp or the momentum-independent k^2 cutoff. In the case of the scattering of distinguishable particles the analysis is very similar to the one presented above with the only difference that $r_{\text{eff}} = -\frac{32\pi A_\phi^\Lambda}{h^2}$.

Appendix E

Scaling dimension of composite operator $\mathcal{O} = \psi\psi$

An elegant way how to calculate the scaling dimensions of the composite two-particle operator $\mathcal{O} = \psi\psi$ (and more generally of the two-particle primary operators $\mathcal{O}^{(l)}$ carrying the angular momentum l) is to employ the operator/state correspondence [128, 129, 43]. To this end one considers two particles interacting through the inverse square potential confined in a harmonic trap. The total Hamiltonian H of this system can be separated into the center-of-mass and relative parts

$$\begin{aligned} &H = H_R + H_r, \\ &H_R = -\frac{1}{4}\nabla^2_{\vec{R}} + \omega^2 R^2, \qquad E^0_R = \omega\frac{D}{2}, \\ &H_r = -\nabla^2_{\vec{r}} - \frac{\kappa}{r^2} + \frac{\omega^2 r^2}{4}, \qquad E^{\pm}_{r,l} = \omega\left(1 \pm \sqrt{\left(l + \frac{(D-2)}{2}\right)^2 - \kappa}\right), \end{aligned} \tag{E.1}$$

where $\vec{R}$ and $\vec{r}$ are the center-of-mass and relative coordinates. In addition, E^0_R denotes the ground state energy of H_R, and $E^{\pm}_{r,l}$ stands for the lowest energy of the Hamiltonian H_r in the subspace of states with the angular momentum l.[1] According to the operator/state correspondence, the scaling

[1]The relative Hamiltonian H_r defines a quantum mechanical problem of a particle in the combined inverse square and harmonic potential, also known as the Calogero problem. The energy spectrum is formally given by two equidistant towers built on top of two "lowest state energies" $E^+_{r,l}$ and $E^-_{r,l}$ [130]. Physically, there are two proper choices of the near-origin boundary condition of the wave function that distinguish between + and − branches of the energy spectrum. The choice $E^+_{r,l}$ ($E^-_{r,l}$) corresponds to CFT_+ (CFT_-) of Sec. 6.1.

dimension of the composite primary $\mathcal{O}^{(l)}$, carrying the angular momentum l, coincides with the lowest energy E_l^0 of the total Hamiltonian H, expressed in the units of the trapping frequency ω

$$\Delta_{\pm}^{(l)} = \frac{E_l^0}{\omega} = \frac{D+2}{2} \pm \sqrt{\left(l + \frac{D-2}{2}\right)^2 - \kappa}. \tag{E.2}$$

Note that the operator $\mathcal{O}^{(l)}$ composed of two identical bose (fermi) fields vanishes if the angular momentum l is odd (even). This is due to the fact that two identical bosons (fermions) can not be in the quantum state with odd (even) angular momentum. For the s-wave ($l = 0$) operator $\mathcal{O}^{(l=0)} = \psi\psi$ we thus obtain

$$\Delta_{\pm} \equiv \Delta_{\pm}^{(l=0)} = \frac{D+2}{2} \pm \sqrt{\left(\frac{D-2}{2}\right)^2 - \kappa}. \tag{E.3}$$

We must stress that the operator/state correspondence applies only to nonrelativistic conformal field theories, and thus our result (E.2) holds for $\kappa < \kappa_{cr} = \left(l + \frac{D-2}{2}\right)^2$, when both $\Delta_{\pm}^{(l)}$ are real. Nevertheless, it turns out that even in the anomalous (nonconformal) regime for $\kappa > \kappa_{cr}$ Eq. (E.2) leads to the correct scaling dimensions $\Delta_{\pm}^{(l)}$. We illustrate this fact on the example of the s-wave composite operator $\mathcal{O}(t, \vec{x})$. Following the observation, made in [43], the a proper definition of the composite $\mathcal{O}(t, \vec{x})$ for any value of κ is given by

$$\mathcal{O}(t, \vec{x}) = \lim_{\vec{y} \to \vec{x}} |\vec{x} - \vec{y}|^{-\gamma} \psi(t, \vec{x}) \psi(t, \vec{y}), \tag{E.4}$$

where γ is a leading near-origin power law exponent of the zero-energy wave function of the relative Hamiltonian H_r. It can be determined from the equation $H_r r^{\gamma} = 0$ and reads

$$\gamma = 1 - \frac{D}{2} \pm \sqrt{\left(\frac{D-2}{2}\right)^2 - \kappa} \tag{E.5}$$

The prefactor $|\vec{x} - \vec{y}|^{\gamma}$ in Eq. (E.4) is needed to make matrix elements of the operator $\mathcal{O}(t, \vec{x})$ between any two states in the Hilbert space finite. From Eq. (E.4) we can read off the scaling dimension of the operator $\mathcal{O}$ by a simple counting

$$\Delta_{\pm} = 2\Delta_{\psi} + \gamma = \frac{D+2}{2} \pm \sqrt{\left(\frac{D-2}{2}\right)^2 - \kappa} \tag{E.6}$$

which is in agreement with Eq. (E.3), found from the operator/state correspondence.

Bibliography

[1] E. Braaten, H.W. Hammer, Phys. Rept. **428**, 259 (2006).

[2] C. Chin, R. Grimm, P. Julienne, and E. Tiesinga, Rev. Mod. Phys. **82**, 1225 (2010).

[3] V. Efimov, Phys. Lett. **33B**, 563 (1970); Nucl. Phys. A **210**, 157 (1973).

[4] T. Kraemer et al., Nature **440**, 315 (2006).

[5] F. Ferlaino, R. Grimm, Physics **3**, 9 (2010).

[6] E. Nielsen, D. V. Fedorov, A. S. Jensen and E. Garrido, Phys. Rep. **347**, 373 (2001).

[7] Rajat K. Bhaduri, Arindam Chatterjee, Brandon P. van Zyl, arXiv:1009.2713 [quant-ph].

[8] K. G. Wilson, Phys. Rev. B **4**, 3174 (1971).

[9] J. Berges, N. Tetradis, and C. Wetterich, Phys. Rept. **363**, 223 (2002).

[10] H. Gies, arXiv:hep-ph/0611146.

[11] M. Salmhofer and C. Honerkamp, Prog. Theor. Phys. **105** (2001) 1.

[12] B. Delamotte, D. Mouhanna and M. Tissier, Phys. Rev. B **69**, 134413 (2004).

[13] S. Diehl, S. Floerchinger, H. Gies, J. M. Pawlowski and C. Wetterich, Annalen Phys. **522**, 615 (2010).

[14] P. Kopietz, L. Bartosch, F. Schutz, Lect. Notes Phys. **798** (2010).

[15] M. Reuter, Phys. Rev. D **57**, 971 (1998).

[16] M. Reuter and F. Saueressig, arXiv:0708.1317 [hep-th].

[17] C. Wetterich, Phys. Lett. B **301** (1993) 90.

[18] J. M. Pawlowski, Ann. Phys. **322**, 2831 (2007).

[19] D. F. Litim, Phys. Lett. B **486**, 92 (2000).

[20] D. F. Litim, Phys. Rev. D **64**, 105007 (2001).

[21] B. Delamotte, arXiv:cond-mat/0702365.

[22] J. Polchinski, Nucl. Phys. B **231** (1984) 269.

[23] H. Gies, C. Wetterich, Phys. Rev. D **65**, 065001 (2002); Acta Phys. Slov. **52**, 215 (2002).

[24] S. Floerchinger, C. Wetterich, Phys. Lett. B **680**, 371 (2009).

[25] C. M. Bender, F. Cooper, G. S. Guralnik and D. H. Sharp, Phys. Rev. D **19**, 1865 (1979).

[26] J. Iliopoulos, C. Itzykson and A. Martin, Rev. Mod. Phys. **47**, 165 (1975).

[27] H. Feshbach and P. M. Morse, "Methods of Theoretical Physics II", McGrow-Hill book company, 1953.

[28] L. D. Landau, E. M. Lifshitz, "Quantum Mechanics: Non-relativistic Theory", Pergamon Press, 1977.

[29] K. M. Case, Phys. Rev. **80**, 797 (1950).

[30] V. de Alfaro, S. Fubini and G. Furlan, Nuovo Cim. A **34**, 569 (1976).

[31] E. Kolomeisky and J. P. Straley, Phys. Rev. B **46**, 12664 (1992).

[32] K. S. Gupta and S. G. Rajeev, Phys. Rev. D **48**, 5940 (1993).

[33] S. R. Beane, P. F. Bedaque, L. Childress, A. Kryjevski, J. McGuire and U. v. Kolck, Phys. Rev. A **64**, 042103 (2001).

[34] T. Barford and M. C. Birse, Phys. Rev. C **67**, 064006 (2003).

[35] M. Bawin and S. A. Coon, Phys. Rev. A **67**, 042712 (2003).

[36] E. J. Mueller and T. L. Ho, [arXiv:cond-mat/0403283].

[37] E. Braaten and D. Phillips, Phys. Rev. A **70**, 052111 (2004).

[38] T. Barford and M. C. Birse, J. Phys. A **38**, 697 (2005).

[39] H. W. Hammer and B. G. Swingle, Annals Phys. **321**, 306 (2006).

[40] H. W. Hammer and R. Higa, Eur. Phys. J. A **37**, 193 (2008).

[41] D. B. Kaplan, J. W. Lee, D. T. Son and M. A. Stephanov, Phys. Rev. D **80**, 125005 (2009).

[42] W. Frank, D. J. Land and R. M. Spector, Rev. Mod. Phys. **43**, 36 (1971).

[43] Y. Nishida and D. T. Son, Phys. Rev. D **76**, 086004 (2007).

[44] H. E. Camblong and C. R. Ordonez, Phys. Rev. D **68**, 125013 (2003).

[45] J. Macek, J. Phys. B **1**, 831 (1968).

[46] L. D. Faddeev, Sov. Phys. JETP **12**, 1014 (1961).

[47] H. E. Camblong, L. N. Epele, H. Fanchiotti and C. A. Garcia Canal, Phys. Rev. Lett. **87**, 220402 (2001).

[48] J. M. Kosterlitz, and D. J. Thouless, J. Phys. C, Solid State Phys., **6**, 1181-1203 (1973).

[49] P. Claus, M. Derix, R. Kallosh, J. Kumar, P. K. Townsend and A. Van Proeyen, Phys. Rev. Lett. **81**, 4553 (1998)

[50] J. M. Maldacena, Adv. Theor. Math. Phys. **2** (1998) 231 [Int. J. Theor. Phys. **38** (1999) 1113]. S. S. Gubser, I. R. Klebanov and A. M. Polyakov, Phys. Lett. B **428** (1998) 105. E. Witten, Adv. Theor. Math. Phys. **2** (1998) 253.

[51] S. Moroz, Phys. Rev. D **81**, 066002 (2010).

[52] S. Moroz, S. Floerchinger, R. Schmidt and C. Wetterich, Phys. Rev. A **79**, 042705 (2009).

[53] M. S. Hussein, arXiv.org:physics/0003081.

[54] E. Braaten, D. Kang and L. Platter, Phys. Rev. A **78**, 053606 (2008).

[55] N. Syassen et. al., Science **320**, 1329 (2008).

[56] M. Kiffner, M. J. Hartmann, arXiv:0908.2055 [quant-ph].

[57] M. P. A. Fisher, and W. Zwerger, Phys. Rev. B **32**, 6190 (1985).

[58] F. Guinea, V. Hakim, and A. Muramatsu, Phys. Rev. Lett. **54**, 263 (1985).

[59] H. Gies, and J. Jaeckel, Eur. Phys. J. C **46**, 433-438 (2006).

[60] J. Braun, and H. Gies, JHEP 0606 (2006) 024; Phys. Lett. B **645** 53-58 (2007),JHEP **1005**, 060 (2010).

[61] S. S. Lee, Phys. Rev. D **79**, 086006 (2009).

[62] H. Liu, J. McGreevy and D. Vegh, arXiv:0903.2477 [hep-th].

[63] T. Faulkner, H. Liu, J. McGreevy and D. Vegh, arXiv:0907.2694 [hep-th].

[64] S. Giorgini, L. P. Pitaevskii and P Stringari, Rev. Mod. Phys. **80**, 1215 (2008).

[65] I. Bloch, J. Dalibard and W. Zwerger, Rev. Mod. Phys **80**, 885 (2008).

[66] S. Knoop *et al.*, Nature Phys. **5**, 277 (2009).

[67] M. Zaccanti *et al.*, Nature Phys. **5**, 586 (2009).

[68] G. Barontini *et al.* Phys. Rev. Lett. **103**, 043201(2009).

[69] S. Pollack, *et al.*, Science **326**, 1683 (2009).

[70] P. F. Bedaque, H. W. Hammer and U. van Kolck, Phys. Rev. Lett. **82**, 463 (1999).

[71] P. F. Bedaque, H. W. Hammer and U. van Kolck, Nucl. Phys. A **646**, 444 (1999).

[72] I.V. Brodsky, A.V. Klaptsov, M.Yu. Kagan, R. Combescot, X. Leyronas, JETP Letters **82**, 273 (2005).

[73] J. Levinsen and V. Gurarie, Phys. Rev. A **73**, 053607 (2006).

[74] D. S. Petrov, Phys. Rev. A **67**, 010703(R) (2003).

[75] G. Rupak, nucl-th/0605074.

[76] Y. Nishida and D. T. Son, Phys. Rev. Lett. **97**, 050403 (2006).

[77] S. Diehl, H. C. Krahl, M. Scherer, Phys. Rev. C **78**, 034001 (2008).

[78] M. C. Birse, Phys. Rev. C **77**, 047001 (2008).

[79] G. V. Skorniakov, K. A. Ter-Martirosian, Zh. Eksp. Teor. Phys. **31**, 775 (1956), [Sov. Phys. JETP **4**, 648 (1957)].

[80] A. Rapp, G. Zarand, C. Honerkamp and W. Hofstetter, Phys. Rev. Lett. **98**, 160405 (2007).

[81] T. Brauner, Phys. Rev. D **75**, 105014 (2007).

[82] L. He, M. Jin and P. Zhuang, Phys. Rev. A **74**, 033604 (2006).

[83] T. Paananen, J. P. Martikainen, and P. Torma, Phys. Rev. A **73**, 053606 (2006); Phys. Rev. A **75**, 023622 (2007).

[84] R. W. Cherng, G. Refael, and E. Demler, Phys. Rev. Lett. **99**, 130406 (2007).

[85] S. Floerchinger, R. Schmidt, S. Moroz and C. Wetterich, Phys. Rev. A **79**, 013603 (2009).

[86] R. Schmidt, Dimploma thesis, Heidelberg 2009.

[87] S. Floerchinger, PhD thesis, Heidelberg 2009, arXiv:0909.0416.

[88] K. M. O'Hara *et al.*, Science **298**, 2179 (2002); C. A. Regal, M. Greiner, and D. S. Jin, Phys. Rev. Lett. **92**, 040403 (2004); M. Bartenstein *et al.*, Phys. Rev. Lett. **92**, 120401 (2004); M. W. Zwierlein *et al.*, Phys. Rev. Lett. **92**, 120403 (2004); J. Kinast, S. L. Hemmer, M. E. Gehm, A. Turlapov, and J. E. Thomas, Phys. Rev. Lett. **92**, 150402 (2004); T. Bourdel *et al.*, Phys. Rev. Lett. **93**, 050401 (2004).

[89] T. B. Ottenstein and T. Lompe and M. Kohnen and A. N. Wenz and S. Jochim, Phys. Rev. Lett. **101**, 203202 (2008).

[90] J. H. Huckans, J. .R. Williams, E. L. Hazlett, R. W. Stites and K. M. O'Hara, Phys. Rev. Lett. **102**, 165302 (2009).

[91] E. Braaten, H.-.W. Hammer, D. Kang and L. Platter, Phys. Rev. Lett. **103**, 073202 (2009).

[92] P. Naidon and M. Ueda, Phys. Rev. Lett. **103**, 073203 (2009).

[93] R. Schmidt, S. Floerchinger, and C. Wetterich Phys. Rev. A **79**, 053633 (2009).

[94] S. Diehl, H. Gies, J. M. Pawlowski and C. Wetterich, Phys. Rev. A **76**, 053627 (2007).

[95] S. Diehl and C. Wetterich, Nucl. Phys. B **770**, 206 (2007); Phys. Rev. A **73** (2006) 033615; S. Diehl, cond-mat/0701157.

[96] S. Diehl, H. Gies, J. M. Pawlowski and C. Wetterich, Phys. Rev. A **76**, 021602(R) (2007).

[97] S. Floerchinger and C. Wetterich Phys. Rev. A **77**, 053603 (2008).

[98] M. C. Birse, J. A. McGovern and K. G. Richardson, Phys. Lett. B **464**, 169 (1999).

[99] P. Nicolic and S. Sachdev Phys. Rev. A **75**, 033608 (2007).

[100] L. Platter, Few Body Syst. **46**, 139 (2009).

[101] O. A. Yakubovsky, Yad. Fiz. **5**, 1312 (1967); [Sov. J. Nucl. Phys. **5**, 937 (1967)].

[102] J. A. Tjon, Phys. Rev. Lett. **56**, 217 (1975).

[103] B. F. Gibson, and D. R. Lehmann, Phys. Rev. C **14**, 685 (1976).

[104] A. C. Fonseca, and P. E. Shanley, Phys. Rev. C **14**, 1343 (1976).

[105] J. A. Tjon, in *Few-body Systems and Nuclear Forces II*, edited by H. Ziegel *et al.* (Springer, Berlin, 1978); D. Blume and C. H. Greene, J. Chem. Phys. **112**, 8053 (2000); K. B. Whaley, Int. Rev. Phys. Chem. **13**, 41 (1994).

[106] D. S. Petrov, C. Salomon, and G. V. Shlyapnikov, Phys. Rev. Lett **93**, 090404 (2004).

[107] L. Platter, H.-W. Hammer, and Ulf-G. Meißner, Phys. Rev. A **70**, 052101 (2004).

[108] H.-W. Hammer, and L. Platter, Eur. Phys. J. A **32**, 113 (2007).

[109] J. von Stecher, J. P. D'Incao, and C. H. Greene, Nature Phys. **5**, 417-421 (2009).

[110] J. P. D'Incao, J. von Stecher, and C. H. Greene, Phys. Rev. Lett. **103**, 033004 (2009).

[111] A. Deltuva, arXiv:1009.1295.

[112] F. Ferlaino, *et al.*, Phys. Rev. Lett. **102**, 140401 (2009).

[113] S.J.J.M.F. Kokkelmans et al., Phys. Rev. A **65**, 053617 (2002).

[114] R. Schmidt, S. Moroz, Phys. Rev. **A81**, 052709 (2010).

[115] M. T. Yamashita, L. Tomio, A. Delfino, and T. Frederico, Europhys. Lett. **75**, 555 (2006).

[116] S. K. Adhikari, T. Frederico, and I. D. Goldmann, Phys. Rev. Lett. **74**, 487 (1995).

[117] R. D. Amado, and F. C. Greenwood, Phys. Rev. D **7**, 2517 (1973).

[118] Y. Nishida and D. T. Son, arXiv:1004.3597.

[119] T. Mehen, I. W. Stewart and M. B. Wise, Phys. Lett. B **474**, 145 (2000).

[120] U. Niederer, Helv. Phys. Acta **45**, 802 (1972).

[121] C. R. Hagen, Phys. Rev. D **5**, 377 (1972).

[122] H. E. Camblong and C. R. Ordonez, Mod. Phys. Lett. A **17**, 817 (2002); Int. J. Mod. Phys. A **19**, 1413 (2004).

[123] L. Rodberg and R. Thaler, "Introduction to the quantum theory of scattering", Academic Press, New York, 1967.

[124] S. Moroz, arXiv:1007.4635.

[125] Y. Nishida and D. T. Son, Phys. Rev. A 82, 043606 (2010).

[126] J. von Stecher, J. Phys. B: At. Mol. Opt. Phys. **43**, 101002 (2010).

[127] R. F. Mohr, R. J. Furnstahl, R. J. Perry, K. G. Wilson and H. W. Hammer, Annals Phys. **321**, 225 (2006).

[128] S. Tan, arXiv:cond-mat/0412764.

[129] F. Werner and Y. Castin, Phys. Rev. Lett. **97**, 150401 (2006); Phys. Rev. A **74**, 053604 (2006).

[130] F. Calogero, J. Math. Phys. **10**, 2191 (1969).

Acknowledgments

I would like to thank my PhD advisor Christof Wetterich. I am obliged to him for permanent support and deep insight in physics which he shared with me during the last three years.

I am very thankful to Stefan Floerchinger and Richard Schmidt for the fruitful joint work and countless hours of discussions.

I am indebted to M. Birse, E. Braaten, S. Diehl, H. Gies, C.H. Greene, H.W. Hammer, J. Hosek, S. Jochim, D. Kaplan, H.C. Krahl, M. Kohen, T. Lompe, Y. Nishida, T.B. Ottenstein, J.M. Pawlowski, M. Scherer, D.T. Son, J. von Stecher, A.N. Wenz and W. Zwerger for stimulating discussions about the Efimov physics.

I am grateful to all the members of the institute for theoretical physics (especially my colleagues from the Dachzimmer) for their support during my PhD studies in Heidelberg.

I am indebted to Klaus Tschira Foundation for financial support.

And last but not least I would like to express my personal thanks to Diana, my parents and my brother without whose love and patience this thesis would never have appeared.